3/1/96

Teri D

NUREG/CR-6096

Apache Leap Tuff INTRAVAL Experiments

Results and Lessons Learned

Prepared by
T. C. Rasmussen, S. C. Rhodes, A. Guzman, S. P. Neuman

Department of Hydrology and Water Resources
University of Arizona

Prepared for
U.S. Nuclear Regulatory Commission

AVAILABILITY NOTICE

Availability of Reference Materials Cited in NRC Publications

Most documents cited in NRC publications will be available from one of the following sources:

1. The NRC Public Document Room, 2120 L Street, NW., Lower Level, Washington, DC 20555-0001

2. The Superintendent of Documents, U.S. Government Printing Office, P. O. Box 37082, Washington, DC 20402-9328

3. The National Technical Information Service, Springfield, VA 22161-0002

Although the listing that follows represents the majority of documents cited in NRC publications, it is not intended to be exhaustive.

Referenced documents available for inspection and copying for a fee from the NRC Public Document Room include NRC correspondence and internal NRC memoranda; NRC bulletins, circulars, information notices, inspection and investigation notices; licensee event reports; vendor reports and correspondence; Commission papers; and applicant and licensee documents and correspondence.

The following documents in the NUREG series are available for purchase from the Government Printing Office: formal NRC staff and contractor reports, NRC-sponsored conference proceedings, international agreement reports, grantee reports, and NRC booklets and brochures. Also available are regulatory guides, NRC regulations in the *Code of Federal Regulations*, and *Nuclear Regulatory Commission Issuances*.

Documents available from the National Technical Information Service include NUREG-series reports and technical reports prepared by other Federal agencies and reports prepared by the Atomic Energy Commission, forerunner agency to the Nuclear Regulatory Commission.

Documents available from public and special technical libraries include all open literature items, such as books, journal articles, and transactions. *Federal Register* notices, Federal and State legislation, and congressional reports can usually be obtained from these libraries.

Documents such as theses, dissertations, foreign reports and translations, and non-NRC conference proceedings are available for purchase from the organization sponsoring the publication cited.

Single copies of NRC draft reports are available free, to the extent of supply, upon written request to the Office of Administration, Distribution and Mail Services Section, U.S. Nuclear Regulatory Commission, Washington, DC 20555-0001.

Copies of industry codes and standards used in a substantive manner in the NRC regulatory process are maintained at the NRC Library, Two White Flint North, 11545 Rockville Pike, Rockville, MD 20852-2738, for use by the public. Codes and standards are usually copyrighted and may be purchased from the originating organization or, if they are American National Standards, from the American National Standards Institute, 1430 Broadway, New York, NY 10018-3308.

DISCLAIMER NOTICE

NUREG/CR-6096

Apache Leap Tuff INTRAVAL Experiments

Results and Lessons Learned

Manuscript Completed: September 1995
Date Published: March 1996

Prepared by
T. C. Rasmussen*, S. C. Rhodes, A. Guzman, S. P. Neuman

Department of Hydrology and Water Resources
University of Arizona
Tucson, AZ 85721

T. Nicholson, NRC Project Manager

Prepared for
Division of Regulatory Applications
Office of Nuclear Regulatory Research
U.S. Nuclear Regulatory Commission
Washington, DC 20555-0001
NRC Job Code L1282

*University of Georgia
Athens, GA 30602

OTHER REPORTS IN THIS SERIES

Evans, D.D., 1983, Unsaturated Flow and Transport Through Fractured Rock - Related to High-Level Waste Repositories, NUREG/CR-3206, 231 pp.

Schrauf, T.W. and D.D. Evans, 1984, Relationship Between the Gas Conductivity and Geometry of a Natural Fracture, NUREG/CR-3680, 131 pp.

Huang, C. and D.D. Evans, 1985, A 3-Dimensional Computer Model to Simulate Fluid Flow and Contaminant Transport Through a Rock Fracture System, NUREG/CR-4042, 109 pp.

Green, R.T. and D.D. Evans, 1987, Radionuclide Transport as Vapor Through Unsaturated Fractured Rock, NUREG-CR-4654, 163 pp.

Rasmussen, T.C. and D.D. Evans, 1987, Unsaturated Flow and Transport Through Fractured Rock - Related to High-Level Waste Repositories, NUREG/CR-4655, 474 pp.

Yeh, T.C.J., T.C. Rasmussen and D.D. Evans, 1988, Simulation of Liquid and Vapor Movement in Unsaturated Fractured Rock at the Apache Leap Tuff Site: Models and Strategies, NUREG/CR-5097, 73 pp.

Weber, D.S. and D.D. Evans, 1988, Stable Isotopes of Authigenic Minerals in Variably-Saturated Fractured Tuff, NUREG/CR-5255, 70 pp.

Rasmussen, T.C. and D.D. Evans, 1989, Fluid Flow and Solute Transport Modeling Through Three-Dimensional Networks of Variably Saturated Discrete Fractures, NUREG/CR-5239, 193 pp.

Chuang, Y., W.R. Haldeman, T.C. Rasmussen, and D.D. Evans, 1990, Laboratory Analysis of Fluid Flow and Solute Transport Through a Variably Saturated Fracture Embedded in Porous Tuff, NUREG/CR-5482, 328 pp.

Rasmussen, T.C., D.D. Evans, P.J. Sheets and J.H. Blanford, 1990, Unsaturated Fractured Rock Characterization Methods and Data Sets at the Apache Leap Tuff Site, NUREG/CR-5596, 139 pp.

Evans, D.D. and T.C. Rasmussen, 1991, Unsaturated Flow and Transport Through Fractured Rock Related to High-Level Waste Repositories, Final Report - Phase III, NUREG/CR-5581, 75 pp.

Rasmussen, T.C. and D.D. Evans, 1992, Nonisothermal Hydrologic Transport Experimental Plan, NUREG/CR-5880, 41 pp.

Bassett, R.L., S.P. Neuman, T.C. Rasmussen, A. Guzman, G.R. Davidson, and C.F. Lohrstorfer, 1994, Validation Studies for Assessing Unsaturated Flow and Transport Through Fractured Rock, NUREG/CR-6203.

ABSTRACT

Data from laboratory and field experiments in unsaturated fractured rock are summarized and interpreted for the purpose of evaluating conceptual and numerical models of fluid, heat and solute transport. The experiments were conducted at four scales, in small cores (2.5-cm long by 6-cm across), a large core (12-cm long by 10-cm across), a small block containing a single fracture (20 x 21 x 93 cm), and at field scales in boreholes (30-m long by 10-cm across) at three scales (½-, 1- and 3-meters). The smallest scale in the laboratory provided isothermal hydraulic and thermal properties of unfractured rock. Nonisothermal heat, fluid and solute transport experiments were conducted using the large core. Isothermal gas and liquid flow experiments were conducted in the fractured block. Field-scale experiments using air were used to obtain *in situ* permeability estimates as a function of the measurement scale. Interpretation of experimental results provides guidance for resolving uncertainties related to radionuclide migration from high level waste repositories in unsaturated fractured rock.

TABLE OF CONTENTS

LIST OF TABLES

LIST OF FIGURES

LIST OF FIGURES (continued)

EXECUTIVE SUMMARY

Prediction models of radionuclide migration through unsaturated fractured rock over geologic time scales require the formulation of conceptual models that incorporate the relevant processes of fluid, heat and solute transport. In addition, mathematical and computer models must be formulated that are used to solve the complex processes anticipated near the repository. Also necessary is the proper parameterization of the mathematical models using coefficients that are reliably obtained for the site of interest. This document provides characterization and evaluation data sets for use in evaluating the suitability of current conceptual, mathematical and physical models of fluid, heat and solute transport. Four types of experiments were conducted to provide these data.

The first set of experiments employed small cores of Apache Leap Tuff (white unit), measuring 6 cm in diameter and approximately 2.5 cm in height. Laboratory analyses provide characterization data related to porosity, characteristic curves, hydraulic conductivity, air permeability and thermal conductivity. The effects of variable water contents, hysteresis and temperature on the physical parameters used to predict transport are shown. Data indicate that variations in temperature affect the shape and position of the characteristic curve, and, by inference, the shape and position of the relative permeability curves. The effect of wetting history is also shown to have a great influence on the characteristic curve. Thermal conductivity is shown to be only poorly related in a linear fashion to water content. The effects of solute concentrations on ambient matric potential are also demonstrated. It can be concluded that accumulations of saturated salt solutions will control the ambient matric potential observed under nonisothermal conditions.

A second set of experiments were conducted on a larger core of Apache Leap Tuff (white unit) measuring 9.6 cm in diameter and 12 cm in length. The core was subjected to a series of experiments in which a one-dimensional thermal gradient (5 to 45°C) was applied along the long-axis of the core. The core was hermetically sealed and insulated to provide a closed system for air and water. Dual-gamma attenuation methods were employed to provide water content and solute concentration profiles along the length of the core. An active heat pipe was observed when the core was brought to an intermediate water content. The resulting latent heat transport was insignificant in comparison to the conductive heat transport in this experiment. When a soluble salt (NaI) was introduced into the experiment, the heat pipe phenomenon was not as active due to the increased osmotic potential near the warm end of the core. The increased osmotic potential lowered the vapor pressure near the warm end and reduced the vapor phase transport of water.

A third set of experiments were conducted using a block of Apache Leap Tuff (white unit) containing a discrete fracture. The block measured (20.2 x 21 x 92.5 cm), with the fracture present along the long axis. Characterization experiments were performed to characterize the physical properties of the block. Equivalent fracture apertures were obtained using six types of experiments. Three volumetric fracture aperture values were obtained by using a pycnometer, tracer breakthrough volumes, and the ratio of fracture transmissivity to fracture hydraulic conductivity. Two Poiseuille apertures were obtained using a cubic aperture equation applied to gas and water flow rates, and using a quadratic aperture equation gas breakthrough velocities. A final estimate of fracture aperture was obtained using the air-entry potential of the saturated fracture. The volumetric apertures estimated using the pycnometer and the tracer breakthrough volumes were closely related. The volumetric aperture determined using the ratio of fracture transmissivity to hydraulic conductivity was less, followed by the apertures determined using the cubic and quadratic equations, respectively. The smallest aperture observed was the capillary aperture. This progression is consistent with the

hypothesis that fracture roughness will decrease the effective flow area for the Poiseuille flow, and induce an ink bottle effect at fracture constrictions.

A horizontal fracture imbibition experiment was also conducted using water as a fluid imbibed into an initially dry fractured rock. The imbibition rate was reproduced using a model developed by Nitao and Buscheck [1991]. The form of the model was found to provide a good fit to the shape of the observed data, but the model overestimated the fracture imbibition volume by a factor of twenty and the fracture wetting front advance by a factor of eight. The noted reduction in water inflow may be due to phenomena neglected in the theoretical model, such as fracture surface coatings or enhanced surface weathering, and the inability to accurately determine fracture physical properties *a priori*, such as the fracture water diffusivity. It was shown that fracture saturation behind the wetting front initially is very low, perhaps ten percent, but increases to complete saturation during the course of the experiment. This may indicate fingers of saturation exist within the fracture during early time which expand laterally and dissipate over time.

The fourth data set consists of in-situ air-permeability measurements at different scales and at multiple-injection rates in six (6) boreholes. Field data indicate that the air permeability determinations are strongly affected by two-phase interaction between air and pore water, and in higher permeability zones by inertial flow effects. A 45-degree, 30-meter deep borehole was tested for permeability at three different scales to study the effect of measurement support on permeability estimates and their statistics. These measurements seem to indicate some dependency of the mean permeability on measurement support (length of test interval), a phenomenon known as "scale effect." Upscaling by weighted arithmetic averaging of the smaller measurement support data produces better estimates than geometric weighted averaging. High permeability values are, however, slightly underpredicted by either upscaling approach. Although the observed variability of air permeabilities at the Apache Leap Tuff Site (ALTS) is over 3.5 orders of magnitude, the data are amenable to classical geostatistical analysis and yields well-defined semivariograms. The omni-directional semivariogram exhibits a nested structure with two distinct plateaus and correlation scales and an additional correlation structure whose sill and range are undefined due to the limited extent of the experimental site. Our observation that the variance and correlation scale increase with scale is consistent with the multi-scale continua concept discussed by Burrough [1983] and Neuman [1987, 1990, 1993, 1994]. The available fractured rock permeability data can be viewed as a sample from a random (stochastic) field defined over a continuum with multiple scales of heterogeneity.

FOREWORD

This technical report was prepared by the University of Arizona under their research projects with the Waste Management Branch in the Office of Nuclear Regulatory Research (FINs L1282 and L1283). The report outlines research results and lessons learned from field and laboratory experiments involving unsaturated flow and transport in heterogeneous, fractured rock. This work was performed within the INTRAVAL[1] Project. The work reported focused on evaluation and testing of unsaturated flow and transport conceptual models using water flow, nonisothermal and transport experimental data from the Apache Leap Tuff Site and studies. The lessons learned provide insights into identifying, and in some instances resolving, key technical uncertainties related to site characterization methods and data analysis as input to modeling unsaturated flow and transport over a range of scales (e.g., from centimeter through tens of meters). This document also serves as an INTRAVAL Project report. NUREG/CR-6096 is not a substitute for NRC regulations, and compliance is not required. The approaches and/or methods described in this NUREG/CR are provided for information only. Publication of this report does not necessarily constitute NRC approval with the information contained herein.

---

[1] INTRAVAL is an international cooperative project for studying validation of geosphere transport models. Dr. Todd C. Rasmussen and his colleagues at the University of Arizona served as the INTRAVAL Pilot Team in defining and reporting on the Apache Leap Tuff experiments and intercomparison modeling efforts.

ACKNOWLEDGEMENTS

This research was funded by the US Nuclear Regulatory Commission (NRC) under contract number NRC-04-90-053. The NRC project monitor was Thomas J. Nicholson. Additional funding was provided by the Center for Nuclear Waste Regulatory Analyses (CNWRA) under subcontract number 65626. The CNWRA project monitor was Dr. John Russell. Appreciation is noted for the technical assistance provided by Ingrid Anderson, James Devine, Charles Lohrstorfer, Michael Henrich, Dick L. Thompson, and for the guidance provided by Daniel Evans.

1. INTRODUCTION

Todd C. Rasmussen

1.1 Overview

Long-term projections of radionuclide transport through unsaturated fractured rock in the vicinity of a high-level nuclear waste repository require that relevant processes and parameters be identified, and that numerical models be formulated to provide estimates of mass transport over geologic time scales. Processes relevant to radionuclide transport considered here include fluid flow (as water, air, and water vapor), heat flow (by conduction, radiation, advection, latent heat transport and convection), and solute transport by advection and diffusion. Additional processes may be relevant to radionuclide transport (e.g., thermo-mechanical deformation, biological, and geochemical processes) but are not considered here.

Of primary concern is the nonisothermal behavior of fluid flow near the waste repository. Complex fluid behavior is expected due to the coupling of fluid, heat and solute transport processes. Additional complexities arise due to the heterogeneous properties of unsaturated, fractured rock. High-permeability macropores in the subsurface (e.g., faults, fractures, worm- or root-holes) can substantially affect the migration of water and entrained solutes [see, e.g., Krishnamoorthy et al., 1992; Norris, 1989], as well as vadospheric gasses [Weeks, 1987]. Models of fluid flow through unsaturated fractured rocks must account for the complex processes associated with matric-potential-dependent flow in strongly heterogeneous media, including aperture variability within fractures, variations in fracture network continuity and interconnectivity, and flow interactions with the enveloping porous media.

Conceptual, mathematical, and numerical models are necessary to investigate the behavior of flow and transport through fractured rock or any geologic media containing macropores. The objective of any model development strategy should be to obtain a parsimonious yet rigorous formulation of the flow and transport behavior that is computationally efficient, physically justifiable, and experimentally confirmed. The modeling and characterization of these complex phenomena can be placed in a hierarchical conceptual framework (Figure 1.1). Grouped at the finest scale are processes related to flow in individual fractures, which may be termed intrafracture flow processes. Important features associated with this scale include aperture variability and continuity of pores within a fracture plane which give rise to flow channeling, hysteresis effects and microdispersion. A courser scale focuses on flow through networks of interconnecting discrete fractures, which may be termed interfracture flow processes. The distribution of fracture orientations and the character of interconnections between fractures are important at this scale because of their influence on the macroscopic paths of flowing fluids. Another scale incorporates the effects of the porous rock matrix on flow behavior, which may be termed suprafracture flow. Fracture surface sealing and matrix hydraulic properties introduce additional complexities at this scale [Thoma et al., 1992]. Also important are the effects of flow refraction across fractures for fluids moving from matrix block to block, and flow funneling from enhanced saturation above inclined fractures that may serve as capillary barriers [Oldenburg and Pruess, 1993].

1.2 Previous Research

Nordqvist et al. [1992] and Dverstorp et al. [1992] present a variable aperture network model for saturated flow that incorporates both intra- and interfracture variability for saturated flow. Lacking from the model are the effects of coupled fracture-matrix interactions and the effects of unsaturated conditions. Krishnamoorthy et al. [1992] examine the effects of suprafracture chemical reactions, yet

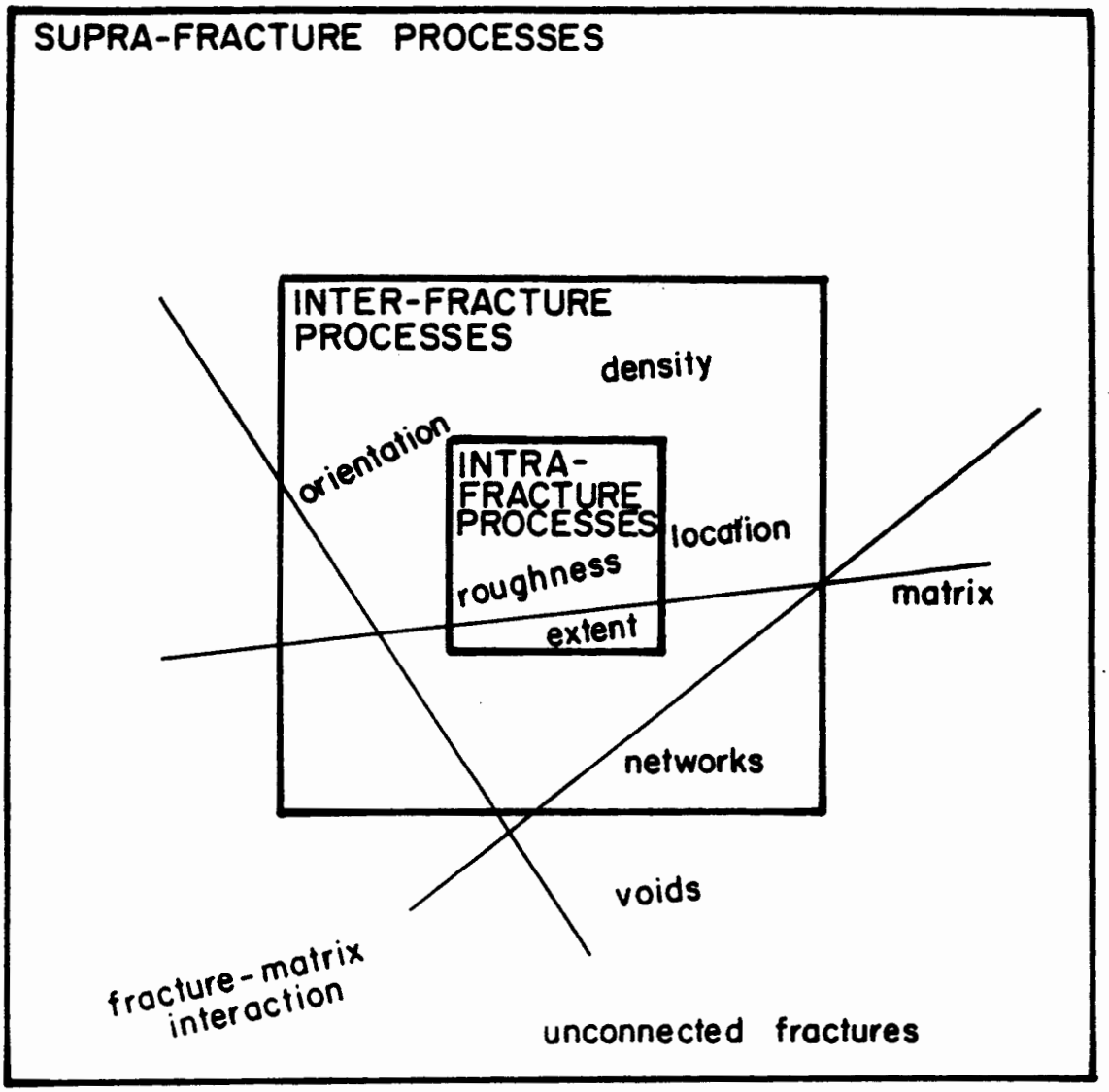

Figure 1.1: Hierarchical structure of fracture flow and transport processes.

neglect processes relevant to flow channeling within and between fractures. Martinez et al. [1992] examine the effects of finite, discrete, repetitive, impermeable, horizontal fractures on unsaturated flow. By neglecting the spatial variations of fracture and matrix hydraulic conductivity, as well as the matric-potential-dependent hydraulic properties of fractures, they demonstrate a smaller reduction in apparent rock matrix hydraulic conductivity than for saturated conditions.

Of interest in the study reported here are the processes relevant to fluid, thermal, and solute transport in unsaturated fractured rock. One method for describing fluid flow through macropores embedded within porous matrix uses a dual-continuum approximation in which flow and transport through the rock matrix is assumed to be less significant than flow within fractures, or flow and transport interactions between between the rock matrix and fractures [see, e.g., Gerke and Van Genuchten, 1992]. One alternative to the dual-continuum model was proposed by Nitao and Buscheck [1991] which provides an approximate analytic solution for the advancement of a wetting front through unsaturated rock with embedded fractures of arbitrary orientation. The fractures are assumed to be infinite in areal extent and may be repetitively spaced. The conceptual and mathematical model identified three stages in the fracture imbibition process. The first stage consists of rapid water imbibition into a dry fracture in response to a specified head or flux at the terminus of the fracture. The initial rapid intake slows in the second phase as water advances in both the rock matrix and fracture. The final phase begins when the water wetting front in the rock matrix encounters an axis of symmetry resulting from the existence of nearby fractures, or an impermeable rock matrix boundary parallel to the fracture.

1.3 Objectives

The focus of this document is to provide characterization and calibration data sets that can be used to evaluate conceptual and numerical models. The evaluation consists of two components, verifying the existence of proposed processes and verifying the parametric form of hypothesized material properties. Hypothesized parametric equations are evaluated by independently estimating material properties of the rock matrix and embedded fracture. Several sections present characterization data sets that can be used to construct prediction models of the behavior of fluid, heat and solute migration through unsaturated fractured rock.

An additional objective is the development of characterization techniques suitable for field-scale characterization of unsaturated fractured rocks relevant to the proposed conceptual and analytic models. To this end, fluid and heat flow experiments were performed to investigate the behavior of coupled transport. These experiments were performed for the purpose of evaluating alternate methodologies for *in situ* characterization of unsaturated fractured rock transport properties. Utilization of experimental techniques developed from laboratory scale experiments to experiments at field scales is the logical next step for model evaluation.

Estimates of parameter uncertainty were incorporated in the characterization experiments to quantify prediction accuracy. Three techniques were used to estimate parameter uncertainties; replication, duplication, and redundancy. Replication was performed by repeating experiments using the same sample for the purpose of estimating experimental errors. Duplication was performed by using different samples for the purpose of estimating geologic variability. Redundancy was performed by employing dissimilar techniques to estimate the bias associated with an individual measurement technique.

2. ROCK MATRIX CHARACTERIZATION

Shirley C. Rhodes

Characterization of the properties of volcanic tuff matrix from the Apache Leap Tuff Site, white unit, was performed on oriented cylindrical cores taken from a single rock sample collected at the site. The cores are 6 cm in diameter and range from 2.39 to 2.69 cm in height. Matrix properties were obtained using laboratory procedures, and the parameters estimated from those experiments apply to fractured rock and nonisothermal flow characterizations as described elsewhere in this report. A description of matrix hydraulic properties follows, including sorption and desorption characteristic curves, hydraulic permeability curves, and air permeability and thermal conductivity properties, along with data sets and procedures employed to collect the data.

2.1 Characteristic Curves

Moisture characteristic curves relate the water content or relative saturation of a rock sample to the matric potential (matric suction) of the water in the sample. The desorption portion of the moisture characteristic curve is obtained using a pressure extraction vessel for the wet region (i.e., matric suctions less than 500 kPa), while saturated salt solutions are used to obtain data for drier regions (i.e., matric suctions greater than 500 kPa). The sorption portion of the moisture characteristic curve is obtained by reversing the order of the pressure increments applied in the procedures just mentioned, with some modifications to the pressure extraction vessel setup.

For matric suctions less than or equal to 500 kPa, a pressure plate extractor is used to regulate the matric potential within a core segment [Klute, 1986]. The system (shown in Figure 2.1) utilizes a computer monitored on-off solenoid, pressure transducer, and bleed-off solenoid to control pressure in the extraction vessel to within 2 kPa. All experiments were performed in a constant-temperature laboratory at 20°C. Beginning with a vacuum-saturated core segment (shown in Figure 2.2), the procedure consists of placing the segment on the porous ceramic plate of the pressure extraction vessel (with a No. 42 Whatman filter paper lying between the sample and the plate for good hydraulic connection), sealing the vessel, and applying pressure using nitrogen gas. The imposed external pressure of the gas will result in an equivalent matric suction within the core segment upon equilibration. Once the sample has reached equilibrium, the pressure is released, the vessel is opened, and the core sample is weighed to calculate volumetric moisture content. The core is returned to the extraction vessel, and a greater pressure is applied. Pressures of 10, 25, 50, 100, 300, and 500 kPa were applied to the cores using this method, and corresponding water contents and relative saturations were determined for the core samples.

For matric suctions greater than 500 kPa, saturated salt solutions were used to impose the desired potential on core segments. At saturation, different salt solutions will have different known potentials, which create specific relative humidities in their immediate environments. The water potential in the vapor phase associated with those relative humidities creates a vapor pressure gradient, which provides the mechanism for moisture sorption and desorption. Core samples were positioned just above a saturated salt solution on a lattice, within a closed Lucite desiccator chamber. This arrangement assures maximum exposed sample surface area and minimum separation between sample and osmotic medium, both factors in reducing equilibration time [Campbell and Gee, 1986].

Samples were allowed to equilibrate within the chamber. They were regularly weighted to determine their volumetric moisture content. The salts used for this procedure were lead nitrate, $Pb(NO_3)_2$, zinc sulfate heptahydrate, $ZnSO_4 \cdot 7H_2O$, and potassium bromide, KBr, giving 2.7 MPa, 14.2 MPa, and 23.6 MPa, respectively. The water potentials associated with these specific salt

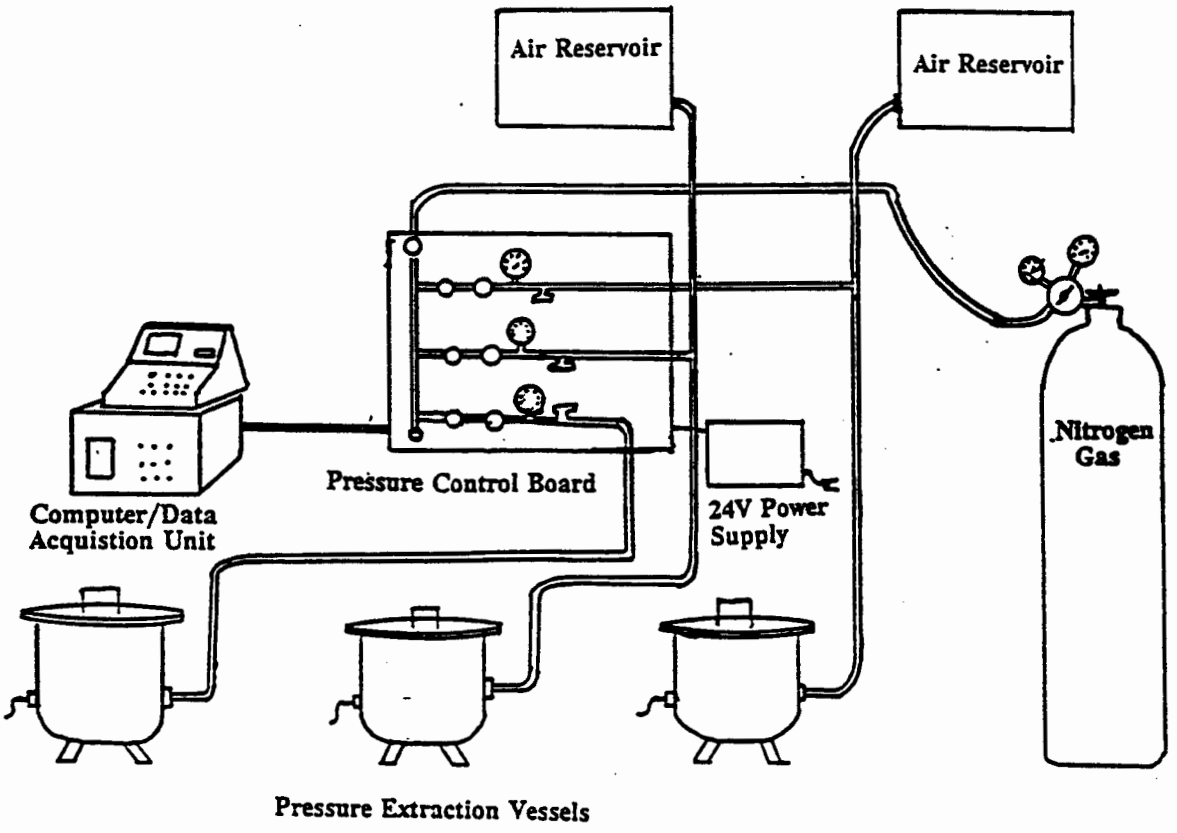

Figure 2.1: Computerized pressure control system schematic.

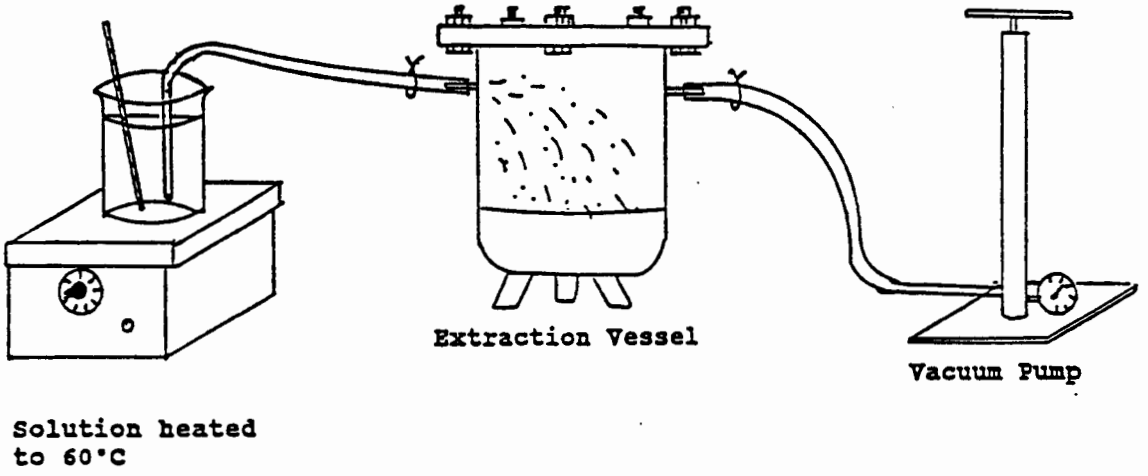

SOLUTION DEAERATION SETUP

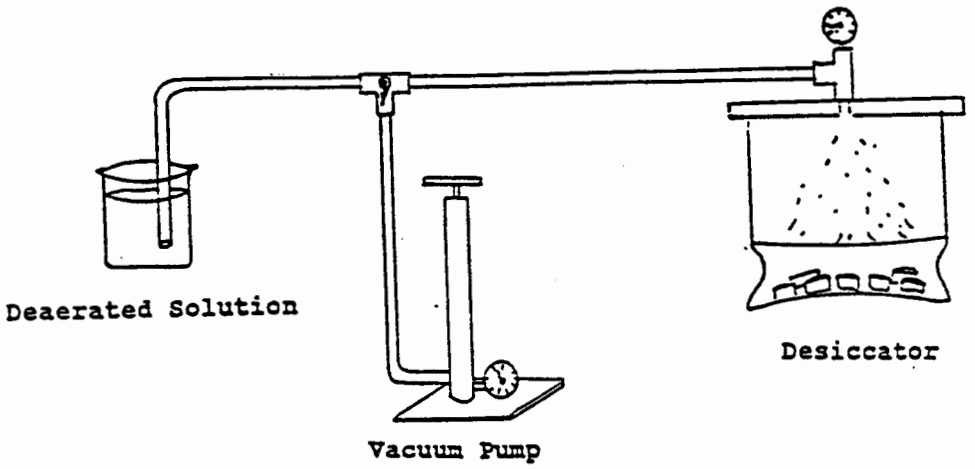

CORE SATURATION SETUP

Figure 2.2: Solution deaeration and core saturation setup.

solutions were used to plot the moisture characteristic curves for the drier regions. These theoretical values are listed, for comparison, in Table 2.1, along with the relative humidities and water potentials that were measured using a hygrometer or thermocouple psychrometer. It should be noted that care must be taken when using hydrated salts. The salt crystals in equilibrium with the cores may or may not be the exact composition of the original salt.

Table 2.1
Relative humidity and water activity for saturated salt solutions.

	$PbNO_3$	$ZnSO_4$	KBr
Water Activity			
Theoretical	0.98	0.90	0.84
Hygrometer	0.97	0.91	0.88
Matric Potential, MPa			
Theoretical	2.73	14.2	23.6
Hygrometer	4.12	12.8	17.3
Psychrometer	5.71	-	-

The water sorption part of the characteristic curve was determined by reversing the order of the matric potential equilibration steps. In the case of saturated salt solutions, the cores were moved to a solution of higher humidity (i.e., a lower matric potential) than that used for the previous step. For sorption at 500 kPa or less, the pressurized apparatus was used, with a ceramic pressure plate which was modified so as to allow deaired solution to be pumped through the bladder under the plate [Klute, 1986]. A reservoir of solution and a slow-speed peristaltic pump provided the source. Equilibration was again in the reverse order of the pressure steps used for desorption.

Table 2.2 presents statistical summaries of water content and relative saturation data for pressure extractor and salt solution methods. The data presented indicate that the saturation of the matrix at a specified matric suction for these samples is consistent for 20 samples, with a coefficient of variation of the mean of less than 2%. Calculated statistical variance, assuming consistent methods and equipment, embodies both measurement error and geologic variation. To obtain variance due to measurement error, ten saturated rock segments were equilibrated at 500 kPa, in the manner already described. The procedure was repeated, giving two sets of water content data for the same set of ten cores. Variance of the data produced by the two experiments was calculated for each sample. Since each variance value was calculated for a single sample, the variance must consist only of measurement error. A mean was determined for the ten variance values, based on volumetric water content. Subtracting this value from the total variance, as calculated for twenty samples at each pressure step, has no significant effect. It must be concluded that the relatively small amount of total variance observed in the set of samples examined here is due almost entirely to geologic variation.

Table 2.2
Summary water content data for Apache Leap Tuff cores

	Matric Suction (kPa)									
	0	10	25	50	100	300	500	2,730	14,240	23,570
Desorption										
Number	20	20	20	20	20	20	20	20	20	20
Mean	0.166	0.161	0.160	0.155	0.140	0.111	0.086	0.058	0.030	0.023
Coef. Var.	0.011	0.011	0.010	0.009	0.011	0.019	0.017	0.010	0.014	0.011
Minimum	0.148	0.143	0.142	0.143	0.121	0.091	0.076	0.054	0.027	0.021
Median	0.155	0.162	0.160	0.155	0.142	0.111	0.084	0.058	0.030	0.023
Maximum	0.178	0.174	0.172	0.166	0.151	0.128	0.097	0.063	0.035	0.025
Absorption										
Number	0	10	10	10	10	10	20	20	20	0
Mean	-	0.136	0.129	0.115	0.094	0.075	0.060	0.028	0.025	-
Coef. Var.	-	0.014	0.012	0.014	0.018	0.022	0.021	0.011	0.010	-
Minimum	-	0.128	0.123	0.106	0.086	0.068	0.051	0.025	0.022	-
Median	-	0.134	0.128	0.115	0.094	0.074	0.061	0.028	0.024	-
Maximum	-	0.146	0.137	0.123	0.101	0.086	0.072	0.031	0.027	-

Hysteresis describes the phenomenon of inconsistent moisture content and distribution with respect to matric potential that occurs during the history of wetting and drying of matrix material. At any given potential, moisture content of a wetting matrix is less than that of a drying matrix. Just as moisture sorption and desorption curves are characteristic of the matrix material from which they are derived, hysteresis scanning curves are influenced, additionally, by the water content and matric potential status of the matrix material at the point the wet-dry cycle is reversed.

Ten volcanic tuff samples were vacuum saturated, then placed in a pressure outflow apparatus at 500 kPa to desorb as described previously. After equilibration at 5 bars, the cores were replaced in the pressure apparatus with a wetting plate designed to provide deaired solution as the cores sorbed solution under decreasing pressure, at steps 300, 100, 50, 25, and 10 kPa. Figure 2.3 shows the entire desorption-absorption curve, with the single hysteresis scanning curve while Table 2.3 presents the statistical summaries.

Table 2.3
Water absorbtion data for Apache Leap Tuff cores (wetting from 500 kPa).

	Matric Potential (kPa)					
	10	25	50	100	300	500
Volumetric Water Content						
Number	10	10	10	10	10	10
Mean	.1317	.1254	.1120	.1017	.0917	.0838
Coef. Var.	1.06 %	1.91 %	1.90 %	2.19 %	2.78 %	2.48 %
Minimum	.1250	.1074	.1021	.0919	.0829	.0753
Median	.1319	.1287	.1113	.1003	.0887	.0842
Maximum	.1366	.1334	.1241	.1132	.1048	.0958
Relative Saturation						
Number	10	10	10	10	10	10
Mean	92.77	88.30	78.88	71.70	64.74	59.08
Coef. Var.	0.805 %	1.43 %	1.8 %	2.35 %	3.38 %	2.54 %
Minimum	87.78	79.85	72.25	62.83	54.32	51.46
Median	92.85	89.47	78.57	71.99	64.35	61.15
Maximum	96.46	92.32	84.25	78.09	78.92	65.93

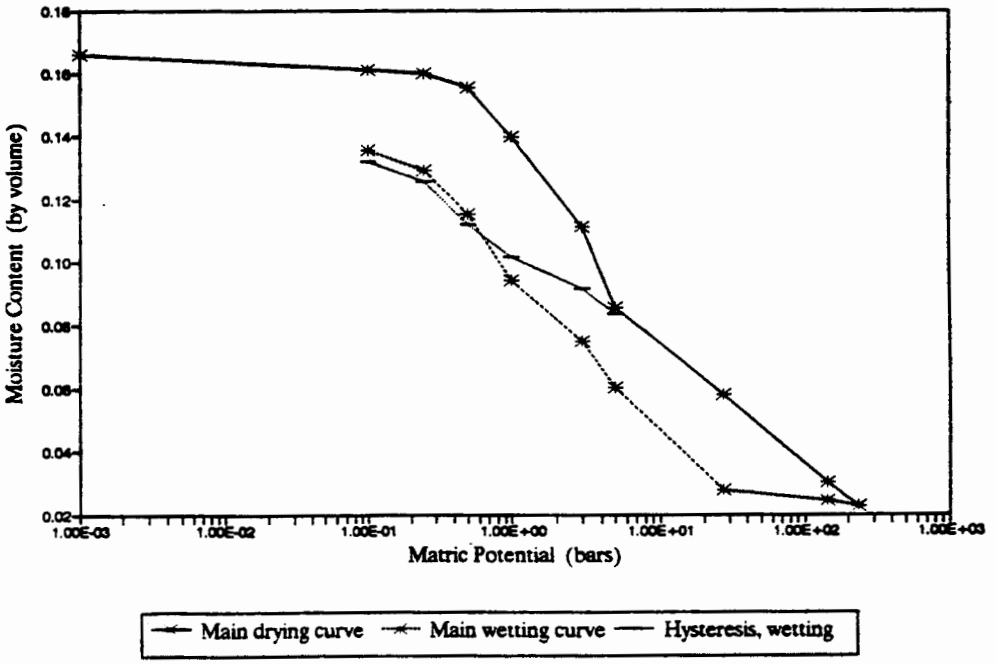

Figure 2.3: Moisture characteristic curves incorporating hysteresis.

2.2 Unsaturated Hydraulic Conductivity

Hydraulic conductivity for geologic materials decreases as moisture content decreases, or as the matric suction increases. The outflow method was used to obtain data for both saturated hydraulic conductivity and intrinsic permeability, with slight differences in technique. While all core segments were vacuum saturated, those used for saturated hydraulic conductivities were "packed" in a cylinder with water-proof caulking, leaving both upper and lower surfaces unobstructed (shown in Figure 2.4). This arrangement allows flow through the core only. In the constant-temperature laboratory at 20°C, samples were placed in a Tempe pressure cell, and a pressure increment was applied, either as solution under pressure for saturated flow or as humidified gas for unsaturated flow. Rate of outflow from the pressure cell was monitored using a small capacity pipette and an injected air bubble, or by directly measuring accumulated outflow in a calibrated buret. Air trapped at the bottom of the porous plate was removed with a recirculation pump [Klute and Dirksen, 1986].

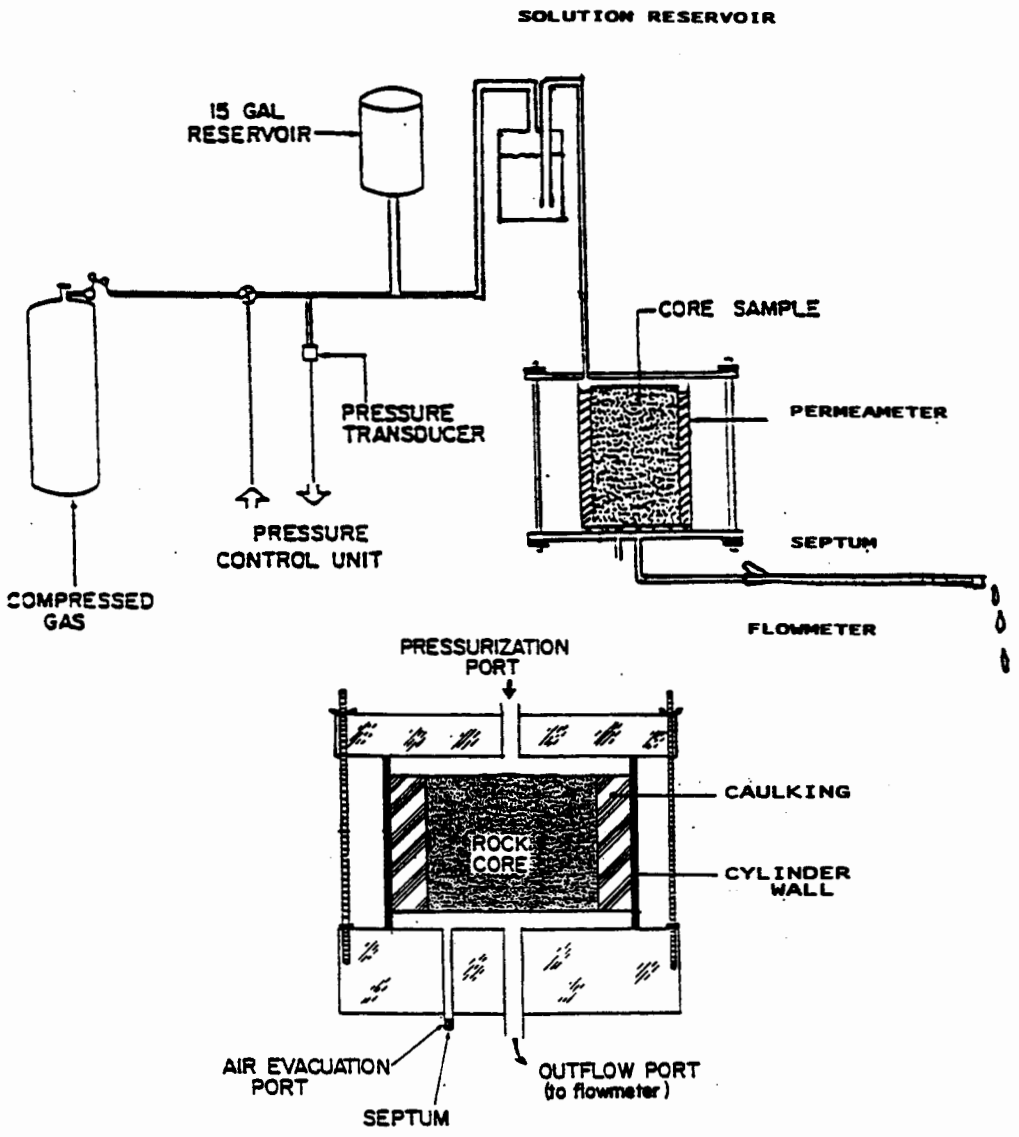

Figure 2.4: Permeameter schematic for saturated hydraulic conductivity.

An analytical form of the cumulative outflow function:

$$1 - \frac{Q(t)}{Q(\infty)} = \frac{8}{\pi^2} \sum_{m=0}^{\infty} \frac{1}{(2m+1)^2} \exp\left[\frac{-(2m+1)^2 \pi^2 \, Dt}{4L^2}\right] \tag{2.1}$$

was used to construct a theoretical plot of the quantities log [1 -Q(t)/Q(∞)] versus log ($Dt/4L^2$). On the same type of log-log graph paper, the quantity log [1 - Q(t)/Q(∞)] versus log t was plotted for the experimental data. Curve-matching technique was employed by translating along the log ($Dt/4L^2$) axis only, and reading the corresponding value of t from the experimental curve. If w represents the chosen value of $Dt/4L^2$ and t is the experimental value of time corresponding to the chosen value of w [Klute, 1964], then diffusivity is given by:

$$D = w L^2 / t \tag{2.2}$$

For sample volume, V, and steady state outflow, Q(∞), the specific water capacity is given by:

$$C = Q(\infty) / (V \Delta h) \tag{2.3}$$

and hydraulic conductivity is given by:

$$K = D C \tag{2.4}$$

Conductivity values were converted to hydraulic permeability values, for which summary statistics are provided as Table 2.4.

Table 2.4
Permeability of Apache Leap Tuff using water (units of 10^{-14} m^2).

	Matric Suction (kPa)				
	0	10	25	50	100
Number	10	5	2	2	13
Mean	42.7	142.0	69.1	0.49	0.630
Coef. Var.	14.9 %	68.7 %	70.0 %	89.1 %	29.2 %
Minimum	13.9	1.23	6.86	0.276	0.092
Median	39.6	73.3	-	-	0.410
Maximum	87.6	522.0	6.96	4.71	2.46

2.3 Pneumatic Permeability

Pneumatic permeability was measured using the permeameter set-up described in Section 2.2, with the core segments sealed so as to allow no bypassing of flow around the outside of the sample (shown as Figure 2.5). This test was performed in a constant temperature room at 20°C, on both oven-dried and partially saturated cores. In the latter case, nitrogen was bubbled through a reservoir to increase the humidity of the gas. The flow rate was obtained through oven-dried cores by applying a known pressure gradient longitudinally across the core segment, at total potential differences of 20 and 40 kPa, and measuring air flow volume with a calibrated bubble flowmeter. The partially saturated samples, equilibrated by the methods and at pressure steps to 100 kPa as described for moisture characteristic curves, were tested at 7, 20 or 40 kPa, always less than the equilibration status. Atmospheric pressure was monitored, and those values, ranging from 96 to 102.5 kPa on different days, were incorporated into the calculation of pneumatic permeability. The pneumatic permeability at each matric potential is calculated using the measured air flow rate, cross sectional area and core segment length. The ideal gas law is employed and flow is assumed to be isothermal:

$$k_a = 2\,Q\,L\,P_o\,\mu/A\,(2\,P_o\,\Delta P + \Delta P^2) \qquad (2.5)$$

where k_a pneumatic permeability, m^2;
Q measured flow rate, m^3/s;
L,A core length, m, and cross sectional area, m^2;
μ viscosity of nitrogen gas, Pa s;
P_o outflow pressure head (atmospheric), Pa
ΔP imposed pressure gradient, Pa.

Table 2.5 summarizes test results. Theoretically, the air permeability of an oven-dried sample should be the same as the water permeability of the sample at saturation. In practice, however, permeability estimates may not be similar due to the phenomenon of slip flow along the walls of pores [Klinkenberg, 1941]. The importance of the Klinkenberg phenomenon can be evaluated by comparing the computed air permeability for oven-dried cores with the computed water permeability for completely saturated cores. The two values should be a function of the ambient air pressure used to conduct the air permeability test, as well as the mean free path of the gas molecules and the pore diameter.

Table 2.5
Permeability of Apache Leap Tuff using air (units of 10^{-14} m^2).

	Matric Potential (kPa)						
	10	25	50	100	300	500	oven-dried
Number	8	3	7	6	6	6	9
Mean	-	0.0057	0.073	0.077	0.160	0.113	0.824
Coef. Var.	-	95.3 %	95.8 %	82.2 %	80.6 %	54.6 %	56.1 %
Minimum	-	0.000084	0.00012	0.00013	0.0114	0.0293	0.102
Median	-	0.00045	0.00592	0.00263	0.0033	0.0563	0.127
Maximum	-	0.0166	0.493	0.390	0.801	0.417	3.33

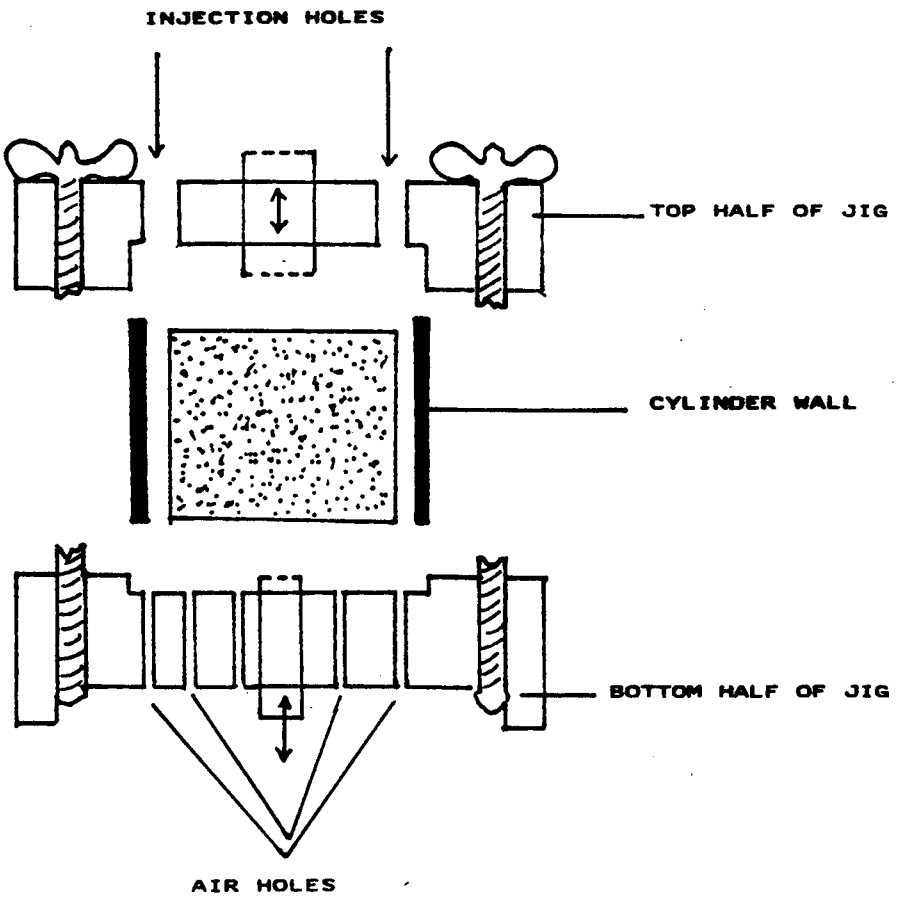

Figure 2.5: Permeameter schematic for air permeability.

2.4 Thermal Conductivity

Because thermal gradients can substantially affect the movement of water as liquid and vapor in the subsurface, characterization of the moisture-dependent thermal properties of the rock matrix is important for modeling the thermal effects on fluid and solute transport. This section presents laboratory data sets for thermal parameters corresponding to samples consistent with other data sets given in this report.

To estimate thermal properties of the rock matrix, modifications were made to a method [Ashworth, 1990] where core segments were "sandwiched" between a set of copper disks with thermistors and a set of heat exchangers, as shown in Figure 2.6. The "heat flux meter" of copper-nylon-copper disks, positioned on the top surface of the core, was the mechanism by which the amount of heat flux entering the segment could be measured. A thermal gradient was imposed vertically through the sample, and the steady state temperature of the core was evaluated with the thermistor-copper disk at the core's lower surface. By using materials of known thermal conductivity and low thermal resistivity where appropriate, Fourier's Law can be used to calculate thermal diffusivity for core samples of known length. First, obtain the amount of heat flux being applied:

$$f_h = K_T \, dT/dx \tag{2.6}$$

where f_h heat flux;
K_T thermal conductivity of nylon disk;
dT change in temperature across nylon disk, T_1-T_2;
dx thickness of nylon disk.

Rearranging the equation to solve for thermal conductivity of the core segment yields:

$$K_T = f_h \, dx/dT \tag{2.7}$$

It must be noted that some moisture loss due to evaporation occurred during the course of the thermal conductivity measurements. Table 2.6 summarizes laboratory thermal properties. Figure 2.7 shows the nonlinear aspect of the relationship between rock matrix thermal conductivity and volumetric water content.

Table 2.6
Thermal conductivity of Apache Leap Tuff (units of W/m°C).

	- - - - Mean Volumetric Water Content - - - -			
	0.1502	0.0876	0.0267	0.0000
Number	10	9	3	9
Mean	1.899	1.574	1.382	1.305
Coef. Var.	1.34 %	1.93 %	2.99 %	2.82 %
Minimum	1.786	1.470	1.341	1.168
Median	1.864	1.540	1.341	1.289
Maximum	2.027	1.703	1.465	1.533

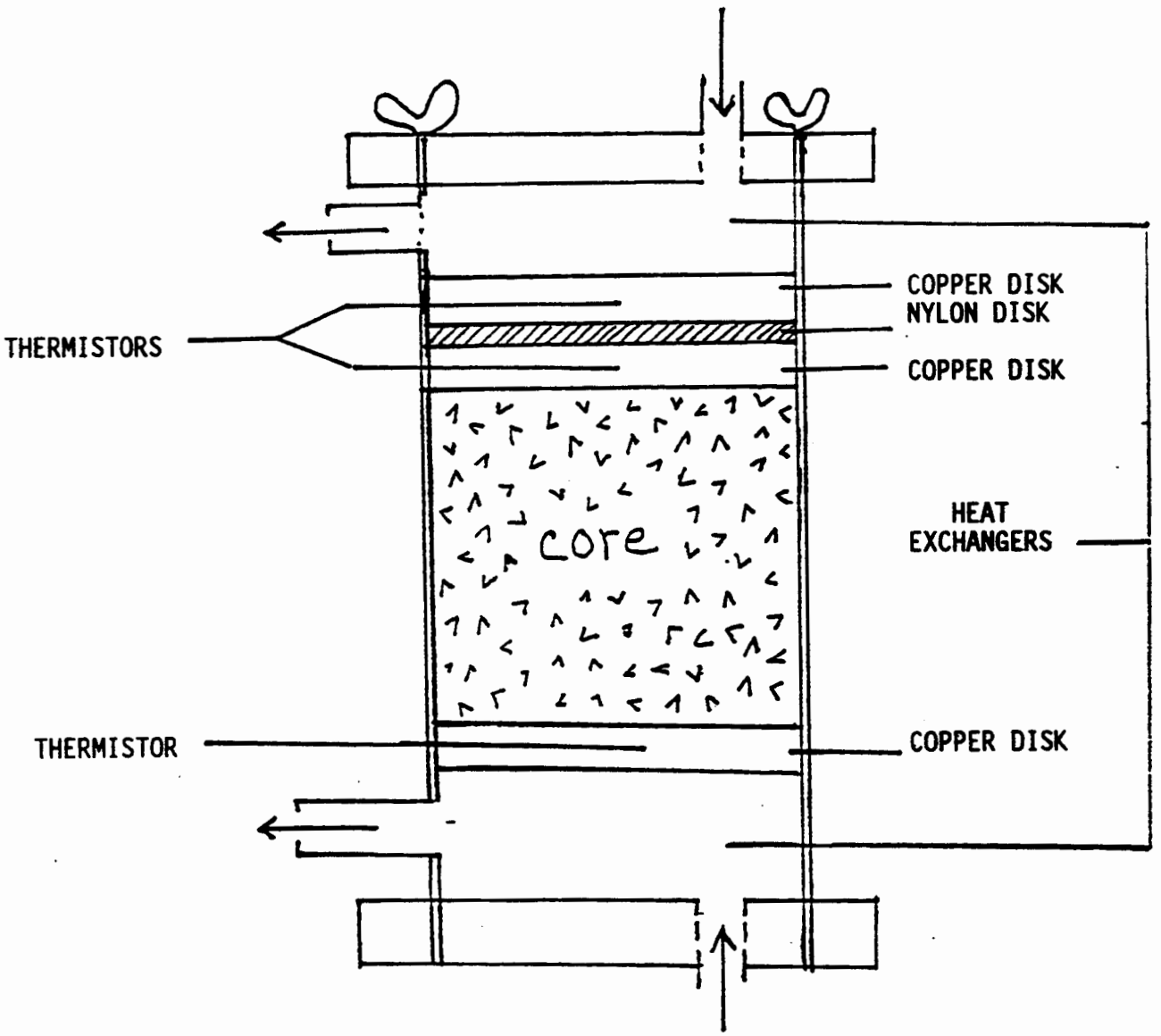

Figure 2.6: Thermal conductivity measurement schematic.

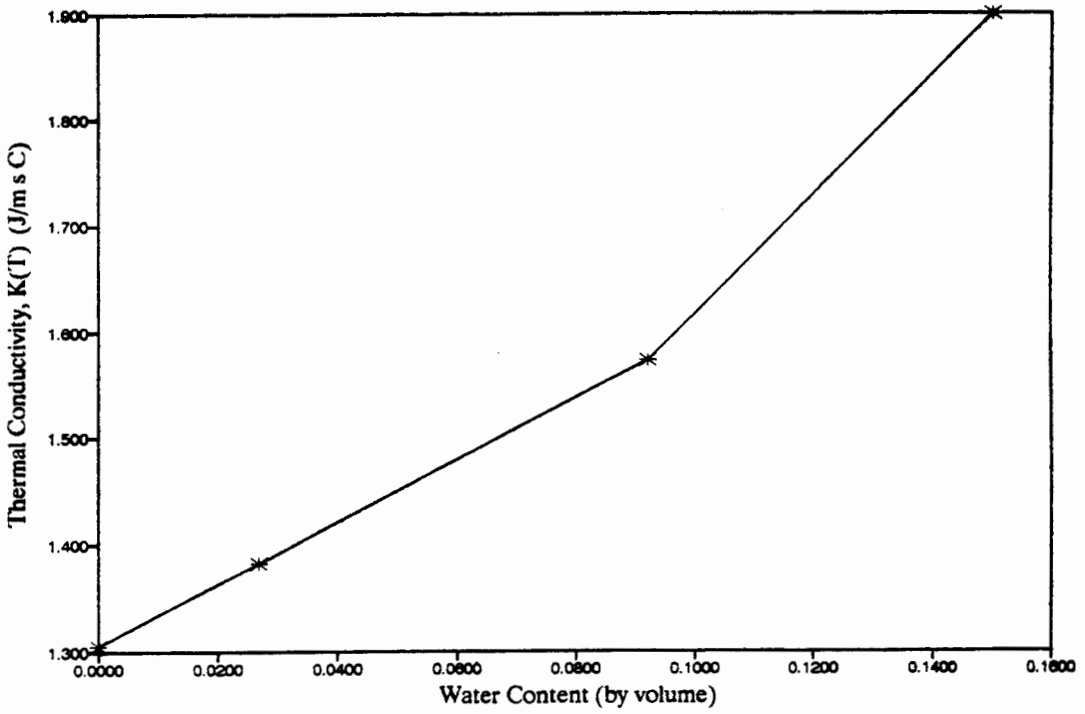

Figure 2.7: Measured water-dependency of thermal conductivity.

2.5 Discussion

Results of laboratory experiments conducted to characterize fluid and thermal flow parameters of unsaturated Apache Leap Tuff indicate that hysteresis influences the moisture characteristic curve. Sorbing and desorbing characteristic curves are markedly different, with the sorbing curve consistently showing higher matric potentials at equivalent water contents. Efforts to identify the matric potential from water contents of unsaturated rock will require knowledge of the water content history of the site. The successful application of osmotic solutions to maintain constant matric potentials was demonstrated. Saturated salt solutions present in the geologic environment may affect the observed matric potential. Near a repository, accumulations of soluble salts may affect the migration of liquid and vapor due to the osmotic potential induced at high salt concentrations. Coupling of salt concentrations with water activity should be an integral component of simulation models of fluid flow near the waste repository. Temperature is shown to affect the characteristic curve. Both reduced and increased temperatures cause substantial shifts in the characteristic curve, attributable to the change in the temperature dependence of the fluid surface tension. Coupling of hysteresis effects with temperature changes was not evaluated, nor were changes in the characteristic curves evaluated as a function of dynamic temperature changes. Additional characterization studies will be required to address the effects of temperature fluctuations on characteristic curves. The relative permeabilities for air and water were determined using rock cores. Estimates of permeabilities were obtained under isothermal conditions. The evaluation of relative permeabilities as a function of temperature was not experimentally determined. Additional experiments will be required to evaluate the importance of temperature on water and air relative permeability functions. The influence of water content on the thermal conductivity was examined using a one-dimensional heat cell. A linear relationship between water content and thermal conductivity was not clearly demonstrated. Observed mean thermal conductivities were less than expected for the range of volumetric water contents from 0 to 0.0876. Additional studies will be required to investigate the nature of the unsaturated thermal conductivity relationship, and the influence of hysteresis on the relationship.

3. NONISOTHERMAL CORE EXPERIMENT

Todd C. Rasmussen

Thermal energy sources can substantially affect air, water vapor, water liquid, and solute movement in geologic media, and particularly in unsaturated fractured rock. The ability to understand and to predict the outcome of coupled fluid, heat and solute transport experiments is essential for accurate modeling of water and solute migration near a subsurface thermal source, due to a geothermal gradient, or from solar heating at the earth's surface.

Experimental data are presented for evaluating the processes of multiple phase fluid flow under conditions of steady heat flux. One component of the experiment investigates the thermal and liquid changes in a partially saturated core, while a second component examines thermal, liquid and solute changes in a partially saturated core. These laboratory data provide data sets for the evaluation of models used to predict thermal, liquid, vapor, and solute transport as a result of a thermal gradient. During the heating phase the following phenomena are anticipated:

- o Liquid water near the warm end of the core will vaporize in response to an increase in the vapor pressure deficit, forming a zone of desiccation near the heat source.
- o Water vapor will move away from the warm end of the core due to total pressure and vapor pressure gradients.
- o Heat flux away from the warm end will occur as sensible heat conduction and latent heat transfer in the vapor phase.
- o As the temperature decreases away from the warm end, the vapor will condense at some distance from the heat source, forming a zone of liquid water accumulation.
- o Liquid water will move from the zone of accumulation toward drier regions due to liquid phase potential gradients.
- o Solute concentrations will affect the liquid and vapor potentials due to osmotic effects.

The conceptual model described above is more precisely defined mathematically using the formulations described here. The general conservation equation for uncoupled processes is:

$$\nabla \cdot q_i = \nabla \cdot (K_i \nabla \phi_i) = C_i \, \partial \phi_i / \partial t + Q_i \tag{3.1}$$

where

- ∇ divergence operator;
- q flux rate;
- K conductance term;
- C capacitance term
- ϕ potential term;
- Q source or sink term; and
- t time.

For fluxes which are coupled (i.e., a potential gradient in one process induces flux in a different process), the corresponding constitutive relationships are:

$$q_i = - \Sigma_j K_{ij} \nabla \phi_j \qquad C_i = f(\phi_j) \qquad K_i = f(\phi_j) \tag{3.2}$$

This set of constitutive relationships state that flux of species i can be induced by a gradient of process j through the coupling term K_{ij}, and that both the uncoupled capacitance and conductance terms for species i can be affected by the potential term for process j. Combining the Equations (3.1) and (3.2) yields a coupled processes relationship of the form:

$$\nabla\cdot[\Sigma_j(K_{ij}(\phi_k)\ \nabla\phi_j)]_i = C_i(\phi_k)\ \partial\phi_i/\partial t + Q_i \qquad (3.3)$$

It should be noted that such parameters as the thermal conductivity and heat capacity are significantly affected by the water content and the solute concentration, yet only slightly affected by gas pressure. Two of the state variables (pressure head and vapor pressure) can be related to each other using Kelvin's equation, if the two potentials are in equilibrium.

Five nonisothermal experiments were conducted using the large core. The large core geometry measured 12.2 cm in length and 9.6 cm in diameter. The five experiments were proposed in order to provide a logical progression of experimental and theoretical complexity from one experiment to the next. Data obtained during the five experiments included water, temperature and solute content profiles along the large core. The same boundary conditions were employed in each case. Material properties were assumed to remain unchanged from one experiment to the next. The initial conditions were varied in the following manner:

- o Oven dry, solute free;
- o Water saturated, NaI solute absent;
- o Partially saturated, NaI solute absent;
- o Water saturated, NaI solute present; and
- o Partially saturated, NaI solute present.

In addition to the changing initial conditions indicated above, the following large-core initial conditions were employed:

- o Air pressure was atmospheric at approximately 93 kPa.
- o The initial core temperature was 22°C.

The initial conditions can be summarized as:

Experiment	1	2	3	4	5
ψ	∞	0	500	0	500
C_s	0	0	0	0.05	0.05

P_o = 93 kPa T_o = 22°C

where ψ matric suction, kPa;
C_s solute molar concentration;
P_o initial total gas pressure, kPa; and
T_o initial core temperature, °C.

The large-core boundary conditions during all heating experiments were:

- o No flow water, air and solute boundary conditions on all surfaces.
- o Steady temperatures of approximately 7 and 42°C at either end, with no flow thermal conditions along the sides of the core cylinder.

3.1 Experimental Setup

A cylindrically shaped core 12.2-cm long and 9.6-cm in diameter was extracted from a block of Apache Leap Tuff (white unit). The large core is used for the experiment, while smaller, "small" cores were also extracted from the block for characterization purposes (described in the previous section). The large core with a prescribed initial matric suction and solute concentration was sealed and insulated to prevent water, air and solute gains or losses on all surfaces, and to minimize heat loss along the sides of the core.

During the experiment, a horizontal temperature gradient was established along the long axis of the core. Thirteen thermistors were situated along the core at approximately 1-cm intervals to record temperature over time (about twice weekly). A dual-gamma source (Figure 3.1) used to determine the water and solute content along the core over time. Each gamma-ray reading measured a 1-cm diameter cylinder of rock. Each reading was 0.5 cm apart and overlapped neighboring measurements (Figure 3.2). There were a total of 22 readings at each observation time. The attenuation method uses the following relationships:

$$(C/C_o)^{am} = \exp(-\mu^{am}_r\, m_r - \mu^{am}_w\, m_w - \mu^{am}_s\, m_s) \tag{3.4a}$$

$$(C/C_o)^{cs} = \exp(-\mu^{cs}_r\, m_r - \mu^{cs}_w\, m_w - \mu^{cs}_s\, m_s) \tag{3.4b}$$

where

$(C/C_o)^{am}$	ratio of americium counts through core to counts through the atmosphere;
$(C/C_o)^{am}$	ratio of cesium counts through core to counts through the atmosphere;
m_r	mass of rock;
m_w	mass of water;
m_s	mass of solute;
μ^{am}_r	attenuation coefficient through rock for americium;
μ^{cs}_r	attenuation coefficient through rock for cesium;
μ^{am}_w	attenuation coefficient through water for americium;
μ^{cs}_w	attenuation coefficient through water for cesium;
μ^{am}_s	attenuation coefficient through solute for americium; and
μ^{cs}_s	attenuation coefficient through solute for cesium.

Due to the time required by the detector to respond to individual photon captures, a correction was made to each count to compensate for instrument deadtime. This correction takes the form:

$$C^{am}_{corr} = C^{am} / (1 - \tau^{am}\, C^{am}) \tag{3.5a}$$

and

$$C^{cs}_{corr} = C^{cs} / (1 - \tau^{cs}\, C^{cs}) \tag{3.5b}$$

where

C_{corr}	corrected count;
τ^{am}	americium counting deadtime, 1.32 μs; and
τ^{cs}	cesium counting deadtime, 1.12 μs.

1 Power Supply
2 High Voltage Power Supply
3 Timer
4 Six Digit Counter
5 AGC Amplifier
6 Linear Amplifier
7 Gamma Detector
8 Lead Detector Shield
9 Gamma Beam Collimator
10 Cs-137 Gamma Source
11 Lead Source Shield
12 Aluminum Track
13 Endplate Reservoir
14 Insulation
15 Precooled Water Inlet
16 Precooled Water Outlet
17 Steel Frame

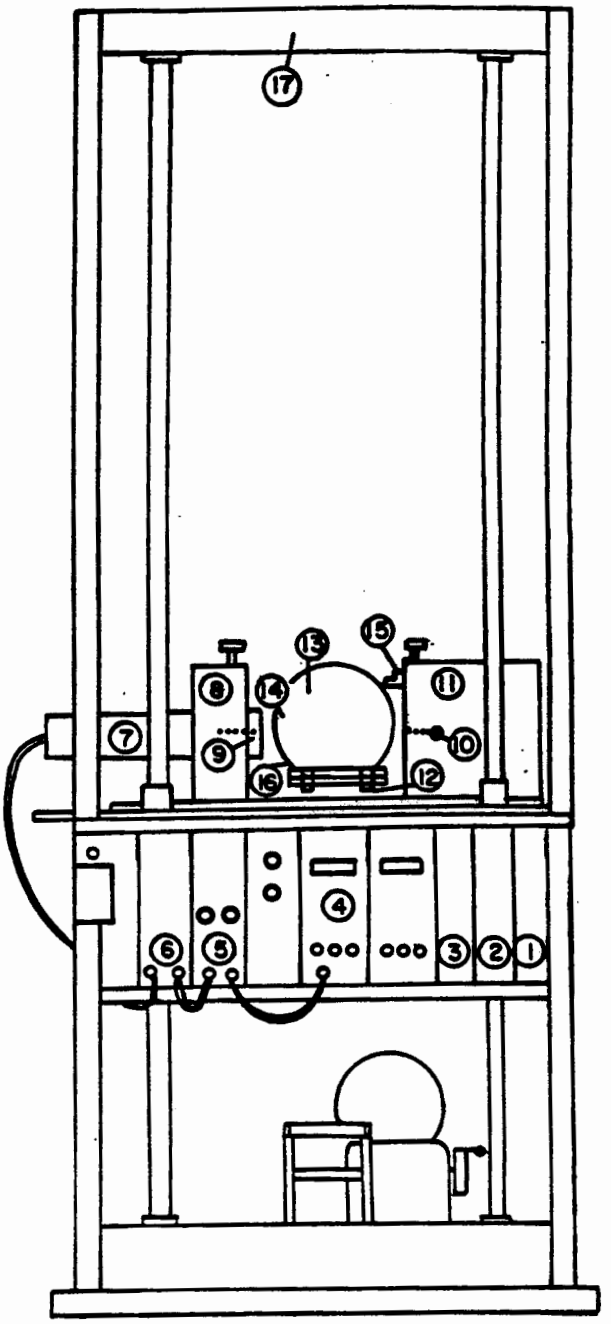

Figure 3.1: Dual-gamma attenuation equipment

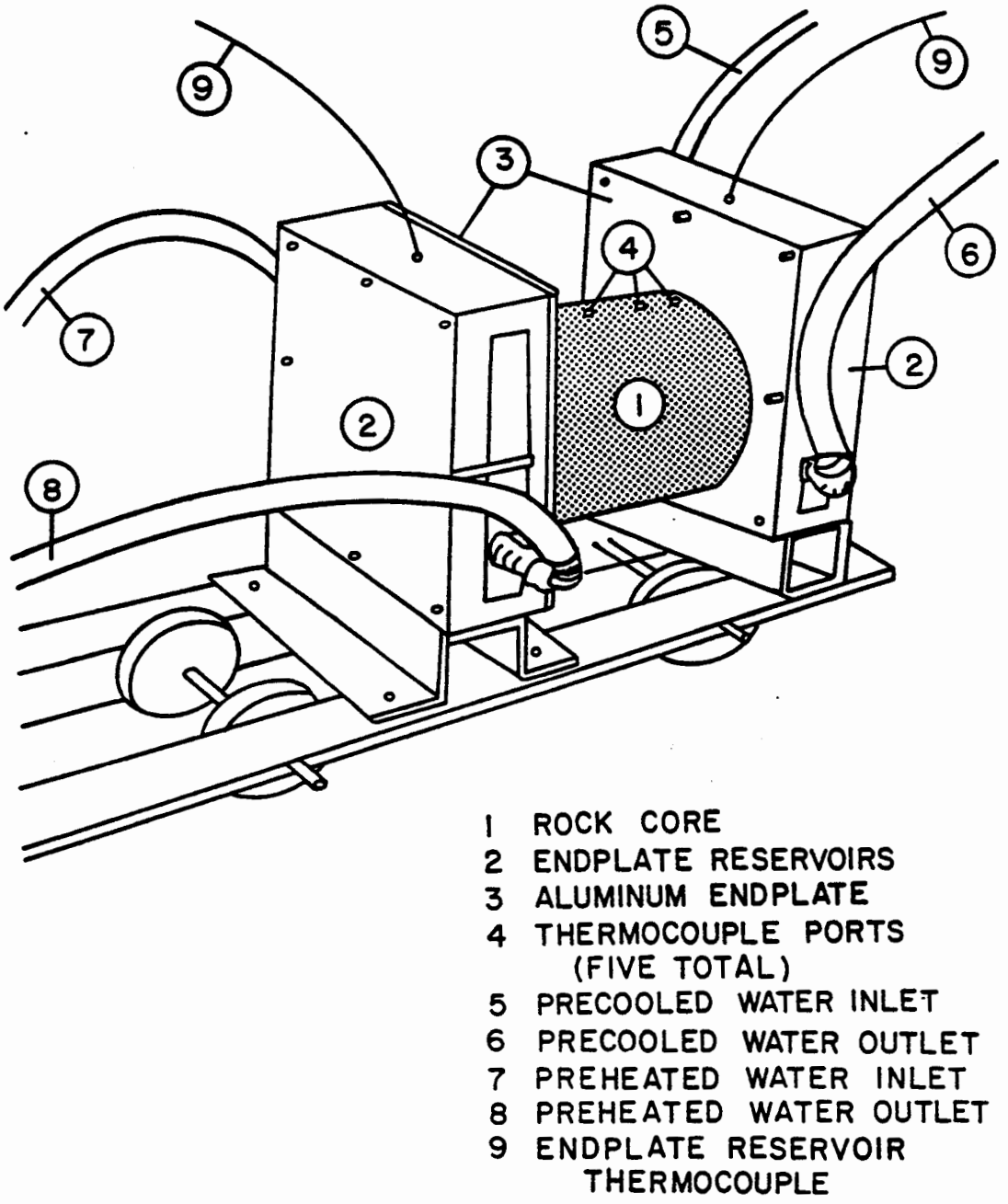

Figure 3.2: Large core experimental setup

An additional complexity results from spurious americium photon counts generated within the detector by the cesium source. To correct for the spurious americium counts a 5 M solution of NaI was used to eliminate any americium photons from entering the detector. The number of americium counts resulting from only the cesium source was obtained and used to correct the americium counts when the NaI solution was not present using the relationship:

$$C^{am}_{corr} = C^{am} - \alpha\, C^{cs} \tag{3.6}$$

where α is the ratio of spurious americium counts to cesium counts obtained using the 5 M NaI solution. This technique for removing the spurious counts was shown to be equivalent to removing the americium source and counting the false americium counts resulting only from the cesium source.

Experiments conducted on the small cores (reported in the previous section) are used to provide characterization data regarding porosity, moisture characteristic curves (including hysteretic effects), saturated and unsaturated hydraulic conductivity, saturated and unsaturated air permeabilities. Similar data from 105 core segments at the Apache Leap Tuff Borehole Site are also available.

3.2 Solute Absent

The large core was saturated and then reduced to a tension of approximately 500 kPa using a ceramic plate in a pressure chamber (discussed in the previous section). Water contents over time are presented as Table 3.1. During the outflow experiment, the circumference of the large core was sealed, while the two ends were left open. The core was fully saturated and then one end of the core was placed on a pressure plate and a five bar (500 kPa) pressure was applied. The total weight of the core was measured on various dates, and used to develop a time series of core saturations. These data are suitable for interpretation using one-step outflow procedures. Interpretation of the outflow data can provide van Genuchten parameters [see, e.g., Kool and Parker, 1987]. Porosity and initial water contents are presented in Table 3.2 for 1-cm diameter cylinders situated perpendicular to the thermal gradient. Each estimate is obtained using Americium and Cesium gamma-attenuation counts located 0.5 cm apart along the 12 cm long core.

TABLE 3.1
Large core saturation vs. time using one-step outflow method.

Day	6	12	19	31	48	61	89	160
Saturation	0.9268	0.8792	0.8262	0.7731	0.7127	0.6798	0.6398	0.5791

TABLE 3.2
Large core initial saturation and total porosity.

Position #	Position (cm)	Initial Saturation	Porosity (%)
1	0.75	0.448	12.6
2	1.25	0.346	12.6
3	1.75	0.300	12.5
4	2.25	0.354	13.2
5	2.75	0.381	13.4
6	3.25	0.488	13.8
7	3.75	0.531	13.4
8	4.25	0.577	13.5
9	4.75	0.535	14.5
10	5.25	0.432	15.5
11	5.75	0.471	16.3
12	6.25	0.475	16.8
13	6.75	0.436	17.5
14	7.25	0.460	17.8
15	7.75	0.504	17.3
16	8.25	0.587	16.7
17	8.75	0.704	16.8
18	9.25	0.738	16.4
19	9.75	0.751	15.7
20	10.25	0.657	14.7
21	10.75	0.651	13.7
22	11.25	0.855	12.5

The average porosity using the values in Table 3.2 is 14.9 percent, and the average relative saturation is 53.1 percent. As can be observed in the table, the initial saturation is not uniform, with a distinct trend from one end of the core to the other. The water saturation trend is a probable artifact of the single-step outflow procedure employed to induce the initial conditions. For the initial part of the experiment, the end nearest the number 1 position was heated, while the end nearest the number 22 position was cooled. The initial conditions, prior to heating, can be summarized as:

- Water potential in the rock matrix is approximately 500 kPa, with a mean saturation of approximately 8.1 percent.
- Initial solute concentration is 0.005 M $CaSO_4$. No NaI solution is present for the first part of the experiment.
- Air pressure is atmospheric at approximately 93 kPa.
- The initial core temperature is 22°C.

ψ = 500 kPa
M_s/M_w = 0
P_o = 93 kPa
T_o = 22°C

where ψ matric suction
M_s mass solute
M_w mass water
P_o initial total gas pressure
T_o initial core temperature

The boundary conditions can be summarized as:

- o No flow water, air and solute boundary conditions on all surfaces.
- o Steady temperatures of approximately 7 and 42°C at either end, with no flow thermal conditions along the sides of the core cylinder.

$q_w = 0$ ∀ surfaces
$q_a = 0$ ∀ surfaces
$q_h = 0$ for sides of core cylinder
$T_1 = 7°C$ for cold end of core cylinder
$T_2 = 42°C$ for hot end of core cylinder

where

q_w water flux
q_a gas flux
q_h heat flux
T_1 temperature at cold end
T_2 temperature at hot end

Temperatures were measured using thirteen precision thermistors placed at approximately 1-cm intervals along the length of the core, from position 0 cm to position 12 cm in increments of 1 cm. The initial temperature was 22°C. Temperatures are reported in Table 3.3.

TABLE 3.3
Large core temperature observations (°C) vs. time.

Loc.	- - - - Time (minutes) - - - -								
(cm)	4	14	24	34	44	54	64	74	84
0	22.053	37.881	40.534	41.194	41.482	41.572	41.612	41.642	41.693
1	22.065	31.854	36.134	37.495	38.025	38.274	38.317	38.403	38.438
2	22.088	28.084	32.805	34.483	35.143	35.428	35.496	35.618	35.656
3	22.080	24.757	29.168	31.054	31.822	32.155	32.246	32.389	32.448
4	22.073	23.424	26.974	28.731	29.473	29.828	29.938	30.078	30.148
5	21.986	22.551	24.744	26.108	26.719	27.059	27.166	27.323	27.390
6	22.049	22.144	22.636	23.219	23.624	23.919	24.010	24.163	24.242
7	22.104	21.772	20.711	20.459	20.634	20.870	20.940	21.093	21.157
8	22.100	21.022	18.580	17.638	17.610	17.770	17.818	17.951	18.009
9	22.136	19.930	16.911	15.674	15.547	15.663	15.700	15.822	15.856
10	21.350	17.463	13.395	12.368	12.158	12.205	12.257	12.321	12.354
11	20.463	13.744	10.500	9.743	9.593	9.609	9.636	9.657	9.681
12	14.616	9.116	7.429	7.092	7.033	7.029	7.494	7.281	7.566

Loc.	- - - - Time (minutes) - - - -								
(cm)	94	104	117	124	250	1040	1365	2815	4315
0	41.733	41.733	41.743	41.743	41.743	41.977	41.987	41.956	41.977
1	38.508	38.508	38.525	38.525	38.525	38.691	38.718	38.639	38.569
2	35.725	35.732	35.755	35.755	35.747	35.878	35.932	35.840	35.801
3	32.520	32.547	32.579	32.573	32.560	32.626	32.692	32.573	32.514
4	30.231	30.254	30.301	30.295	30.266	30.301	30.372	30.231	30.183
5	27.477	27.508	27.550	27.545	27.519	27.488	27.570	27.416	27.364
6	24.338	24.352	24.396	24.396	24.365	24.325	24.409	24.259	24.202
7	21.240	21.259	21.304	21.301	21.274	21.187	21.267	21.135	21.049
8	18.082	18.098	18.140	18.137	18.114	18.057	18.140	18.031	17.932
9	15.936	15.942	15.974	15.974	15.945	15.859	15.934	15.845	15.719
10	12.418	12.413	12.444	12.440	12.411	12.330	12.390	12.366	12.217
11	9.727	9.716	9.731	9.725	9.687	9.556	9.595	9.560	9.383
12	7.851	7.744	7.780	7.744	7.067	6.852	6.900	6.887	6.761

TABLE 3.3: (continued)

Loc. (cm)	- - - - Time (minutes) - - - - 5785	10045	14365	15805	18905	24745
0	41.936	41.956	41.743	41.967	41.926	42.296
1	38.516	38.482	38.282	38.473	38.395	38.744
2	35.732	35.671	35.436	35.602	35.489	35.809
3	32.435	32.383	32.149	32.311	32.162	32.435
4	30.101	30.060	29.811	29.985	29.822	30.084
5	27.283	27.247	26.954	27.191	27.024	27.278
6	24.128	24.110	23.713	24.054	23.889	24.123
7	20.989	20.993	20.826	20.937	20.803	21.022
8	17.878	17.906	17.761	17.843	17.745	17.929
9	15.677	15.748	15.632	15.685	15.620	15.782
10	12.188	12.297	12.205	12.221	12.200	12.335
11	9.339	9.519	9.452	9.426	9.391	9.550
12	6.720	6.889	6.810	6.826	6.719	6.930

The positions of data reported in Tables 3.2 and 3.3 are not coincident. For steady water contents (dry, saturated, and partially saturated), the large core thermal properties are estimated by applying step boundary conditions to both ends simultaneously. The temperature response at locations along the core can be estimated using [Carslaw and Jaeger, 1959]:

$$v/V = 1 - 4/\pi \sum -1^n/(2n+1) \exp[-(2n+1)^2\pi^2 T/4] \cos[(2n+1)n\xi/2] \qquad (3.7)$$

where

$T = \kappa t/l^2$

$\xi = x/l$

and

- v observed temperature;
- V applied temperature at ends of core;
- κ assumed constant thermal diffusivity;
- x distance along core;
- l half-length of core.

3.3 Solute present

The large core was desaturated and then resaturated with a 0.05 M NaI solution. Gamma attenuation methods were employed to scan the core sample and evaluate the accuracy of the gamma attenuation method. Given the known attenuation coefficients for NaI, the interpreted concentration should be comparable to the known NaI concentration. Discrepancies between interpreted and prescribed concentrations are either attributable to: 1) errors in the dual-gamma detection process, 2) incomplete desaturation of the core and subsequent dilution of the 0.05 M NaI solution, 3) incomplete saturation of the core, or 4) evaporation of pure water from the end of the core leaving a higher-than-expected concentration of NaI accumulated at the evaporation face.

3.4 Discussion

Laboratory experiments conducted to observe thermal, liquid, vapor and solute transport through variably saturated, unfractured Apache Leap Tuff demonstrate that:

1. Conduction is the dominant heat transport mechanism even when a significant heat pipe is present.
2. Water contents increase away from the heat source due to vapor driven advection and condensation.
3. Solutes accumulate near the heat source, but the accumulation of solutes increases the osmotic potential which decreases the heat pipe phenomenon.
4. The heat pipe process may not significantly affect thermal or liquid flow in materials similar to the Apache Leap Tuff samples examined.
5. Solute transport was substantially affected by the heat pipe phenomenon, resulting in the accumulation of significant solutes nearer the heat source than would have occurred if the heat pipe had not been present.
6. Models of heat and liquid flow near high level waste repositories may not need to incorporate heat pipe effects.
7. Models of solute transport should incorporate the heat pipe phenomenon, and should also consider the effects of osmotic potential on liquid and vapor transport.

These observations may only be relevant to the conditions examined. Additional laboratory and computer simulation experiments should be conducted to evaluate the effects of coupled thermal, liquid, vapor and solute transport over a wider range of material properties. Also, the effects of thermomechanical, geochemical, biogeochemical, and radiation-induced changes will also require examination. It is possible that processes not yet considered may significantly affect the migration of radionuclides in the region immediately adjacent to the waste repository. Field and laboratory-scale experiments are necessary to identify these unknown processes.

4. FRACTURED BLOCK CHARACTERIZATION

Todd C. Rasmussen

Characterization methods are presented for a block of unsaturated, fractured rock. The methods provide data sets for use in evaluating parametric relationships, as well as for evaluating the adequacy of conceptual models related to fluid flow and transport through unsaturated fracture rock. The block of Apache Leap Tuff containing a single discrete fracture was excavated from a site near Superior, Arizona. The fracture was stabilized in the field using rock bolts cemented in place to prevent fracture movement. The block was then excavated using pneumatic hammers, transported to a rock quarry for shaping, and then moved to the laboratory for analysis. The block measures 20.2 x 92.5 x 21.0 cm and contains a single horizontal fracture measuring 20.2 x 92.5 cm.

Two metal manifolds were constructed and attached to short axes of the block to provide water injection capability into the rock fracture. The manifolds were attached with a thin rubber gasket between the manifolds and the rock matrix, allowing hydraulic communication only with the rock fracture. The exposed fracture surfaces along the long axes of the block were sealed using clay caulking. All surfaces of the block were then covered with sheets of transparent vinyl adhesive to prevent evaporation and seepage. Prior to encapsulation, the block was air-dried at an average humidity of approximately thirty percent.

4.1 Rock Volume and Porosity

The total rock porosity, consisting predominately of the rock matrix porosity, θ_m, plus the fracture porosity, θ_f, was obtained using a pycnometer. The pycnometer, with a volume of 3,634.2 cm^3, was attached to one of the injection manifolds with the manifold closed on the opposite end. The porous volume of the block was determined by placing a partial vacuum on the block, venting the pycnometer to the atmosphere, and then venting the pycnometer to the block. Figure 4.1 illustrates the experimental apparatus. The initial pressures of the block and pycnometer, and the final pressure of the two vented to each other are used to calculate the block volume assuming isothermal ideal gas behavior:

$$V_t = - V_p \, \Delta p_p / \Delta p_b \tag{4.1}$$

where

V_t	total block void volume
V_p	pycnometer volume
Δp_b	pressure change in rock
Δp_p	pressure change in pycnometer

Pycnometer measurements yielded a total rock void volume of V_t = 4,635 $\pm$ 120 cm^3 (mean $\pm$ standard deviation of mean). The block porosity is calculated by subtracting the fracture volume (determined below) and then dividing the block void volume by the dimensions of the block. Given the matrix block dimension of approximately 39,240 cm^3, the block effective porosity is θ_m = 11.5 $\pm$ 0.3 percent.

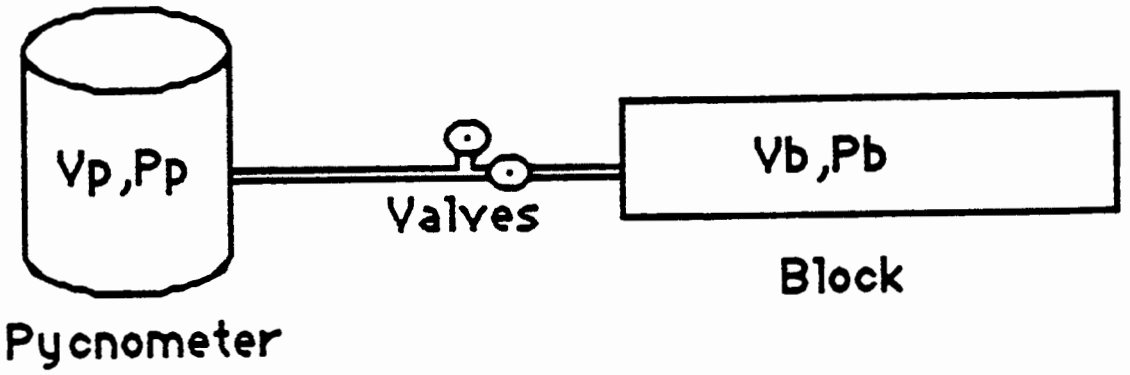

Figure 4.1: Pycnometer apparatus for porosity determination

4.2 Hydraulic Diffusivity Coefficient

The rock matrix water diffusivity, D_m, was estimated using a rock matrix core obtained from an excess rock fragment located immediately next to the block. The diffusivity was determined by placing the air-dried rock core on a water surface and measuring the advancement of the wetting front with time along four vertical profiles. Figure 4.2 presents the experimental configuration. The core imbibition experiment was conducted under conditions similar to that expected to occur during the block imbibition experiment, i.e., the core was at the same initial water content and water was applied at near zero pressure. The rock matrix water diffusivity was calculated assuming negligible gravitational forces using:

$$D_m = \pi y^2 / 4 t \qquad (4.2)$$

where

D_m	rock matrix water diffusivity coefficient
y	height of rise of visual wetting front
t	observation time

A mean water diffusivity for the four transects of $D_m = 3.61 \pm 0.28$ cm^2 hr^{-1} was observed. Figure 4.3 presents the laboratory rock matrix imbibition data along with least squares model fits of the data. It is evident from the figure that significant diffusivity variation is present, even in the same core, leading to uncertainty in this parameter.

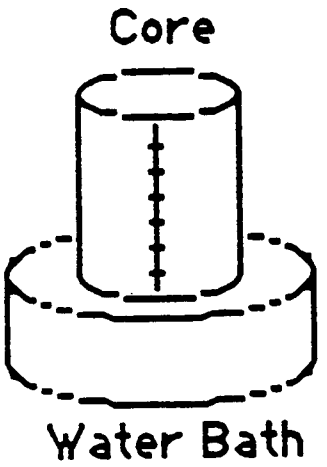

Figure 4.2: Experimental setup for rock matrix water diffusivity determination

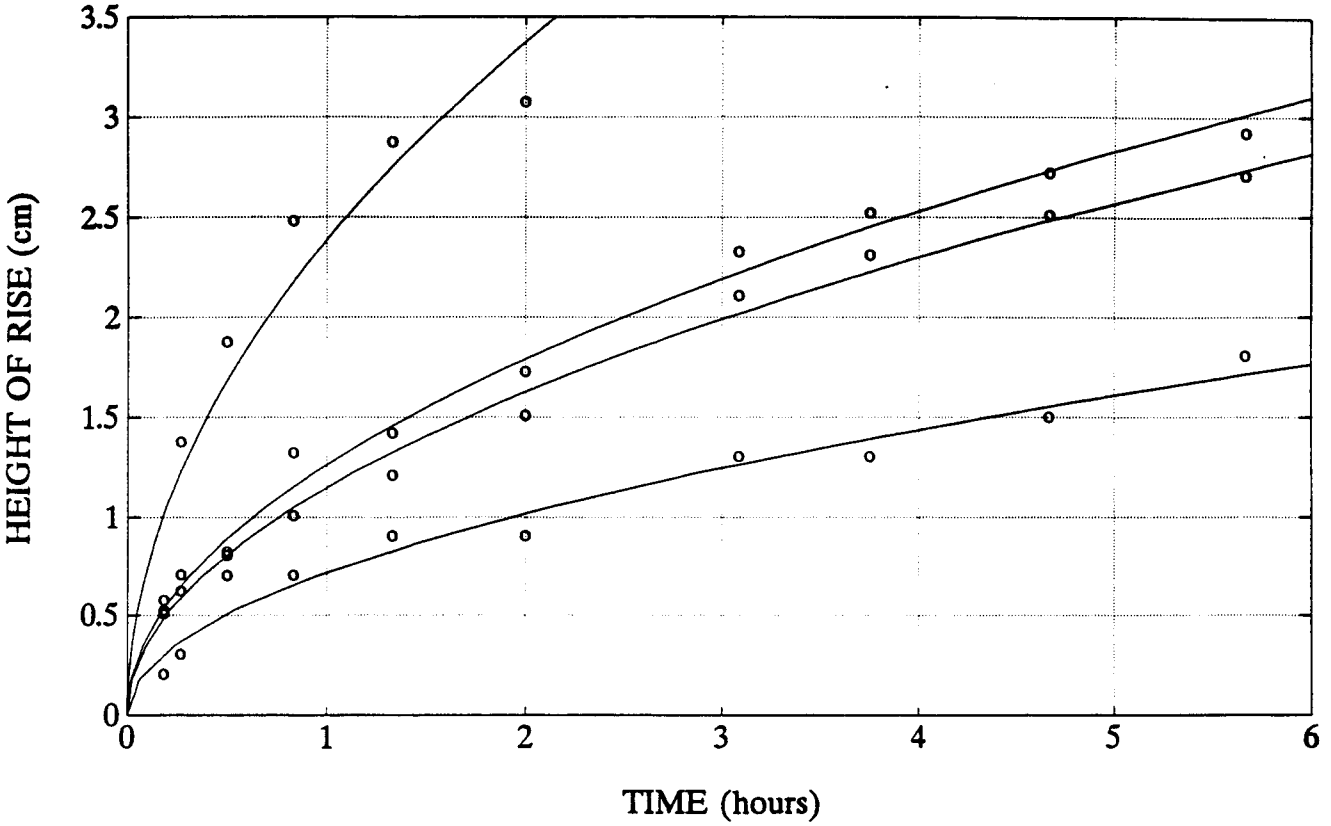

Figure 4.3: Height of water rise in rock matrix; observed (symbols) and calibrated (lines)

4.3 Fracture Volume

Three methods were employed to determine the fracture volume, V_f. In one case, pycnometer tests of fracture volume were obtained once the rock matrix was saturated with water. Because the rock matrix pores were saturated with water, the fracture porosity could be determined without the complicating factors of matrix diffusion and storage. Results of pycnometer tests using a pycnometer volume of 108.4 cm^3 indicated a fracture volume of $V_f = 142.3 \pm 4.0$ cm^3.

In a second experiment, argon and helium gasses were used as air-phase tracers to determine the fracture volume. A steady flow of gas was established and then connected to one end of the rock fracture. A gas leak detector was used to measure the arrival time and breakthrough curve of the gas tracer. The flow rate of gas through the fracture was measured using a bubble flowmeter. The pressure gradient was also recorded. The fracture volume was determined by multiplying the gas flow rate by the arrival time of the gas. For dry rock, the initial arrival time was used to calculate the fracture volume because the diffusion of gas into the rock matrix substantially diminishes subsequent concentrations. The fracture volume calculated using the volumetric flux and the observed travel time was $V_f = 100.2 \pm 13.2$ cm^3.

A final experiment was conducted using tracer tests through an open fracture embedded in a saturated rock matrix. The average travel time was used to determine the fracture volume. For the helium and argon gas tracer tests past a saturated rock matrix, the fracture volume was estimated to be $V_f = 143.0 \pm 12.6$ cm^3 which is very similar the estimate presented above for the volume estimated using the pycnometer. Estimates of fracture volume using tracer tests through the dry rock are less than the estimate based on the wet rock tracer and pycnometer tests due in part to the use of the initial arrival time.

4.4 Fracture Transmissivity

The rock fracture transmissivity, $T = b\ K_f$, was determined before and after the imbibition test using air flow, tracer and water injection experiments. For these experiments, a steady fluid flow was established, the flow rate was measured using a bubble flowmeter for gas and a graduated cylinder for liquid, and the pressure head gradient was measured. Figure 4.4 presents the experimental conditions. The fracture transmissivity was calculated using:

$$T = (Q/w) / (\Delta h/L) = q / i \qquad (4.3)$$

where

T	fracture transmissivity
Q	volumetric flow rate
w	fracture width
Δh	freshwater manometer pressure head drop
L	fracture length
q	flow rate per unit fracture width, Q/w
i	freshwater pressure head gradient, $\Delta h/L$

The freshwater manometer pressure head change drop is used to provide consistent estimates of fracture transmissivity, irregardless of the fluid viscosity. To adjust for variable viscosity, the observed head is multiplied by the water viscosity and divided by the test fluid viscosity (i.e., $\Delta h = \Delta h_o\ \mu_w/\mu_g$). This formulation allows disparate fluids to be compared for range of pressure head gradients.

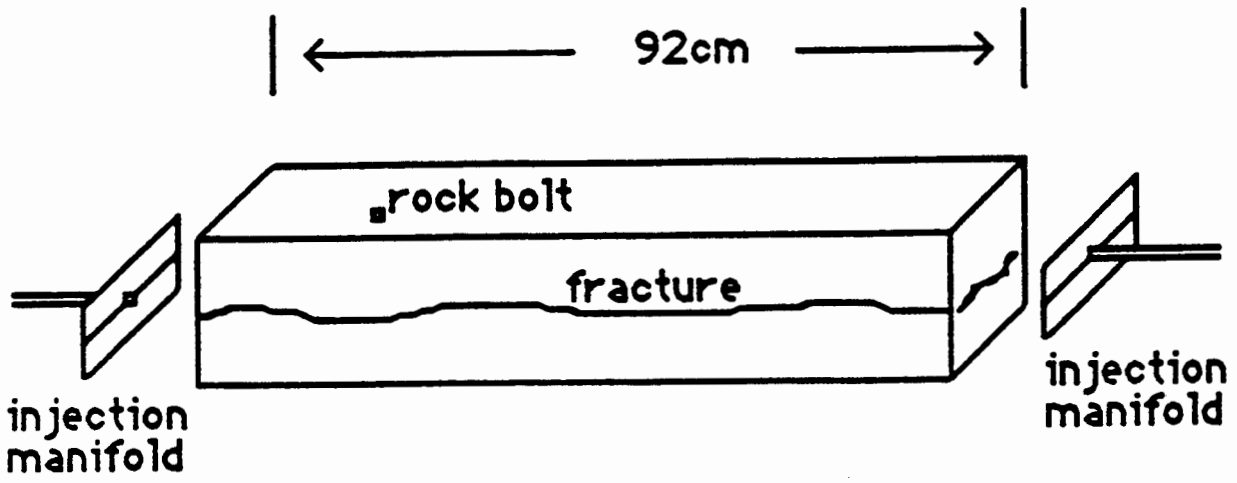

Figure 4.4: Experimental setup for fracture permeability determination

The fracture transmissivity calculated using water as the test fluid is T = 410 cm^2 hr^{-1}. The mean fracture transmissivity calculated using data for air flow through dry rock is higher at T = 457 cm^2 hr^{-1}, while the value for wet rock is slightly lower at T = 266 m^2 s^{-1}. Using argon gas flow through dry rock yields a value of T = 389 cm^2 hr^{-1}, which is close to the estimated value using water. The value using mixtures of air with helium and argon gasses through the wet rock was larger, T = 598 cm^2 hr^{-1}. Using all data results in a mean fracture transmissivity of T = 490 $\pm$ 25.2 cm^2 hr^{-1}. Figure 4.5 presents the fracture transmissivity data as a function of the pressure gradient for air, mixtures of air with argon and helium gasses, and water. The effects of slip-flow are not apparent, which is consistent with fluid flow through the large apertures (i.e., $>>$ 1 μm) present in the fracture.

4.5 Fracture Hydraulic Conductivity

An effective fracture hydraulic conductivity, K_f, was obtained using data from the helium and argon tracer tests through the fracture embedded in a saturated rock matrix. The velocity of the tracer was calculated as the straight-line travel path divided by the observed arrival time. The mean velocity was obtained by averaging over all measured arrival times. The effective hydraulic conductivity was determined by dividing the mean velocity for each test by the mean freshwater gradient, adjusted for each test using the viscosity of the fluid. The observed effective fracture hydraulic conductivity was observed to be K_f = 9650 $\pm$ 504 cm hr^{-1}.

4.6 Fracture Air-Entry Value

The air-entry value, h_a, for the fracture is the suction head at which the fracture saturation allows the passage of air from one manifold to the other. The air-entry value was obtained by placing a vacuum on the fracture, flooding the fracture with water, dissipating the vacuum and allowing the water to saturate the fracture, disconnecting the water source, venting one manifold to the atmosphere, lowering the outlet of an outflow tube connected to the opposite fracture manifold, and observing the suction head at which air was observed in the outflow tube. An air-entry suction head of h_a = 13.5 $\pm$ 0.7 cm was required to drain the fracture at 20°C.

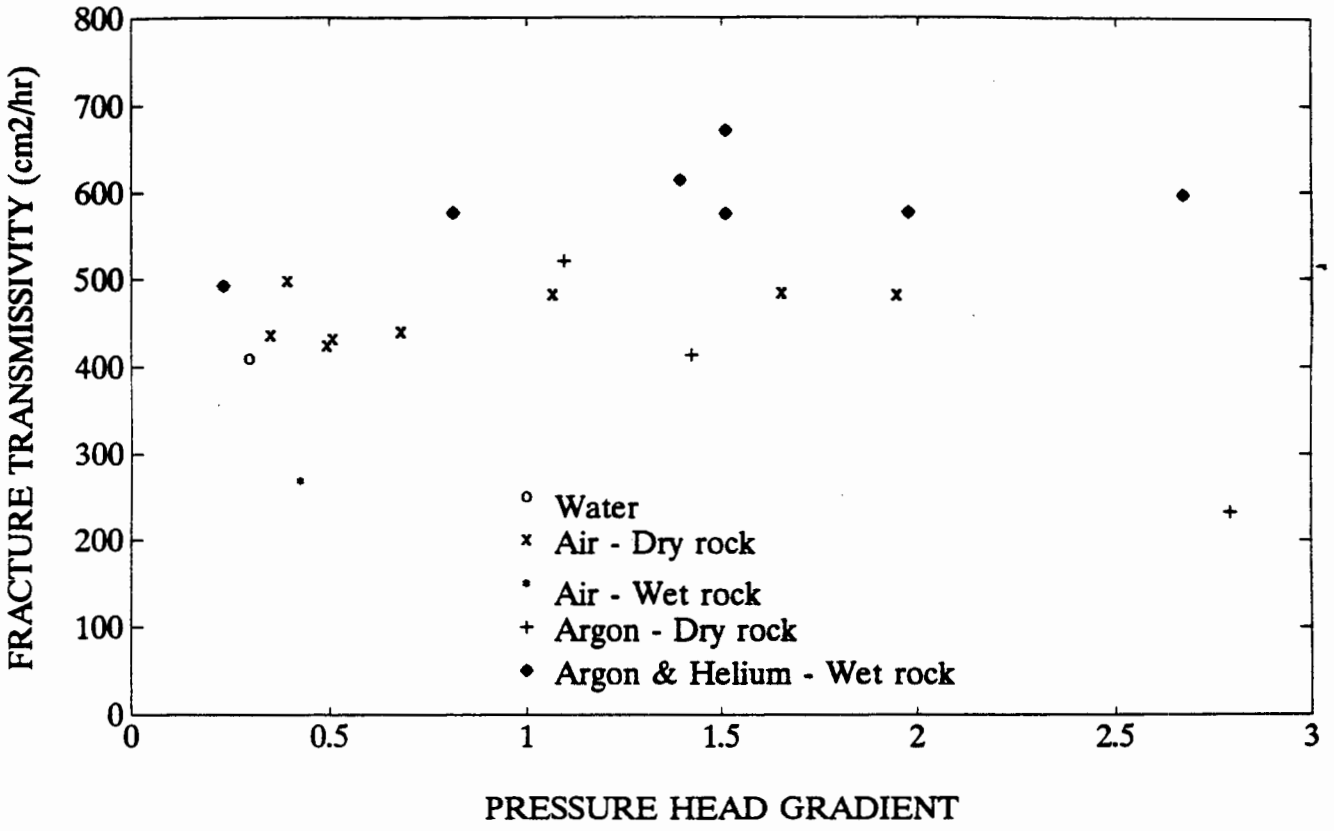

Figure 4.5: Fracture transmissivities determined from gas and water permeability tests

4.7 Breakthrough Curves

Argon gas movement through the rock matrix due to advective transport of the gas through the fracture was observed by maintaining a constant pressure gradient between the two manifolds and measuring the outflow concentration of gas using a thermal conductivity detector. Figure 4.6 presents the laboratory experimental arrangement. Gas diffusion into the dry rock matrix resulting from the advection of gas through the fracture and Fickian diffusion into the matrix on either side of the fracture is predicted using:

$$C^* = (C-C_i)/(C_o-C_i) = \text{erfc}[\theta_g D_g^{1/2} \tau / b (t-\tau)^{1/2}] \qquad \text{for } t > \tau \qquad (4.4)$$

where

C^*	normalized tracer concentration
C	measured tracer concentration
C_i	initial tracer concentration in rock
C_o	injected tracer concentration
θ_g	accessible gas-filled matrix porosity
D_g	matrix gas diffusion coefficient
b	fracture half-aperture
t	time since injection
τ	time of travel along length of block

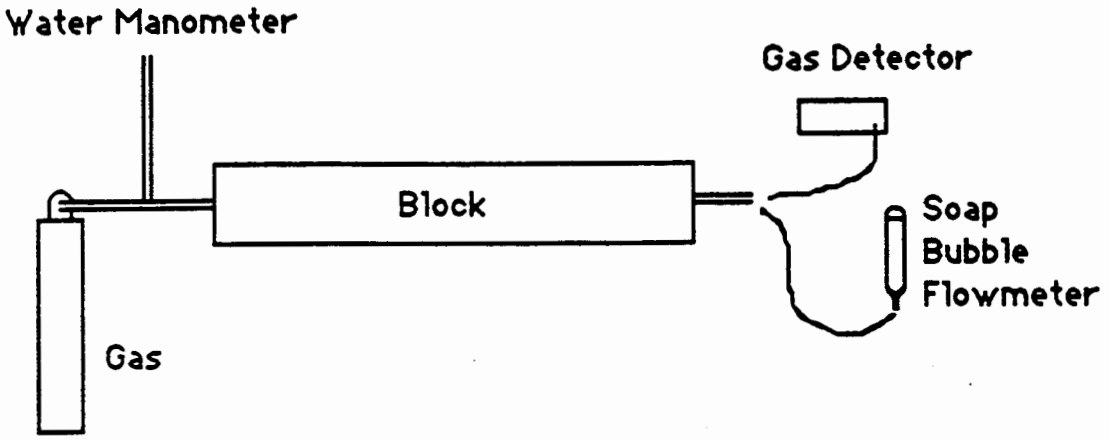

Figure 4.6: Experimental setup for observing gas tracer breakthrough curves.

Equation (4.4) was inverted to determine the matrix gas diffusion coefficient:

$$D_g = (t-\tau)\ (b\ \text{ierfc}[C^*] / \tau\ n)^2 \qquad \text{for } t > \tau \qquad (4.5)$$

where ierfc is the inverse complementary error function. For pure argon gas flowing past the dry rock matrix, the matrix argon gas diffusion coefficient was estimated as $D_g = 31.0 \pm 0.94$ cm^2 hr^{-1}. Figure 4.7 presents plots of observed breakthrough curves along with the estimated breakthrough using the calculated matrix gas diffusion coefficient value.

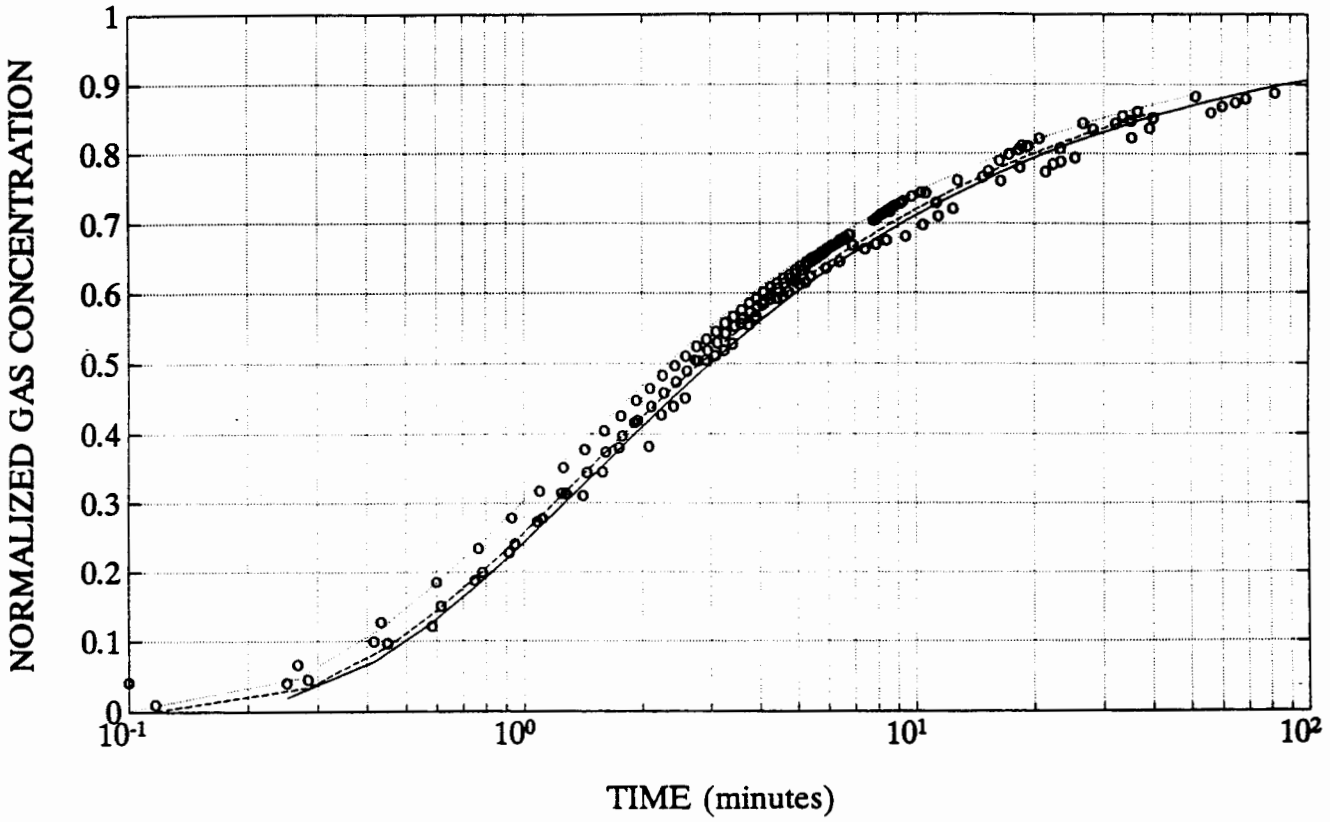

Figure 4.7: Argon gas breakthrough curves; observed (circles) and fitted (lines).

For a single component advection-diffusion model the matrix gas diffusion coefficient combines the effects of flow due to partial and total gas pressure head gradients [adapted from Massmann and Farrier, 1992, Eqn 11]:

$$D_g = D_j + k/\mu\ p_j\ \nabla h/\nabla h_j \tag{4.6}$$

where

D_j	effective diffusion coefficient for gas j
k	rock matrix permeability
μ	gas mixture viscosity
p_j	mean gas pressure head
∇h	total pressure head gradient
∇h_j	partial pressure head gradient

Massmann and Farrier further show the validity of the single-component model for conditions where the permeability of the rock matrix is greater than approximately 0.01 μm^2. The mean rock matrix permeability of the Apache Leap Tuff is approximately 0.002 μm^2, or near the limit of the applicability of the single-component model. For conditions where the single-component model is not appropriate, Massmann and Farrier present a simultaneous equation method for solving multi-component gas mixture flow and diffusion problems.

Advantage can be taken of variations in the gas diffusion coefficient to determine the gas porosity of fractured rock or geologic materials with both micro- and macro-porosities. The volume of air-filled microporosity determines the reduction in breakthrough time for a gas with low diffusion rates compared to the time of a gas with higher diffusion rate. Breakthrough curves for gasses of variable diffusivity are denoted by (C_i,t_i) where C_i is the observed concentration at time t_i for gas i with diffusion coefficient D_i. Gasses with variable diffusion coefficients are used to determine the travel time through the fracture, τ, by noting that for conditions of steady flow, homogenous rock matrix porosity and variable travel path lengths between the injection source and the observation, there will exist n pairs of observations where the gas concentrations for two gasses are equal, i.e., $C_1 = C_2$. The fracture travel time for the specified concentration is:

$$\tau_i = (t_1 - \alpha\ t_2) / (1 - \alpha) \tag{4.7}$$

where α is the diffusivity ratio, D_1/D_2. Inserting the estimated value of τ_i into Equation (4.7) yields an estimate of the rock matrix porosity-fracture aperture ratio for each travel path:

$$(n/b)_i = \text{ierfc}(C_1)\ (t_1-\tau_i)^{1/2} / \tau_i\ D_1^{1/2} \tag{4.8}$$

For a specified travel distance, L, with a steady and uniform velocity along the streamline:

$$(b/L)_i = (12\ \mu / \gamma\ \Delta h\ \tau_i)^{1/2} \tag{4.9}$$

where

μ	gas viscosity
γ	manometer fluid specific weight
Δh	pressure head difference along the streamline from source to observation point

The hydraulic conductivity distribution for each streamline can also be determined using:

$$K_i = L^2 / \Delta h \, \tau_i \qquad (4.10)$$

For one-dimensional steady fracture flow, the values of μ, γ, L and Δh are constant and known, providing unique estimates of the distribution of fracture hydraulic conductivity, fracture apertures and rock matrix porosity.

4.8 Fracture Aperture Determination

Six methods for determining the fracture aperture are presented. Three of the methods provide estimates of the volume of the fracture, two methods arrive at an equivalent frictional aperture using Poiseuille's law, and one method uses capillary theory to estimate an equivalent aperture. Volumetric apertures are denoted with the symbol b, frictional apertures with the symbol e, and capillary aperture with the symbol c.

Pycnometer estimates of fracture volume were used to estimate the mean fracture aperture:

$$b_1 = V / A \qquad (4.11)$$

where

V	fracture volume
A	fracture surface area
b_1	volumetric aperture

Poiseuille's law is commonly employed to relate the fracture permeability to the fracture aperture for the case of fluid flow through smooth-walled fractures.

$$T = b_2 K = b_2 k \gamma/\mu = b_2 e_1^2/12 \, \gamma/\mu \qquad (4.12)$$

where

T	fracture transmissivity
b_2	volumetric aperture
k	intrinsic permeability
γ	specific weight of manometer fluid
e_1	Poiseuille aperture

Equation (4.12) applied to rough-walled fractures underestimates the mean aperture due to inertial and friction effects. The assumption is often made that $b_2 = e_1$, i.e., that the mean cross-sectional area equals the Poiseuille aperture, yielding the so-called cubic equation:

$$k_f = e_2^3/12 \qquad (4.13)$$

where

k_f	fracture intrinsic permeability
e_2	Poiseuille aperture estimated using the cubic equation

Tracer studies provide additional estimates of fracture aperture. A direct estimate used the arrival time of a conservative tracer in conjunction with the flow rate and the assumption of piston flow:

$$b_3 = V/A = Q \, t_a / A \qquad (4.14)$$

where

b_3	volumetric aperture from tracer arrival times
Q	volumetric flow rate
t_a	tracer residence time

The tracer velocity was also used to estimate the fracture permeability:

$$k = v \gamma / \mu i = L \gamma / \mu i t_a \tag{4.15}$$

where

v	tracer velocity
i	pressure head gradient
L	fracture length

The tracer velocity estimate of fracture permeability is used to estimate two additional fracture apertures, the Poiseuille aperture from Equation (4.12), and the mean aperture using Equation (4.13) and knowing the fracture transmissivity:

$$b_2 = T / K = e_2^3 / e_1^2 \tag{4.16}$$

The negative pressure head required to drain the fracture is the air-entry value and can be related to a fracture aperture using:

$$c = 2 \tau \cos ß / \gamma \Delta z \tag{4.17}$$

where

c	capillary aperture
τ	air-water surface tension
ß	air-water-solid contact angle
γ	water specific weight
Δz	air-entry pressure head

For this experiment, the specific weight of water was 9806 pa m^{-1} and the surface tension was 0.07275 Pa m. A contact angle of 0° was assumed. Table 4.1 summarizes the experimental estimates of the Poiseuille, volumetric and capillary aperture estimates.

TABLE 4.1
Fractured block aperture estimates.

		mean ± std. dev.
Poiseuille's Aperture:		
e_1	$(12\ \mu\ K\ /\ \gamma)^{1/2}$	181 ± 41 μm
e_2	$(12\ \mu\ T\ /\ \gamma)^{1/3}$	255 ± 95 μm
Volumetric Aperture:		
b_1	V/A	762 ± 21 μm
b_2	T/K	507 ± 403 μm
b_3	$Q\ t_a\ /\ A$	765 ± 67 μm
Capillary Aperture:		
c	$2\tau \cos ß\ /\gamma\ \Delta z$	112 ± 21 μm

Figure 4.8 presents a comparison of the six fracture aperture estimates. The volumetric apertures obtained from the pycnometer and tracer experiments, b_1 and b_3, appear similar, while the volumetric aperture obtained from permeability and tracer velocities, b_2, is significantly smaller. The apertures estimated using the permeability equations are smaller yet, due undoubtedly to surface effects. The smallest observed aperture is the capillary aperture, c. The order of fracture apertures are:

$$c < e_1 < e_2 < b_2 < b_1 \leq b_3$$

This ranking of fracture apertures is consistent with the model of Tsang [1992]. Silliman [1989] notes that the fracture aperture obtained from permeability estimates can be function of the geometric mean, while the volumetric mean is the arithmetic mean of the fracture aperture. For an unknown spatial distribution of fracture apertures, x, the geometric mean, exp(E[ln(x)]), can be related to the arithmetic mean, E[x], using:

$$E[e] = \exp(E[\ln(x)]) = \exp(E[\ln(E[x]) + \ln(1+a)]) \tag{4.18}$$

where $a = x/E(x) - 1$. Knowing that:

$$\ln(1+a) = a - a^2/2 + a^3/3 - \ldots \qquad \text{for } -1 < a < 1 \tag{4.19}$$

yields the following relationship between the mean volumetric aperture b, and the mean permeability aperture, e:

$$\sigma_x^2 \approx 2\ b^2\ \ln(E[b]/E[e]) \tag{4.20}$$

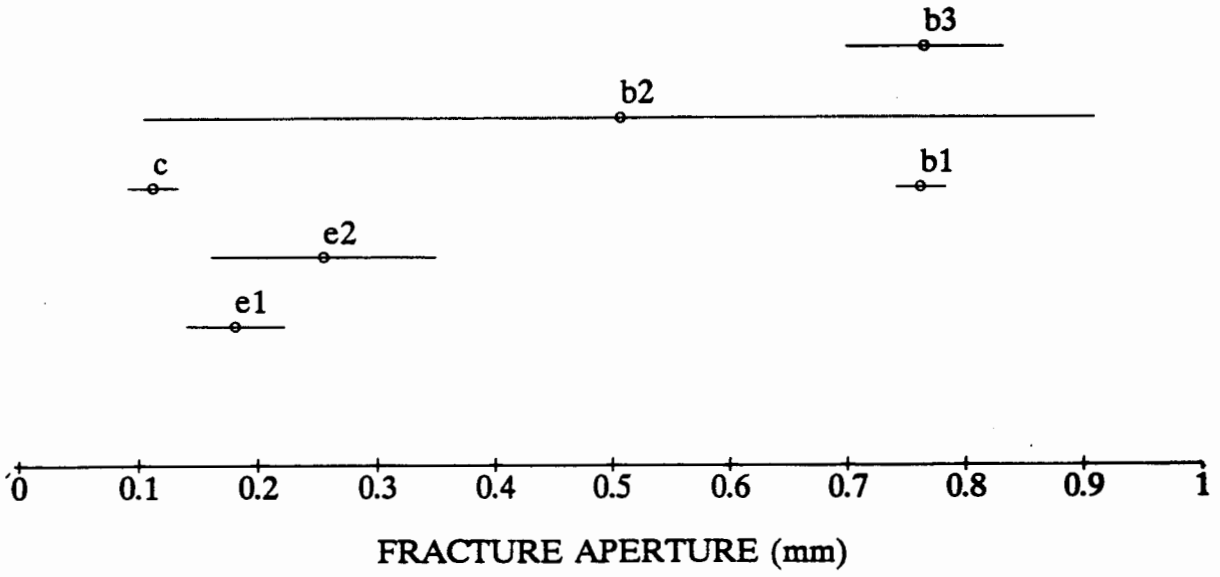

Figure 4.8: Fracture apertures; mean (circles) and one standard deviation (lines)

Using the values of b_1 and e_1 from Table 4.1 yields an estimate of the fracture aperture standard deviation of 1.3 mm, which is consistent with the fracture surface roughness standard deviation of 1.8 $\pm$ 0.8 mm obtained from profiling six fracture surfaces (three mated pairs) located immediately adjacent to the rock matrix block investigated here [Vickers, 1990]. Inserting a value of b_1 and e_2 from Table 4.1 yields a slightly smaller fracture aperture standard deviation of 1.1 mm. While the fracture aperture standard deviation is expected to decrease for mated fracture surfaces, a reduction in the fracture surface roughness standard deviation would reduce the gap between the calculated and observed standard deviations.

4.9 Discussion

Table 4.2 presents estimated characterization properties of the rock matrix and the embedded fracture. Several parameters, including the fracture porosity, liquid saturation changes across the wetting front in the fracture and rock matrix are assumed values. Table 4.2 also presents characterization parameters with their uncertainties. Uncertainties in the derived parameters were estimated by propagating parameter uncertainties using first-order Taylor series approximations, presented as Table 4.3. A first-order approximation of parameter uncertainty propagation was estimated using the Taylor-series expansion of the input errors.

Characterization techniques which demonstrate promise for estimating material properties on field scales include the use of a pycnometer to measure fracture and matrix porosities, and gas-phase tracer experiments to estimate the fracture/matrix porosity ratio, the permeability distribution, and the porosity-length distribution. While these indices are only strictly appropriate for gas-phase transport, inferences to liquid phase transport may be derived if relationships between gas and liquid phase

transport are known. It is anticipated that gas-phase testing using tracers will become a rapid and effective tool for characterizing macropores on field scales. The interactions between matric storage and advection through fractures have been demonstrated in the laboratory, and field scale experiments are being explored to apply this new technique.

Interpretation of fracture aperture estimates is complicated by the observation that the estimated value is a function of the method employed to provide the estimate. Six measures of fracture aperture were developed and comparisons were made between methods. It was observed that volumetric measures of fracture aperture yield the highest values, with lower estimates provided by measures using Poiseuille's law. The lowest estimate was obtained using capillary theory. It can be concluded that when fracture aperture measurements are reported, the method employed to provide the estimate should also be indicated.

Uncertainty measures of characterization parameters are also presented here. The uncertainty in the measured parameter are required to evaluate the uncertainty in predictions based upon the parameter. Forecasts of flow and transport will require measures of uncertainty in the forecast. Uncertainties in estimated parameters may contribute to a large errors in forecasts.

TABLE 4.2
Fractured block characterization parameters.

		mean ± std. dev.	
Rock Matrix Properties:			
V	rock volume	39,240 ± 0	cm^3
V_t	pore plus fracture volume	4,635 ± 120	cm^3
V_m	matrix pore volume	4,493 ± 127	cm^3
θ_m	porosity	0.115 ± 0.003	
ΔS_m	liquid saturation change	1 ± 0	(1)
D_m	water diffusivity coefficient	3.61 ± 0.28	$cm^2\ hr^{-1}$
D_g	argon gas diffusion coefficient	31.0 ± 0.94	$cm^2\ hr^{-1}$
Rock Fracture Properties:			
V_f	volume	142.3 ± 41.7	cm^3
w	width	20.2 ± 0	cm
a	fracture-boundary distance	10.5 ± 3	cm
b	half-aperture	381 ± 11	μm
L	length	92.5 ± 0	cm
θ_f	porosity	1 ± 0	(1)
ΔS_f	liquid saturation change	1 ± 0	(1)
K_f	hydraulic conductivity	9650 ± 504	$cm\ hr^{-1}$
T_f	transmissivity	490 ± 25.2	$cm^2\ hr^{-1}$
D_f	water diffusivity coefficient		

(1) Assumed value.

TABLE 4.3
First-order uncertainty propagation using Taylor-series approximations.

Untransformed:	$\mu_x = E(x)$ $\sigma_x = (E(x - E(x))^2)^{1/2}$ $CV_x = \sigma_x / \mu_x$
Reciprocal transform:	$\mu_{1/x} \approx (1 + CV_x^2) / \mu_x$ $\sigma_{1/x} \approx (CV_x^2 - CV_x^4)^{1/2} / \mu_x$ $CV_{1/x} \approx CV_x (1 - CV_x^2)^{1/2} / (1 + CV_x^2)$
Product transform:	$\mu_{x \cdot y} = \mu_x \mu_y$ $\sigma_{x \cdot y} = (\mu_y^2 \sigma_x^2 + \mu_x^2 \sigma_y^2 + \sigma_x^2 \sigma_y^2)^{1/2}$ $CV_{x \cdot y} = (CV_x^2 + CV_y^2 + CV_x^2 CV_y^2)^{1/2}$
Ratio transform:	$\mu_{x/y} \approx (1 + CV_y^2) \mu_x / \mu_y$ $\sigma_{x/y} \approx (CV_x^2 + CV_y^2 - CV_y^4)^{1/2} \mu_x / \mu_y$ $CV_{x/y} \approx (CV_x^2 + CV_y^2 - CV_y^4)^{1/2} / (1 + CV_y^2)$
Logarithm transform:	$\mu_{\ln(x)} \approx \ln(\mu_x) - CV_x^2/2$ $\sigma_{\ln(x)} \approx ((\ln(\mu_x))^2 + \mu_x CV_x^2)^{1/2}$ $CV_{\ln(x)} \approx ((\ln(\mu_x))^2 + \mu_x CV_x^2)^{1/2} / (\ln(\mu_x) - CV_x^2/2)$
Exponential transform:	$\mu_{\exp(x)} \approx 1 + \mu_x + \sigma_x^2/2$ $\sigma_{\exp(x)} \approx (1 + 2\mu_x + 2\sigma_x^2)^{1/2}$ $CV_{\exp(x)} \approx (1 + 2\mu_x + 2\sigma_x^2)^{1/2} / (1 + \mu_x + \sigma_x^2/2)$

Notes: 1. x and y are assumed to be uncorrelated random variables.
2. Moments greater than second order are neglected.
3. CV = Coefficient of Variation < 1.

5. WATER IMBIBITION EXPERIMENT

Todd C. Rasmussen

The suitability of conceptual and numerical models of flow through unsaturated fractured rock was evaluated by conducting an imbibition experiment into an initially unsaturated fractured tuff block. Two methods were used to evaluate a model developed by Nitao and Buscheck [1991] for its ability to reproduce imbibition rates and wetting front position. The first method compared calibration parameters obtained from fitting prediction equations to the imbibition and fracture wetting front advance data. The second method compared observed imbibition rates and visual wetting front position in the fracture to the predicted values based upon characterization experiments presented in the previous section. Parameters and predictions should compare favorably if the model accurately represents the physical system, and the characterization experiments accurately estimate the parameters of interest. The experiment also had the secondary intent of evaluating methods that may be relevant for field characterization techniques.

5.1 Experimental Setup

The block of fractured Apache Leap Tuff described in the previous section was used to conduct an imbibition experiment. The block was encased in a clear vinyl cover and attached to intake manifolds at either end of the horizontal fracture. The fracture was also caulked along the long length of the block prior to encapsulation with the vinyl to prevent fluid flow between the rock matrix and the vinyl. The water imbibition experiment was initiated by opening a valve connected to the fracture intake manifold. A graduated Marriotte bottle maintained a pressure head of 1 cm of water within the manifold. The Marriotte bottle was also used to measure the water imbibition volume. Table 5.1 reports the observed cumulative imbibition volumes. The fracture manifold at the opposite end of the block was open to the atmosphere. Figure 5.1 illustrates the experimental configuration.

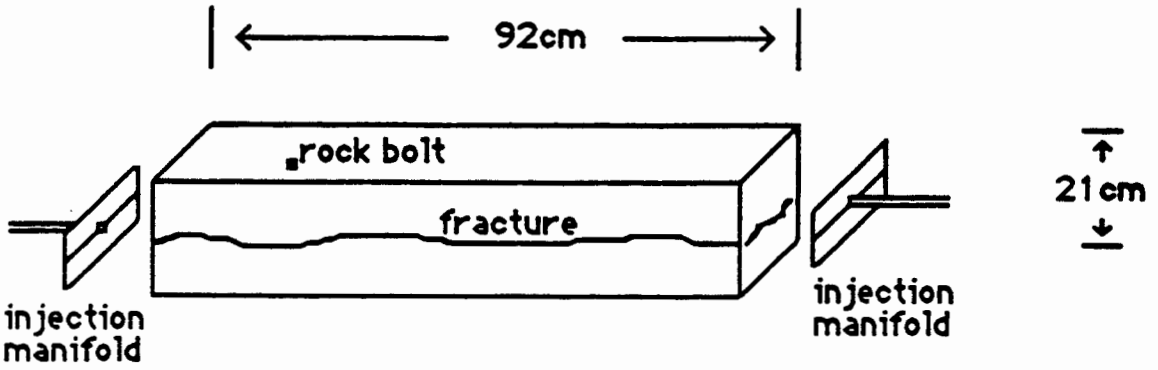

Figure 5.1: Fractured tuff imbibition experimental setup.

Table 5.1
Fracture block imbibition volumes.

Time (min)	Volume (cm^3)	Time (min)	Volume (cm^3)	Time (min)	Volume (cm^3)
2	15	155	212	2797	1678
3	20	165	235	2887	1711
4	25	180	250	4556	2271
5	28	195	270	4597	2313
7	31	210	280	4704	2313
9	35	225	293	4708	2323
11	39	240	312	4758	2333
13	41	255	328	4794	2342
15	46	285	342	5966	2896
19	52	300	360	5986	2911
22	57	340	407	6017	2911
25	60	360	430	6026	2924
30	70	390	463	7303	3588
35	73	420	485	7450	3649
40	80	452	500	7507	3671
45	90	465	506	7573	3696
50	93	508	528	7633	3720
55	99	552	577	8546	4041
60	107	586	598	8883	4122
65	116	596	601	9058	4157
70	126	600	607	10108	4337
75	132	771	711	10587	4390
80	140	1344	1034	11677	4511
85	144	1440	1126	12035	4551
90	150	1519	1168	12882	4679
95	157	1676	1301	13248	4717
100	163	1801	1309		
105	169	1825	1317		
120	190	1892	1348		
135	202	1899	1348		

The visual wetting front position was traced onto the clear vinyl covering the rock surface. Figure 5.2 presents the observed wetting front position in the rock matrix. The wetting front in the fracture advanced rapidly and irregularly for the first ten hours. Isolated zones of saturation were observed along the length of the fracture that coalesced at about ten hours, after which time the advancement of the wetting front along the fracture slowed, and most of the water movement appeared to be in the matrix perpendicular to the fracture with some exceptions. At about 46 hours, rapidly growing fingers of saturation in the rock matrix intersected both the top and bottom boundaries. These fingers expanded laterally in size until about 146 hours, when most of the block was saturated, and the fracture wetting front appeared to intersect the far end of the block. Full saturation was not observed until approximately 221 hours.

The visual wetting front location in the fracture was estimated by noting the time and location of the furthest advance of the wetting front in the rock matrix immediately adjacent to the fracture. Four estimates of this location were obtained; on the front and back surfaces, and on the upper and lower fracture surfaces. While the position was expected to be the same for the upper and lower surfaces of a fracture, this was not commonly observed.

Nitao and Buscheck [1991] present analytic solutions for water imbibition into regularly-spaced, initially-dry, arbitrarily-oriented fractures bounded by unsaturated porous rock. The equations for horizontal fracture flow can be rewritten as:

$$q \approx \begin{cases} \alpha_1 t^{-1/2} & t < t_1 \\ \alpha_2 t^{-1/4} & t_1 < t < t_2 \\ \alpha_3 t^{-1/2} & t_2 < t \end{cases} \qquad (5.1)$$

where

$$t_1 = [b\ \Delta S_f / \theta_m\ \Delta S_m]^2\ \pi / D_m \qquad (5.2a)$$

$$t_2 = a^2\ \pi / D_m \qquad (5.2b)$$

$$\alpha_1 = \Gamma(5/4) / \Gamma(3/4)\ \theta_f\ \Delta S_f\ (D_f / \pi)^{1/2} / 2 \qquad (5.2c)$$

$$\alpha_2 = \alpha_1\ 8^{1/2}\ t_1^{-1/4} \qquad (5.2d)$$

$$\alpha_3 = \alpha_1\ (V_f / V_t)^{1/2} \qquad (5.2e)$$

$$D_f = 2\ \pi\ K_f\ p_o / \theta_f\ \Delta S_f \qquad (5.2f)$$

q	fracture imbibition rate per unit fracture length
θ_f	fracture porosity
θ_m	matrix porosity
ΔS_f	change in fracture saturation across the wetting front
ΔS_m	change in matrix saturation across wetting front
D_f	fracture diffusivity coefficient
D_m	matrix diffusivity coefficient
a	half-distance between parallel fractures
b	fracture half-aperture
t	time from beginning of imbibition
V_f	fracture pore volume
V_t	total matrix plus fracture pore volume
K_f	fracture hydraulic conductivity
p_o	boundary pressure head

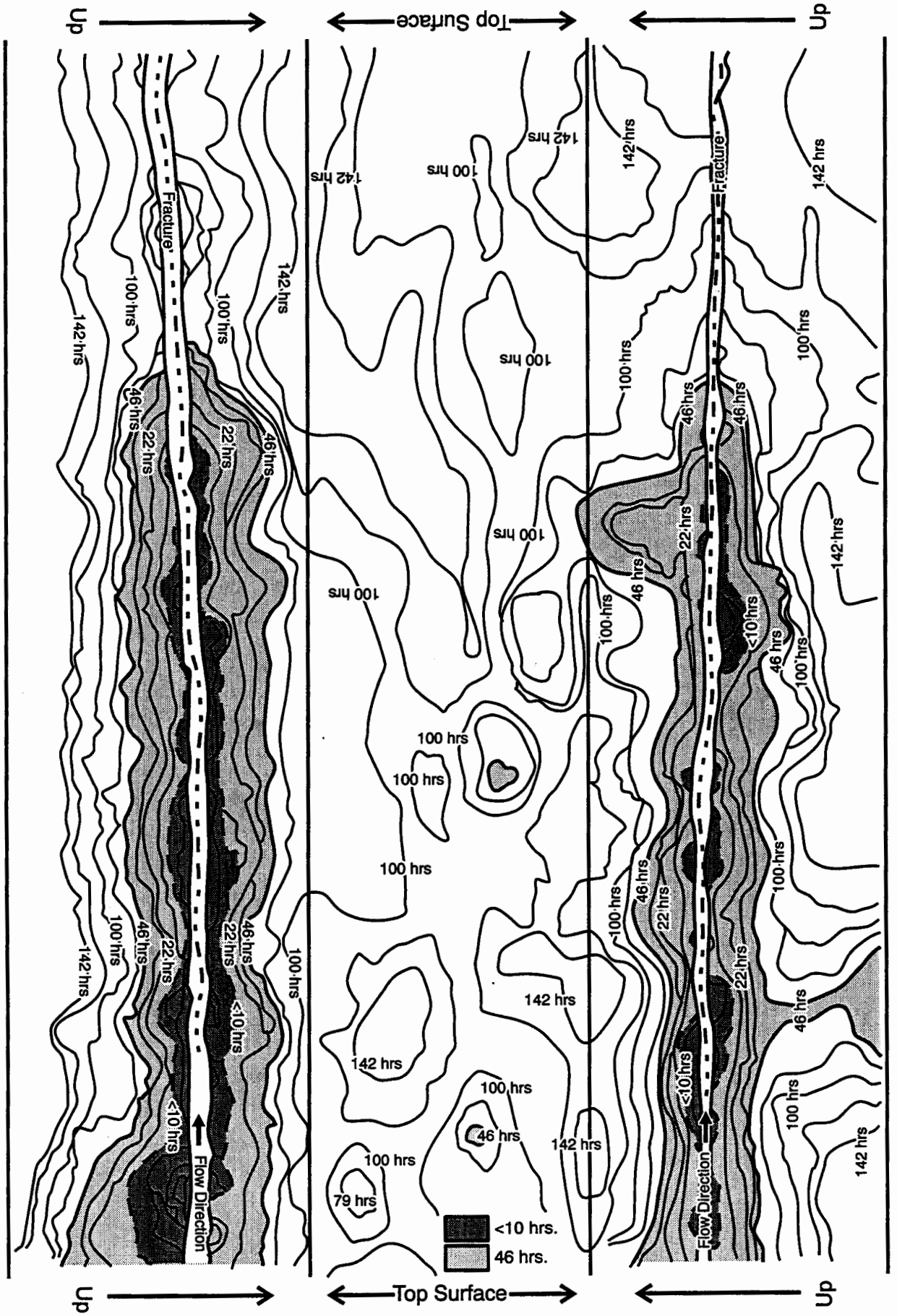

Figure 5.2: Observed rock matrix wetting front positions.

Note that the Nitao and Buscheck model accounts for three flow phases; an initial stage dominated by imbibition into the fracture governed by linear square-root-time decrease in flow rate, a second phase dominated by imbibition into the fracture and the rock matrix governed by a fourth-root-time decrease in flow, and a final phase resulting from interference between regularly spaced fractures governed by a return to the square-root-time decrease.

The Nitao and Buscheck model also predicts the wetting front position, x_w, in a horizontal fracture:

$$x_w \approx \begin{cases} ß_1 t^{1/2} & t < t_1 \\ ß_2 t^{1/4} & t_1 < t < t_2 \\ ß_3 t^{1/2} & t_2 < t \end{cases} \quad (3)$$

where $ß_1 = (D_f/\pi)^{1/2}$ (3a)

$ß_2 = ß_1 t_1^{1/4} (2/\pi)^{1/2}$ (3b)

$ß_3 = ß_1 (V_f / V_J)^{1/2}$ (3c)

Philip and Farrell [1964] used LaPlace transform methods to solve an analogous problem in which water advances within an agricultural furrow and simultaneously infiltrates into the underlying soil. The solution to this problem was limited to constant flow at the furrow inlet. For this condition, the position of the wetting front in the furrow, analogous to wetting front position in the fracture, was found to be linearly related to $t^{1/2}$, which is consistent with the late-time solution shown above.

5.2 Imbibition Volumes

Calibration parameters for the Nitao and Buscheck imbibition model (i.e., α_i and t_i) were estimated using cumulative imbibition volumes (Figure 5.3). A middle-to-late transition time, was identified based on the substantial change in slope at approximately 148 hours. This time is consistent with the observed time of 146 hours corresponding to when the visual wetting front position reached the far end of the block. The Nitao and Buscheck model incorporates only infinite fractures, so this time is not consistent with the postulated hypothesis that the transition time results from lateral no-flow boundaries. The relevant value of t_2 is therefore > 148 hours.

No apparent change in slope was present at earlier times. In fact, the cumulative imbibition volume is reproduced with an accuracy of 3.0 percent for all times up until 148 hours by neglecting the initial volume which was assumed to fill the fracture manifold. The exponent on time for the observed imbibition rates was estimated to be -0.263 $\pm$ 0.003, which is in reasonably good agreement with the exponent predicted for the second phase by the Nitao and Buscheck model, -0.250. The second-phase imbibition coefficient, α_2, was estimated to be 3.72 $\pm$ 0.28 $cm^2\ hr^{-1/4}$ assuming the exponent to be equal to its theoretical value of -0.25. The transition from the first to second phase, t_1, was not observed and was assigned an upper limit of 0.033 hours. The calibrated second-phase imbibition equation is also presented in Figure 5.3.

Figure 5.3 also presents a comparison of model predictions with observed data. As is evident in the figure, the model approximates the transition times between the three periods, and reproduces the slope of the observed data. On the other hand, the prediction equation overestimates the observed imbibition flux during all periods. The difference between the calibrated and predicted value of t_2 can be attributed to the spatial variability of the hydraulic diffusivity, as well as the possibility of entrapped air retarding the advance of the wetting front in the rock matrix. Values of the calibration parameters are presented in Table 5.2.

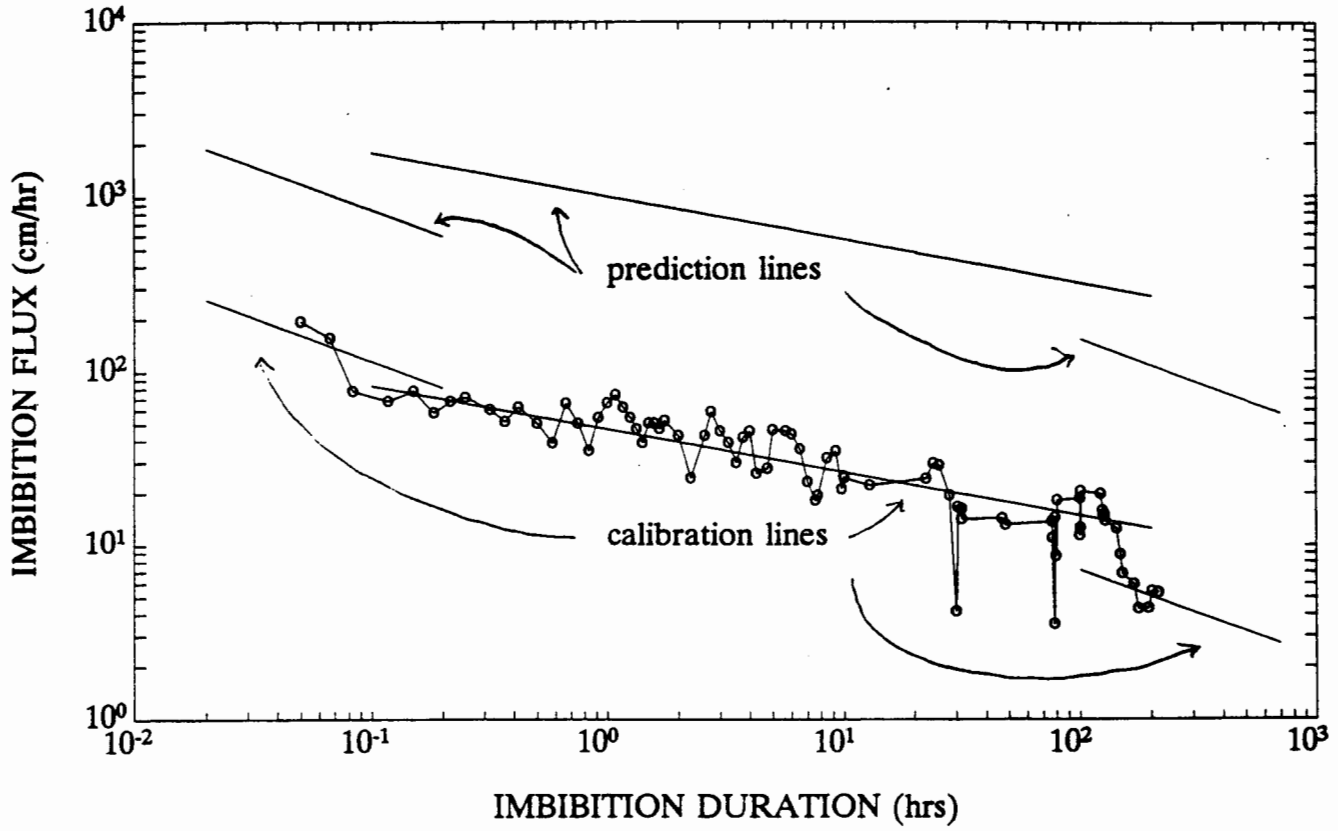

Figure 5.3: Cumulative imbibition volumes; observed (symbols) and calibrated (line).

TABLE 5.2
Fractured block derived parameters.

	Predicted	Calibrated	
Transition Times:			
t_1 (hr)	0.1 ± 0.1	< 0.03	
t_2 (hr)	96.1 ± 71.3	> 148	
Imbibition Coefficients:			
α_1 ($cm^2/hr^{1/2}$)	0.0004	-	
α_2 ($cm^2/hr^{1/4}$)	0.0010	3.72 ± 0.28	
α_3 ($cm^2/hr^{1/2}$)	0.00007	-	
Wetting Front Coefficients:			
$ß_1$ ($cm/hr^{1/2}$)	139.	-	$cm\ hr^{-1/2}$
$ß_2$ ($cm/hr^{1/4}$)	62.3	27.8 ± 5.4	$cm\ hr^{-1/4}$
$ß_3$ ($cm/hr^{1/2}$)	24.6	-	$cm\ hr^{-1/2}$

NOTE: Prediction uncertainties estimated using Taylor-series approximation (Table 3.3).

5.3 Wetting Front Position

Fracture wetting front position data were available only for the second phase, where $t_1 < t < t_2$. The exponent on time for the observed wetting front position was estimated to be 0.271 ± 0.344, which is also reasonably close to the theoretical value of 0.250. The second-phase wetting front position coefficient, $ß_2$ was estimated to be 27.8 ± 5.4 cm $hr^{1/4}$. Phase transition times were not estimated from the wetting front position data due to the paucity of position data. Figure 5.4 presents the observed and calibrated visual wetting front positions in the rock fracture.

An assumption violated during the experiment was that of constant fracture saturation behind the wetting front, i.e., ΔS_f = constant. Estimates of ΔS_f were obtained by visually noting the length of saturated rock matrix immediately adjacent to the fracture and dividing by the furthermost extent of wetting along the fracture. Figure 5.5 presents a plot of the fracture saturation over time. For early time $\Delta S_f \approx 0.10$, increasing to unity by 24 hours. The possibility for fingered fluid flow within the fracture is a process neglected in the Buscheck and Nitao model. Such fingering is expected to be substantial in vertical fractures.

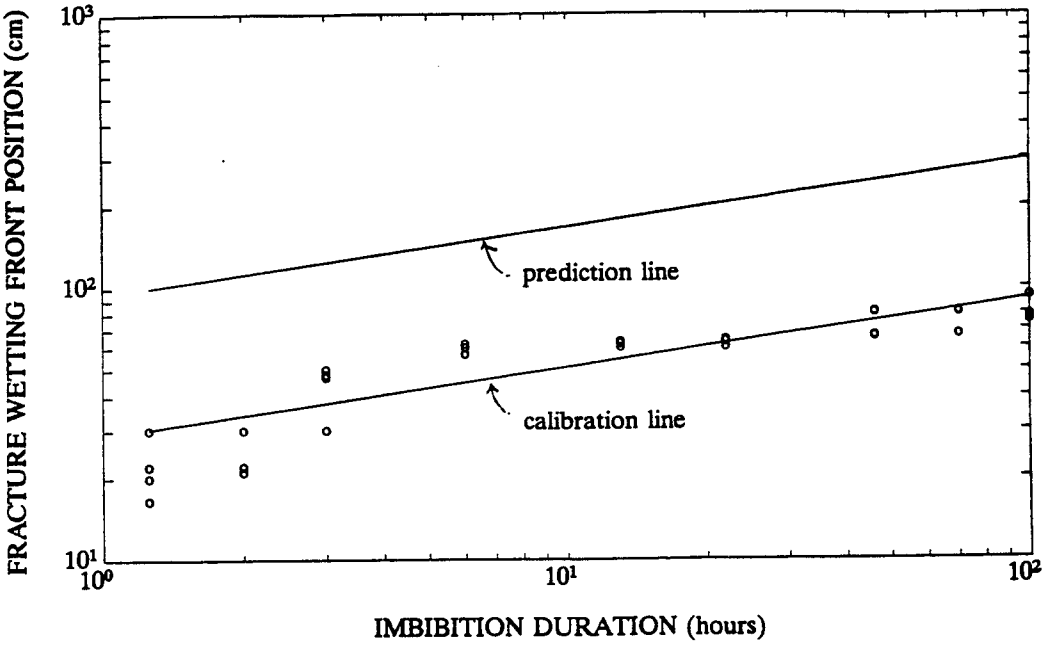

Figure 5.4: Fracture wetting front position; observed (circles) and calibrated (line).

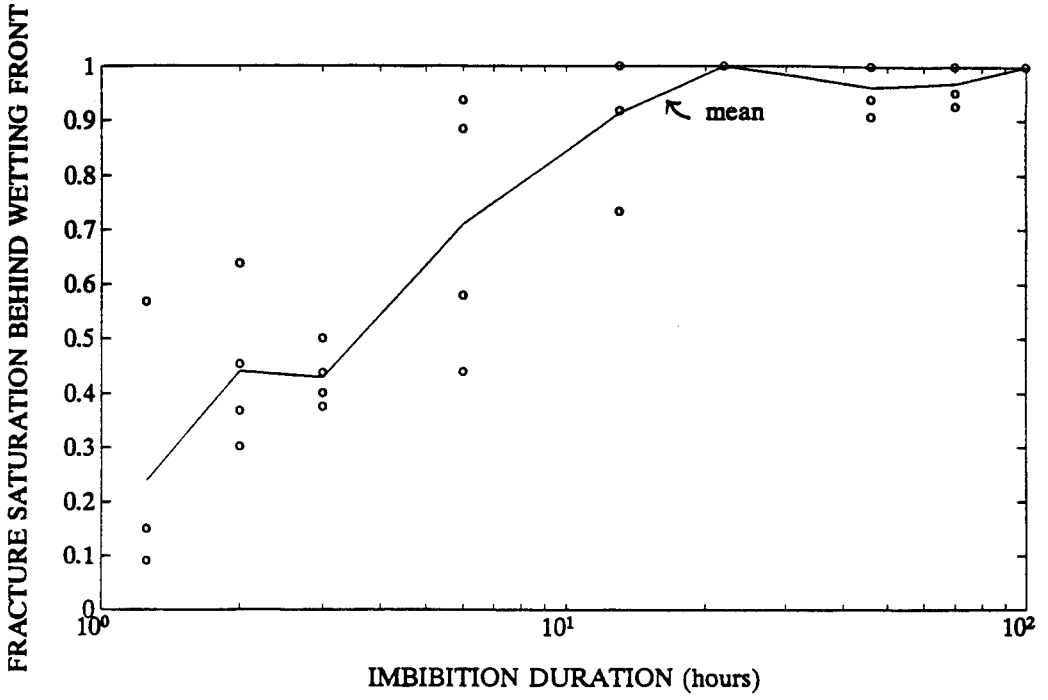

Figure 5.5: Observed mean fracture saturation behind wetting front.

The observed fracture wetting front position is indicated in Figure 5.4 along with prediction and calibration positions. It is evident from the figure that the prediction parameters overestimate the observed wetting front advance. If the value of t_1 is assumed to equal the prediction value during Phase 2, then the value of D_f can be calculated. This value is also shown in Table 5.2. Like the calibration parameters obtained from imbibition flux data, the wetting front value of D_f is substantially less than the prediction value, although not as low as the calibration values.

5.4 Discussion

Data from the imbibition experiment reported here confirms the second phase of the Nitao and Buscheck model. The experiment was not able to distinguish either the first or third phase of their model. A new phase was observed, however, which resulted from the finite length of the fracture within the tuff. The Nitao and Buscheck model should be extended to incorporate the finite extent of discrete fractures. Another concern raised by the experiment was the failure to properly estimate fracture hydraulic properties. It is observed that laboratory estimates of rock fracture hydraulic properties, when used with the Nitao and Buscheck model, substantially overestimated the cumulative imbibition rate, and the rate of advance of the wetting front in the fractured block. Calibrated values of the fracture hydraulic parameter are substantially less than the characterization value. An additional shortcoming of the model is the inability to reproduce the observed fingering of water within the fracture, although the fingering was limited only to the early fracture imbibition period. Fingering may be more important when vertically oriented fractures are present.

6. FIELD AIR INJECTION EXPERIMENTS

Amado G.-Guzman and Shlomo P. Neuman

To conduct defensible safety analyses of high level radioactive waste repositories in geologic media, it is necessary to reliably model fluid and contaminant transport around such repositories. Not only must models describe flow and transport processes in the geosphere reliably but they must be operational by relying on measurable inputs, and verifiable by generating outputs that can be compared with observations. The potential high level waste repository at Yucca Mountain in Nevada will be located in an unsaturated fractured tuff environment, underlain by a fractured carbonaceous aquifer. Mathematical models of flow and transport in this environment must be based on equations and algorithms which reliably describe multiphase flow and transport in porous-fractured tuffs, must admit measurable flow and transport parameters, and must produce outputs at least partially verifiable in the field. To address the question what constitutes a reliable model of flow and transport in environments similar to those which prevail at Yucca Mountain, and to resolve the issue how one evaluates the corresponding parameters on the basis of appropriate field measurements, the University of Arizona (UAz) has been conducting research at the Apache Leap Tuff Site (ALTS) near Superior, Arizona. The work is sponsored by the US Nuclear Regulatory Commission (NRC) under Contracts NRC-04-90-51 (FIN L1282) and NRC-04-90-052 (FIN L1283).

The UAz research at ALTS has several components. This chapter concerns pneumatic permeability tests within inclined shallow boreholes at the site. Issues being investigated include the proper conduct and interpretation of such tests in single boreholes, the extent to which fractured and porous block permeabilities can be identified, the extent to which fracture geometric data can be used to help predict permeabilities, the effects of phenomena such as two-phase flow and inertia (including variations of permeability with pressure and saturation), scale -dependence of the test results, upscaling of the test results to obtain effective permeabilities for larger rock blocks, spatial and directional variability of single-hole air permeabilities, the extent to which single-hole tests results can be used to predict permeability variations between boreholes, corroboration of such predictions by means of cross-hole fluid and tracer tests, and the extent to which air permeabilities are indicative of permeabilities to water. Two phase flow simulations using the code VTOUGH, geostatistical tools, and stochastic models are used in support of the investigation. One question of interest is the role that continuum and discontinuum concepts must play in models of flow and transport in the context of available, or potentially available, data.

The bulk of the experimental data presented in this report is being published concurrently as a NUREG report entitled Validation Studies for Assessing Flow and Transport Through Unsaturated Fractured Rock [Bassett et al., 1994]. Here the material is presented in the context of validation issues. Also, new data not available during the preparation of that report is included. The geostatistical analysis encompass all the data available to date.

6.1 Experimental Setup

There are currently twenty-one 4-in diameter boreholes which vary in depth from about 11 m to about 32 m at the site. These boreholes were drilled in sets of three which are labeled the X-, Y-, Z-, V-, and W-series. The area around the boreholes is covered by a thick plastic liner. Another G-series consists of six boreholes outside the plastic cover. The V- and G- series consist of vertical boreholes; the other boreholes are slanted at a 45° angle. The azimuth of the X and Y slanted boreholes is of 90° (CCW from North), that for the W boreholes 180°, and that of the Z boreholes

270° (see Figure 6.1). Testing to date has centered on borehole Y2 and its neighbors at the center of the experimental site.

Air permeability testing is conducted with a straddle-packer system furnished with rubber glands about 1.68 m in length. The interval between the glands is variable to allow testing at different measurement supports. A permeability test consists of imposing an increasing sequence of flow rates (a minimum of three) each of which is extended until a steady state pressure response is attained. The working definition for steady state is a pressure change of 0.1 cm (Hg) or less within an interval of 30 minutes. A schematic representation of the injection system and its major components is shown in Figure 6.2. Air pressure, temperature and relative humidity are measured at the surface and at the injection interval. Atmospheric temperature and pressure are also monitored. The flow rate is preset at the surface with the aid of electronic mass flow controllers. The experimental parameters are recorded at a logarithmic time scale, starting at 2 seconds at early time for each flow rate and increasing up to 2 minutes after 90 minutes of observation. All data are recorded automatically and electronically. At the end of an injection sequence, the temperature, pressure, and relative humidity in the interval are allowed to recover to their initial conditions. These recovery data are also monitored. After a test is completed, one has at least seven different sets of data which can be used to determine the air permeability of the rock surrounding the interval; three transient sets during injection, three steady state sets and one recovery set.

The analysis presented here concerns only steady state data. Water capillary displacement affects the transient data to an extent that renders the application of available single-phase interpretation techniques unreliable. The transient data sets should be interpreted in the context of multiphase flow, but we do not at present have the tools to do so. An alternative to analytical analysis of the transient data is their interpretation by numerical inverse procedures as suggested by Finisterle and Pruess [1994]. We hope to do so in the future. The following section offers a brief account of the steady state analysis. The interested reader is referred to Guzman [1994] and Bassett et al. [1994] where a more detail description is presented.

6.2 Steady State Interpretation

Hvorslev [1951] and Hsieh et al. [1983] present an analytical expression for the spatial distribution of steady state water pressure around a hydraulic injection test interval which considers the equipotentials to form prolate spheroids. Modified for air, this expression takes the form:

$$Q_{sc} = 4\,\pi\,L\,\frac{k}{\mu}\,\frac{T_{sc}}{T\,p_{sc}\,Z}\,\frac{p^2 - p_o^2}{\sinh^{-1}[\frac{L/2+z}{r}] + \sinh^{-1}[\frac{L/2-z}{r}]} \qquad (6.1)$$

where

- Q_{sc} volumetric flow rate at standard conditions
- k air permeability
- μ air viscosity
- L distance between the straddle packers
- T air temperature in the injection interval
- p_{sc} pressure at standard conditions (1 atm)
- T_{sc} temperature at standard conditions (20°C)
- Z air compressibility
- p_o ambient air pressure
- p air pressure in the rock at a radial distance r and vertical distance z from a point at the center of the interval.

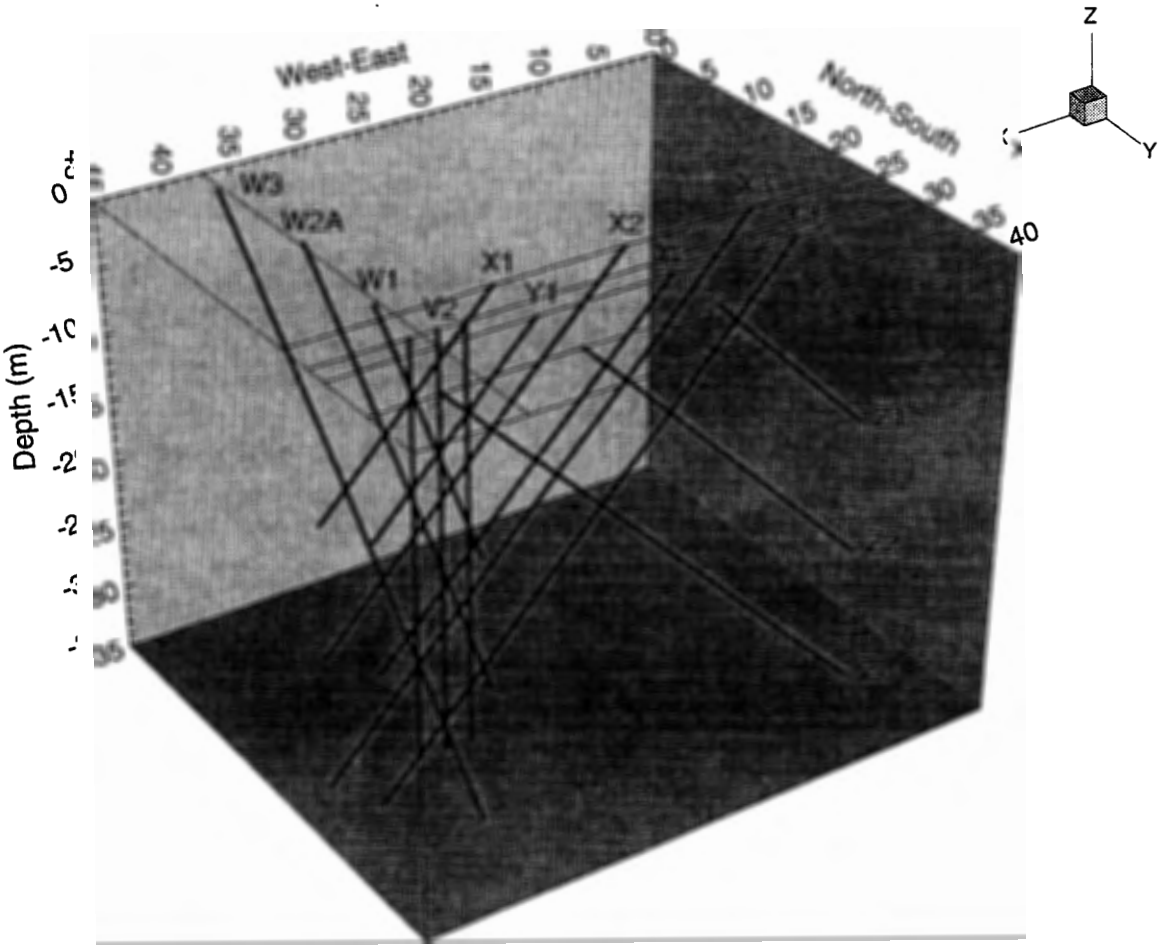

Figure 6.1: Spatial location of boreholes at ALTS.

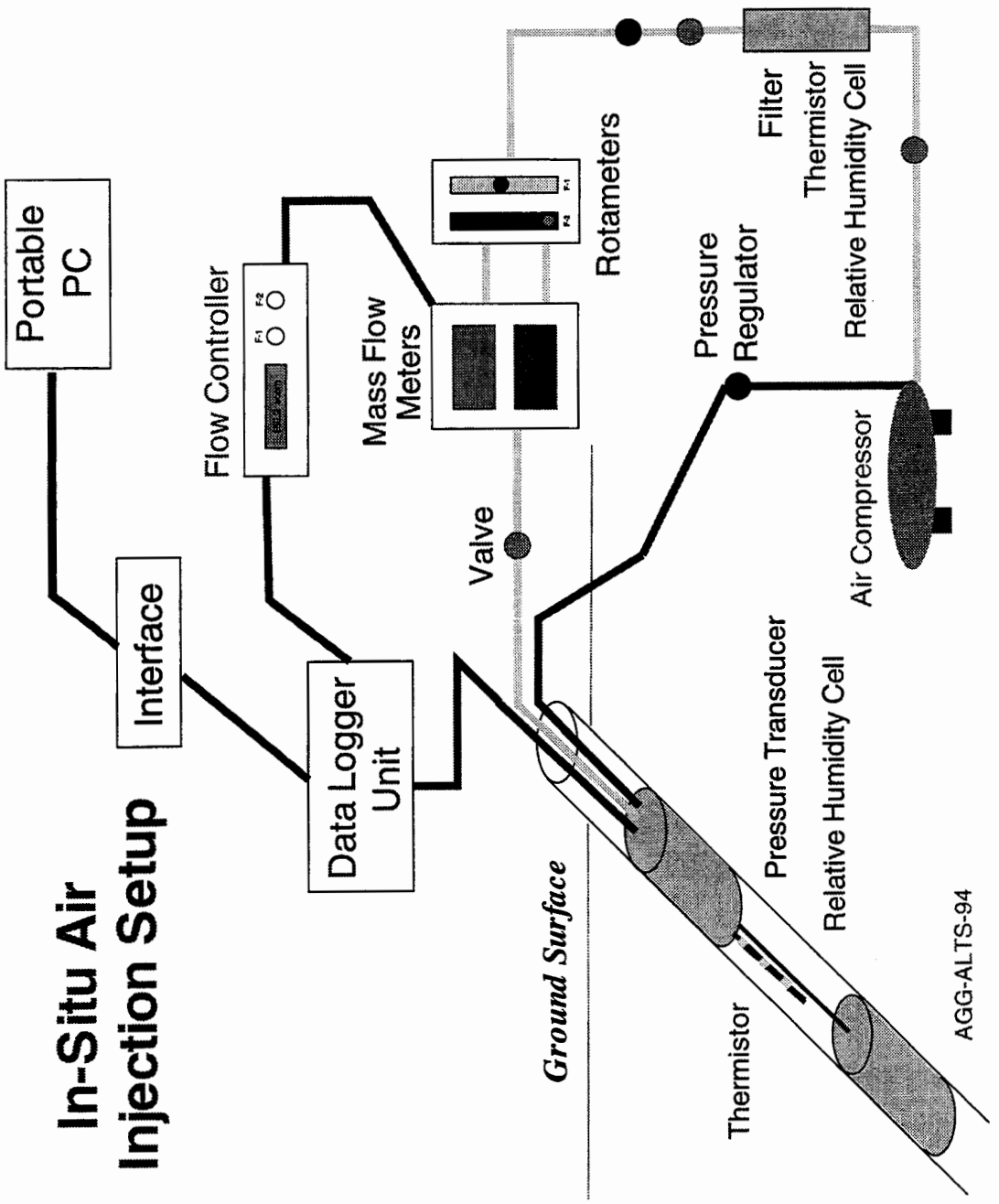

Figure 6.2: Schematic representation of the air injection system.

The pressure in the test interval, p_w, is usually associated with $z=0$ and the borehole radius $r=r_w$. If $L/r_w >> 1$, flow is predominantly radial and Equation 6.1 can be written as

$$k = Q_{sc} \frac{\mu \, Ln(L/r_w)}{\pi \, L \, (p^2_w - p^2_o)} \frac{T \, p_{sc} \, Z}{T_{sc}} \qquad (6.2)$$

Equation 6.2 has the advantage over standard radial flow equations that it does not require introducing a fictitious radius of influence. At ALTS, air injection has to date been conducted on scales (in terms of L) of 0.5 m, 1.0 m and 3.0 m. As the radius of each borehole is about 0.05 m, the smallest aspect ratio in our test is $L/r_w = 10$. Figure 6.3 shows how the ratio of k^R from the radial flow Equation 6.2 and k^P from the prolate spheroidal flow Equation 6.1 varies with L when $r_w = 0.05$ m. It follows from this figure that, under our test conditions, calculations resulting from the radial flow Equation 6.2 differs from those from Equation 6.1 by not more than 0.5%.

Local heterogeneities (layers, lenses, fractures, other) and anisotropy may alter the steady state flow regime around the test interval. When layers or fractures intersect this interval, flow in the rock may be predominantly two-dimensional. If preferential flow channels exist in such layers or fractures, flow in them may be predominantly one-dimensional. Intermediate flow regimes corresponding to non-integer (fractal) dimensions may also develop in some cases [Barker, 1989].

Table 6.1 summarizes the in-situ permeability data available to date as well as local 3-D coordinates. A number of permeability values, resulting from different flow rates and repeated testing, are reported for each interval. There are two sections in Table 6.1, one including the permeability data obtained from tests along borehole Y2 at three different scales of measurement (0.5, 1.0 and 3.0 m), and the 1.0-m data for all the other boreholes (X2, V2, W2A, Z2 and Y3).

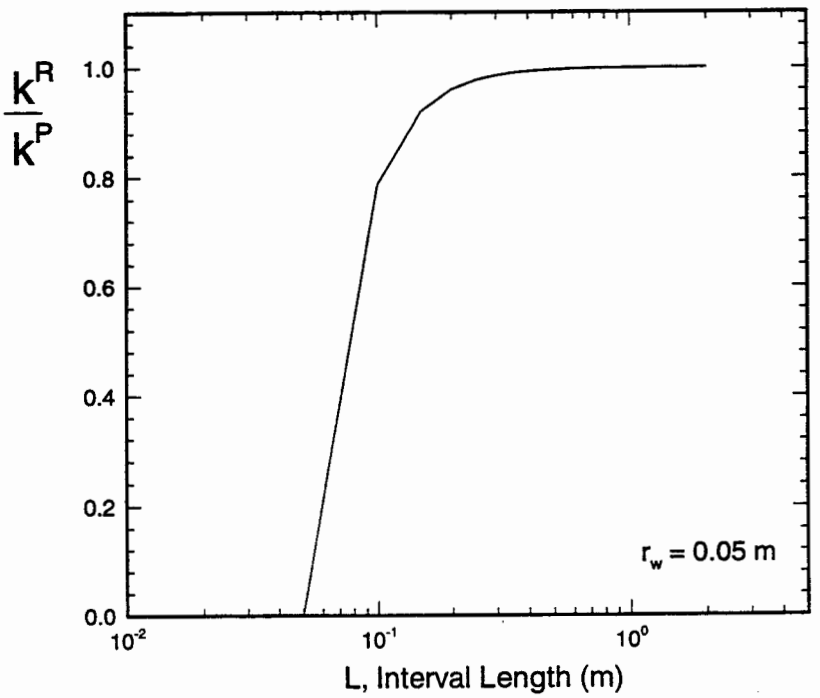

Figure 6.3: Ratio of apparent permeability estimates from the radial and prolate spheroidal analytical solution.

Table 6.1

Field-scale estimates of apparent permeability using air (units of 10^{-16} m^2) vs. depth (m) for a range of applied pressures (units of cm-Hg)

Borehole: Y2 Scale: 3.0 m

Xo = 20.25 m Yo = 29.85 m Zo = -0.34 m

L(m)	Kmin	Kmax	Pmin	Pmax	Ln(Kmean)
4.08	49.9	53.1	109.16	118.69	-32.90
6.37	7.23	8.51	116.99	125.25	-34.78
9.37	9.11	12.3	111.96	115.93	-34.47
12.37	19.3	23.7	110.15	130.28	-33.77
15.37	206.	287.	107.64	68.16	-31.33
18.37	30.1	32.9	114.09	75.94	-33.39
21.37	6.94	11.9	103.97	119.82	-34.60
24.37	8.47	9.21	114.50	128.70	-34.66
27.37	1.42	1.74	120.71	138.74	-36.38

Table 6.1: (continued)

Borehole: Y2 Scale: 1.0 m

Xo = 20.25 m Yo = 29.85 m Zo = -0.34 m

L(m)	Kmin	Kmax	Pmin	Pmax	In(kmn)
3.07	95.41	98.50	71.92	86.32	-32.27
4.05	22.36	27.22	107.85	120.51	-33.63
5.03	6.068	7.071	122.65	136.55	-34.96
6.01	11.75	12.33	99.13	119.36	-34.35
6.99	1.800	2.502	115.43	175.05	-36.08
7.97	2.171	2.936	139.47	154.91	-35.90
8.95	3.864	5.302	113.60	135.17	-35.32
9.93	19.07	21.97	93.01	128.17	-33.82
10.91	16.36	20.10	96.91	129.32	-33.94
11.89	29.41	31.97	84.54	116.84	-33.42
12.87	20.50	23.15	95.87	131.20	-33.76
13.85	20.11	22.69	91.88	132.20	-33.78
14.83	26.49	28.50	86.43	90.13	-33.53
15.81	451.6	494.3	71.03	67.74	-30.68
16.79	466.5	485.6	67.23	67.85	-30.68
17.77	55.25	56.87	72.23	90.06	-32.81
18.75	33.56	35.98	79.46	114.35	-33.29
19.73	19.05	20.42	93.15	128.41	-33.86
20.71	4.621	5.560	136.56	149.34	-35.21
21.69	8.692	11.76	90.38	119.27	-34.52
22.67	11.51	14.79	85.02	124.61	-34.27
23.65	13.39	15.65	82.35	122.11	-34.17
24.63	1.970	3.478	91.68	126.82	-35.84
25.61	.4718	.8815	129.41	164.01	-37.23
26.59	.9005	1.666	102.29	104.53	-36.59
27.57	1.043	1.401	101.64	127.41	-36.64
28.55	.5627	.7454	128.03	144.61	-37.27
29.00	.5781	.7956	117.92	128.74	-37.22

Table 6.1: (continued)

Borehole: Y2 Scale: 0.5 m

Xo = 20.25 m Yo = 29.85 m Zo = -0.34 m

L(m)	Kmin	Kmax	Pmin	Pmax	Ln(Kmean)
2.83	15.6	22.5	94.95	124.00	-33.911
3.33	147.	162.	92.58	71.54	-31.802
3.83	28.9	34.8	92.93	113.38	-33.385
4.33	5.62	7.16	132.53	147.24	-34.994
4.83	3.10	4.27	111.06	126.81	-35.550
5.33	8.00	9.81	109.96	130.31	-34.660
5.83	17.4	18.8	93.14	132.58	-33.946
6.33	1.11	1.67	142.60	139.36	-36.532
6.83	.746	.975	167.40	172.89	-37.000
7.33	2.81	3.52	115.59	149.08	-35.696
7.83	1.26	1.71	135.36	148.68	-36.459
8.33	1.73	2.56	120.60	137.56	-36.098
8.83	2.19	3.45	126.35	150.48	-35.829
9.23	4.47	4.47	135.55	135.55	-35.344
9.74	22.5	28.7	84.36	132.13	-33.606
10.33	5.91	9.26	92.65	123.30	-34.840
10.83	13.1	19.2	82.81	132.04	-34.077
11.33	16.1	22.7	82.14	132.79	-33.891
11.83	29.2	33.0	78.09	125.76	-33.406
12.23	24.3	28.7	77.00	132.08	-33.568
12.83	9.23	12.4	91.99	132.17	-34.470
13.33	13.3	19.9	84.97	139.63	-34.054
13.83	15.4	20.0	82.62	139.46	-33.977
14.33	15.7	22.2	82.46	133.99	-33.916
14.83	29.9	34.2	78.07	126.99	-33.376
15.33	26.2	31.7	79.46	130.68	-33.480
15.83	32.8	38.8	80.82	129.09	-33.267
16.33	719.	818.	70.07	87.64	-30.199
16.83	31.9	47.3	111.50	132.84	-33.182
17.33	30.5	37.5	78.00	128.34	-33.320
17.83	44.5	56.0	74.34	114.58	-32.931
18.33	40.1	51.2	75.26	117.07	-33.028
18.83	15.8	25.8	82.33	137.76	-33.836
19.33	8.93	12.5	100.09	135.94	-34.485
19.83	19.2	25.1	79.81	128.18	-33.752
20.33	3.16	4.55	103.70	124.24	-35.508
20.83	3.02	4.26	100.66	131.70	-35.564
21.33	6.08	10.1	87.75	124.85	-34.782
21.83	6.38	8.59	91.10	114.61	-34.840
22.33	5.59	10.1	86.69	138.33	-34.823
22.83	14.2	15.5	88.15	125.30	-34.143
23.33	16.0	18.9	77.11	125.03	-33.985
23.83	6.98	9.13	98.77	129.48	-34.764
24.33	4.13	5.31	109.60	144.78	-35.296
24.83	1.81	2.27	121.26	144.80	-36.136
25.33	.847	.853	162.41	163.39	-37.004
25.83	.714	.857	152.64	160.71	-37.086
26.33	.921	1.07	138.53	146.93	-36.847
26.83	1.57	2.07	113.68	139.35	-36.253
27.33	1.55	2.16	114.50	138.95	-36.237
27.83	1.13	1.25	128.13	142.38	-36.669
28.33	.441	.536	157.10	172.84	-37.563
28.83	.755	1.10	126.02	146.50	-36.934
29.23	.914	1.16	123.51	146.11	-36.814

Table 6.1: (continued)

Borehole: X2 Scale: 1.0 m

Xo = 19.88 m Yo = 24.99 m Zo = -0.05 m

L(m)	Kmin	Kmax	Pmin	Pmax	Ln(Kmean)
2.51	17.6	43.5	72.61	94.88	-33.521
3.49	279.	339.	67.55	73.71	-31.112
4.47	13.5	19.6	108.68	139.83	-34.054
5.45	10.8	28.4	78.86	114.84	-33.977
6.43	1.93	2.65	113.80	131.06	-36.025
7.41	1.64	2.43	128.51	143.98	-36.151
8.39	13.8	23.0	95.47	126.05	-33.962
9.37	7.51	12.6	114.84	133.21	-34.565
10.35	11.0	16.5	109.11	131.59	-34.237
11.33	822.	905.	67.36	68.45	-30.081
12.31	17.7	24.3	117.29	131.70	-33.811
13.29	4.47	10.4	83.73	117.84	-34.921
14.27	15.7	30.6	86.66	121.00	-33.752
15.25	13.7	42.2	78.65	86.45	-33.662
16.23	17.2	32.1	85.31	118.98	-33.685
17.21	7.15	15.7	94.70	137.92	-34.48
18.19	8.21	19.6	79.82	120.39	-34.302
19.17	13.8	21.5	82.21	116.74	-33.994
20.15	3.61	7.83	88.35	137.87	-35.17
31.13	1.15	3.05	100.00	123.07	-36.214
22.11	1.80	6.84	100.02	137.75	-35.586
23.09	15.4	39.7	77.40	108.46	-33.633
24.07	.771	1.18	121.84	134.52	-36.889
24.00	.218	.708	108.61	124.95	-37.775
25.00	.327	1.85	96.49	198.81	-37.093
26.00	.582	3.00	84.53	177.16	-36.563
27.00	1.43	2.73	77.88	158.14	-36.161
28.00	1.35	2.86	78.56	163.75	-36.166
29.00	1.14	2.59	80.39	157.98	-36.299
30.00	.546	1.53	94.09	159.62	-36.931

Table 6.1: (continued)

Borehole: V2 Scale: 1.0 m

Xo = 36.00 m Yo = 28.10 m Zo = -0.00 m

L(m)	Kmin	Kmax	Pmin	Pmax	Ln(Kmean)
2.37	.0879	.415	117.18	167.00	-38.50
3.38	.312	.364	158.07	162.82	-37.93
4.37	.487	.714	144.41	164.08	-37.37
5.37	.585	.925	118.82	132.81	-37.15
6.37	.559	1.06	126.40	141.09	-37.11
7.37	.898	2.28	107.69	122.70	-36.48
8.37	321.	369.	66.67	72.10	-31.00
9.37	4.47	29.4	88.88	114.83	-34.40
10.37	12.9	20.3	96.71	114.63	-34.06
11.37	14.0	57.8	78.13	93.76	-33.49
12.37	7.67	9.72	103.25	119.88	-34.69
16.37	2.83	6.36	84.89	130.65	-35.40
17.37	.655	.927	129.03	147.76	-37.09
18.37	1.08	2.00	108.81	142.68	-36.45
19.37	.858	1.42	117.32	155.73	-36.74
20.37	.777	1.94	121.54	145.05	-36.64
21.37	.745	1.30	123.11	151.72	-36.86
22.37	4.66	7.85	72.35	114.15	-35.04
23.37	.265	.265	186.46	186.46	-38.17
24.37	.199	.199	156.65	156.65	-38.46
25.37	.133	.133	169.66	169.66	-38.86

Table 6.1: (continued)

Borehole: W2A Scale: 1.0 m

Xo = 36.80 m Yo = 13.20 m Zo = -0.00 m

L(m)	Kmin	Kmax	Pmin	Pmax	In(Kmean)
2.75	52.6	112.	71.83	149.17	-32.499
2.55	70.3	116.	82.32	147.01	-32.34
3.53	1.46	13.4	88.13	170.40	-33.355
4.53	.713	1.96	126.83	159.57	-36.673
5.53	.876	1.50	152.36	162.09	-36.704
6.53	1.63	6.66	97.46	138.73	-35.65
7.53	1.85	11.7	93.88	159.21	-35.303
7.55	.654	14.0	82.24	165.44	-35.734
8.53	5.11	52.1	87.07	172.06	-34.049
9.53	9.82	54.4	77.74	168.85	-33.701
10.53	1.35	2.92	128.69	155.20	-36.158
11.55	1.50	5.88	99.33	179.45	-35.753
12.55	1.24	2.81	104.18	164.98	-36.218
13.55	1.62	10.1	79.21	153.22	-35.446
14.55	3.53	12.3	72.46	154.66	-34.954
15.55	5.75	24.4	69.95	132.00	-34.369
16.55	29.7	42.1	67.52	109.11	-33.275
17.55	21.0	39.0	71.43	91.96	-33.486
18.55	29.7	58.3	69.69	98.92	-33.114
19.55	3.63	13.3	72.34	167.14	-34.903
20.55	11.8	19.8	67.18	142.99	-34.115
21.55	9.98	19.8	66.89	142.91	-34.197
22.55	3.78	10.9	69.37	162.52	-34.981
23.55	2.88	7.76	71.93	158.63	-35.287
25.55	2.02	38.8	79.55	112.12	-34.661
26.55	2.43	3.73	70.69	92.97	-35.74
27.55	2.14	4.15	71.06	177.35	-35.751
28.55	1.78	4.66	71.96	169.03	-35.785
23.70	4.00	9.01	70.09	176.72	-35.05
24.90	22.9	41.8	66.32	109.14	-33.409
25.90	2.86	5.30	69.42	101.28	-35.482

Table 6.1: (continued)

Borehole: Z2 Scale: 1.0 m

Xo = 30.58 m Yo = 34.99 m Zo = -0.21 m

L(m)	Kmin	Kmax	Pmin	Pmax	Ln(Kmean)
2.58	3.94	4.92	159.14	167.07	-35.359
3.58	1.23	4.68	104.92	148.29	-35.967
4.56	1.48	5.95	99.35	144.57	-35.753
5.56	1.26	5.87	103.89	145.22	-35.839
6.56	.892	3.26	115.84	171.48	-36.308
7.56	1.01	2.74	111.30	167.31	-36.335
8.56	1.80	4.59	93.90	170.61	-35.785
9.56	126.	141.	70.57	81.14	-31.949
10.56	72.2	102.	73.83	86.62	-32.39
11.56	56.3	66.4	84.88	95.59	-32.728
12.56	125.	138.	74.98	81.52	-31.963
13.56	512.	528.	68.24	70.49	-30.588
14.56	30.7	66.9	73.42	95.52	-33.027
15.56	11.7	34.2	84.01	116.89	-33.846
16.53	4.05	21.7	74.59	139.36	-34.603
17.53	1.79	2.34	135.94	148.20	-36.125
18.53	725.	776.	67.56	70.04	-30.221
19.53	1.42	5.05	100.74	143.61	-35.856
20.53	.288	.376	156.40	162.78	-37.953
21.53	.254	.254	164.67	164.67	-38.213
22.53	372.	409.	69.46	79.69	-30.875
23.53	.818	2.72	102.86	168.67	-36.442
24.53	.719	2.91	111.71	180.22	-36.473
25.53	.496	1.30	125.93	171.88	-37.06
26.53	1.29	33.2	85.26	94.25	-34.962
27.53	13.3	58.3	69.83	167.41	-33.513
28.53	25.3	95.6	68.10	157.82	-32.947
29.53	22.0	57.7	68.22	155.33	-33.267

Table 6.1: (continued)

Borehole: Y3 Scale: 1.0 m

Xo = 10.22 m Yo = 29.68 m Zo = -0.32 m

L(m)	Kmin	Kmax	Pmin	Pmax	Ln(Kmean)
2.55	463.	515.	68.57	71.25	-30.651
3.55	50.3	77.3	86.74	169.46	-32.709
4.55	119.	262.	67.09	128.16	-31.669
5.55	17.2	95.1	72.84	170.95	-33.141
6.55	3.79	29.8	80.81	167.96	-34.478
7.55	9.30	75.6	69.97	171.82	-33.564
8.55	13.6	85.6	70.63	163.13	-33.312
9.55	34.0	66.9	66.86	95.45	-32.976
10.55	85.5	137.	71.30	173.95	-32.157
11.55	5.60	65.9	75.48	95.78	-33.886
12.55	6.15	183.	74.77	150.24	-33.328
11.55	83.8	141.	119.84	163.89	-32.154
13.55	3.69	28.0	70.51	162.75	-34.522
14.55	3.64	26.3	69.03	167.35	-34.561
15.55	4.81	26.5	70.49	166.65	-34.418
16.55	6.16	18.5	75.48	191.92	-34.472
17.55	.484	3.56	126.05	178.28	-36.568
18.55	.102	.335	143.09	168.65	-38.529
19.55	.396	.708	134.50	147.23	-37.476
20.55	2.20	11.5	71.29	146.02	-35.226
20.55	.102	.102	168.44	168.44	-39.125
20.55	.0745	.0745	162.65	162.65	-39.438
23.55	6.89	20.6	67.90	166.30	-34.364

6.3 Pressure Dependence

When Equation 6.2 applies, knowledge of the flow rate, pressure and temperature in the test interval allow computing k. In multiple flow rate tests such as ours, one can compute a k for each flow rate. Under viscous flow and under a single phase flow regime, application of Equation 6.2 results in a number of k-estimates which differ from each other due to experimental error (white noise). In most of our tests, however, such k values either decrease (Figure 6.4a) or increase (Figure 6.4b) consistently with increasing mean pressure (the arithmetic average of p_w and p_o). In other words, our tests indicate that in-situ air permeability as obtained by means of Equation 6.2 is non-unique, depending strongly on the applied mean pressure. This kind of permeability increase was observed by Wentworth [1944] during gas flow through thin cracks in lava rock. He attributed the phenomenon to an enhancement of permeability due to gas adsorption on the rock surfaces. Estes and Fulton [1956] observed a similar enhancement in permeability when studying slip phenomena in sandstone and limestone cores. They attributed the increase in permeability with flow rate to experimental difficulties at higher liquid saturations due to redistribution of the liquid phase within the cores. Montazer [1982] briefly mentioned the possible effects of moisture on his permeability measurements. We suspect that the enhancement of permeability observed by these authors, and by us in numerous intervals at ALTS, may be attributed to displacement of water, which partially blocks air movement, by air. Other mechanisms such as rock deformation, leakage around the packers, or gas diffusion and adsorption are in our view less likely to act as the primary causes of this consistent phenomenon at ALTS. That two-phase flow causes k to increase is strongly supported by our numerical experiments, described in detail in Guzman [1994]. These experiments also reproduce the behavior observed in Figure 6.5, where the pressure during a constant flow rate injection test first increases to a maximum and then decreases slowly toward a steady state value.

Other behavior which suggests two-phase flow effects, and is reproduced well by our numerical experiments, is that observed during two types of specially designed field experiments. In the first type, air was injected at a step-wise increasing sequence of flow rates followed by a step-wise decreasing sequence back to the initial value. In the second type, air injection started at a very low flow rate and increased gradually to the maximum allowed by our equipment (20 slpm, standard liters per minute). In both types of experiments, the total air pressure at the injection interval was kept at less than 250 KPa. Figure 6.6 shows the results of two experiments of the first type completed in boreholes Y2 and X2 at measurement supports of 0.5 m and 1.0 m. The arrows indicate directions of change in the flow rate and mean pressure. For example, the test depicted in Figure 6.6 consisted of the following flow rate sequence: 500, 750, 1000, 1200, 750 and 500 sccm (standard cubic centimeter per minute). It is seen that equilibrium pressures during flow rate increase are consistently larger than those during flow rate decrease. On the other hand, air permeabilities are smaller during flow rate and mean pressure increase than during their decrease. This hysteretic behavior is commonly observed during laboratory determinations of non-wetting phase relative permeability [Anderson, 1987] and has the following simple two-phase flow explanation. When air is injected into the medium, some water evaporates and some is forced out of larger voids (due to capillary pressure re-equilibration) into smaller voids. Increasing flow rate, and consequently increasing air pressure, results in higher capillary pressure which in turn produces a larger pore space to be occupied by air and thereby in an enhancement of air permeability. This physical behavior is analogous to that relied upon by the Hassler [1952] method to determine relative permeabilities for rock cores in the laboratory. When the flow sequence is reversed and the resulting mean air pressure decreases; the capillary pressure decreases and some water moves back toward the borehole. Some of it, however, remains in vapor phase, and some has difficulty returning from small to larger voids due to the ink-bottle effect and differences between receding and advancing capillary angles. Hence the void volume available for air flow is larger than it was during the drying portion of the test, requiring lesser

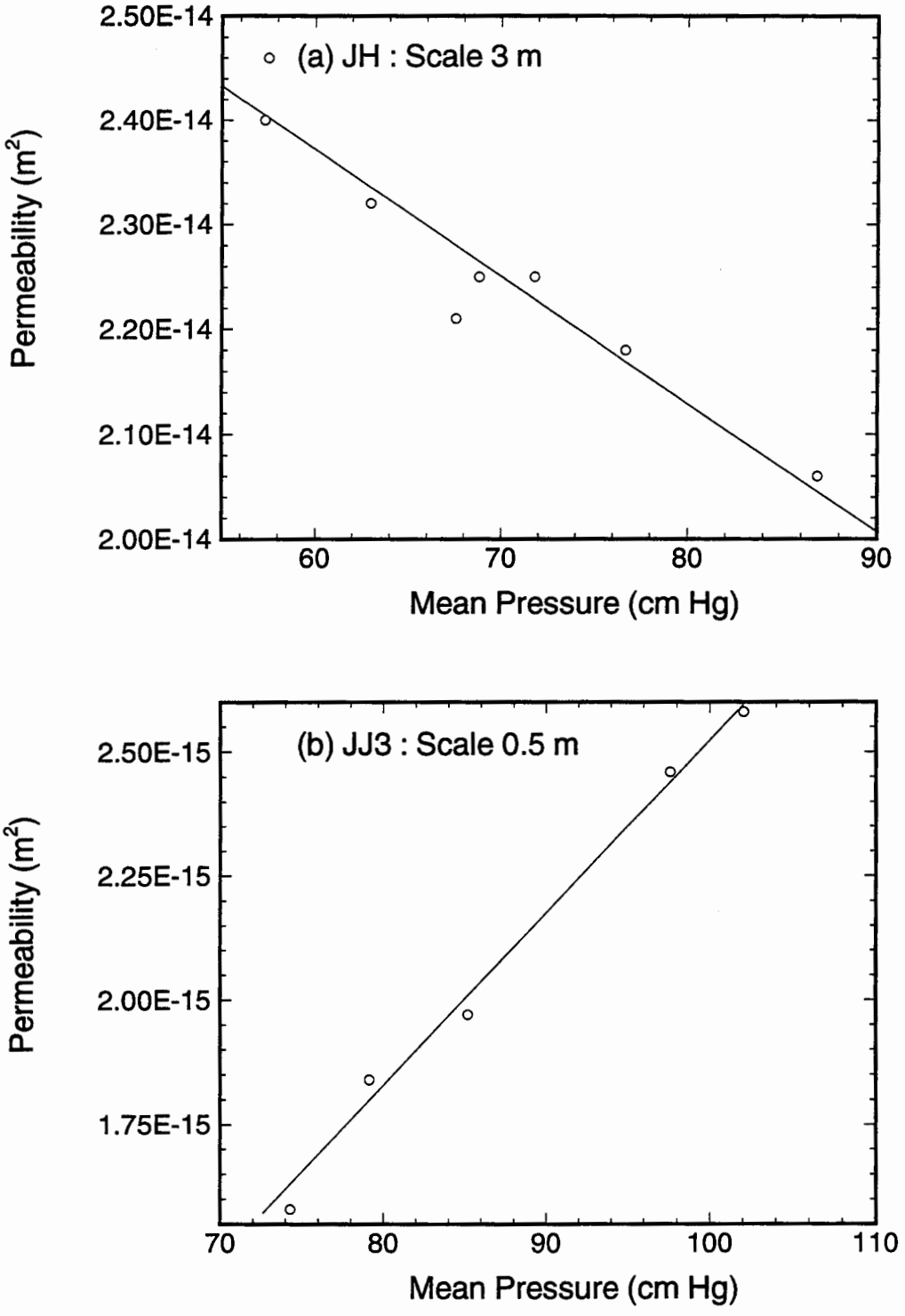

Figure 6.4: Changes of apparent permeability as a function of pressure.
(a) Inertial flow effects. (b) Two-phase flow effects.

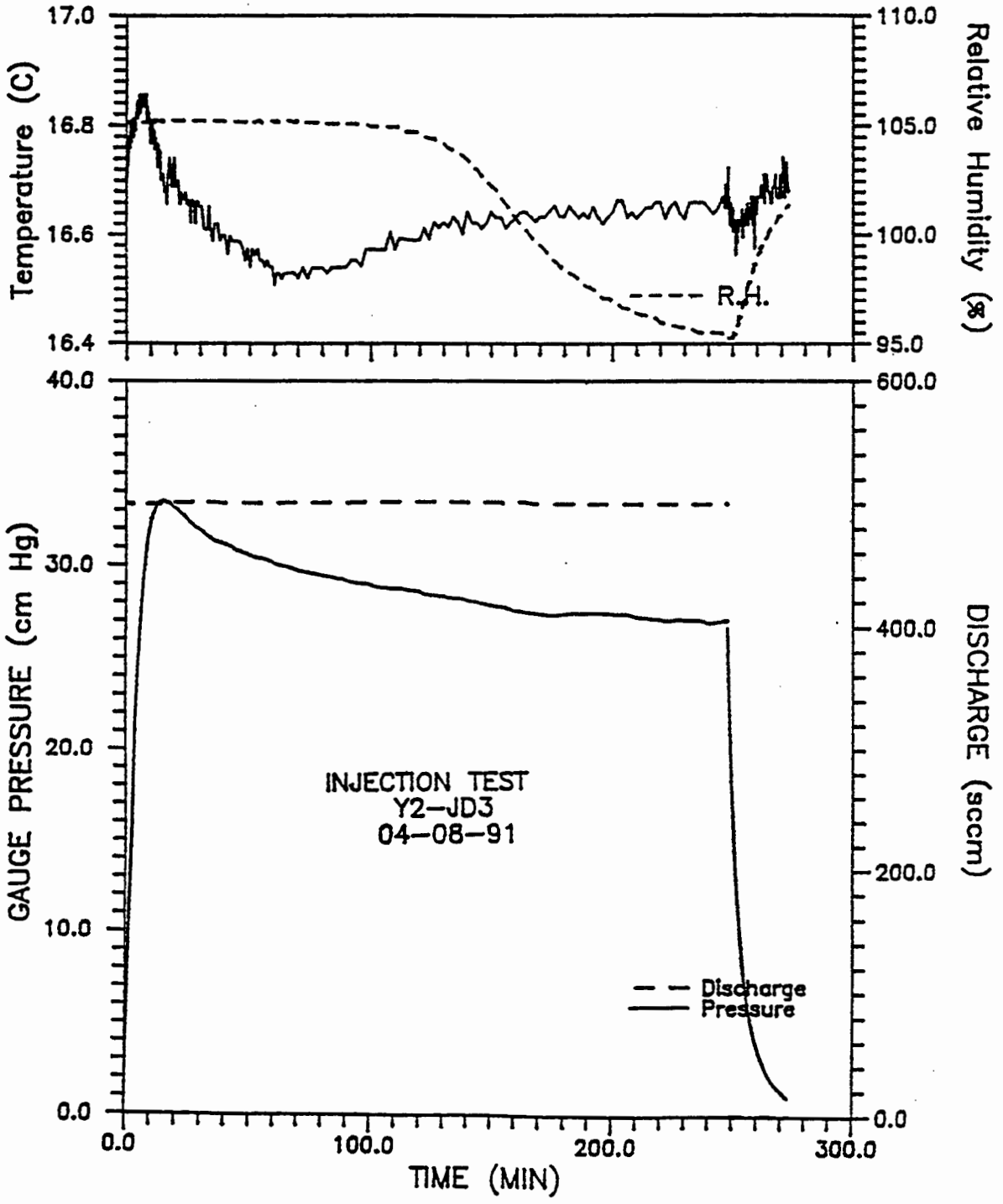

Figure 6.5: Non-monotonic change of pressure response during an air injection pressure test.

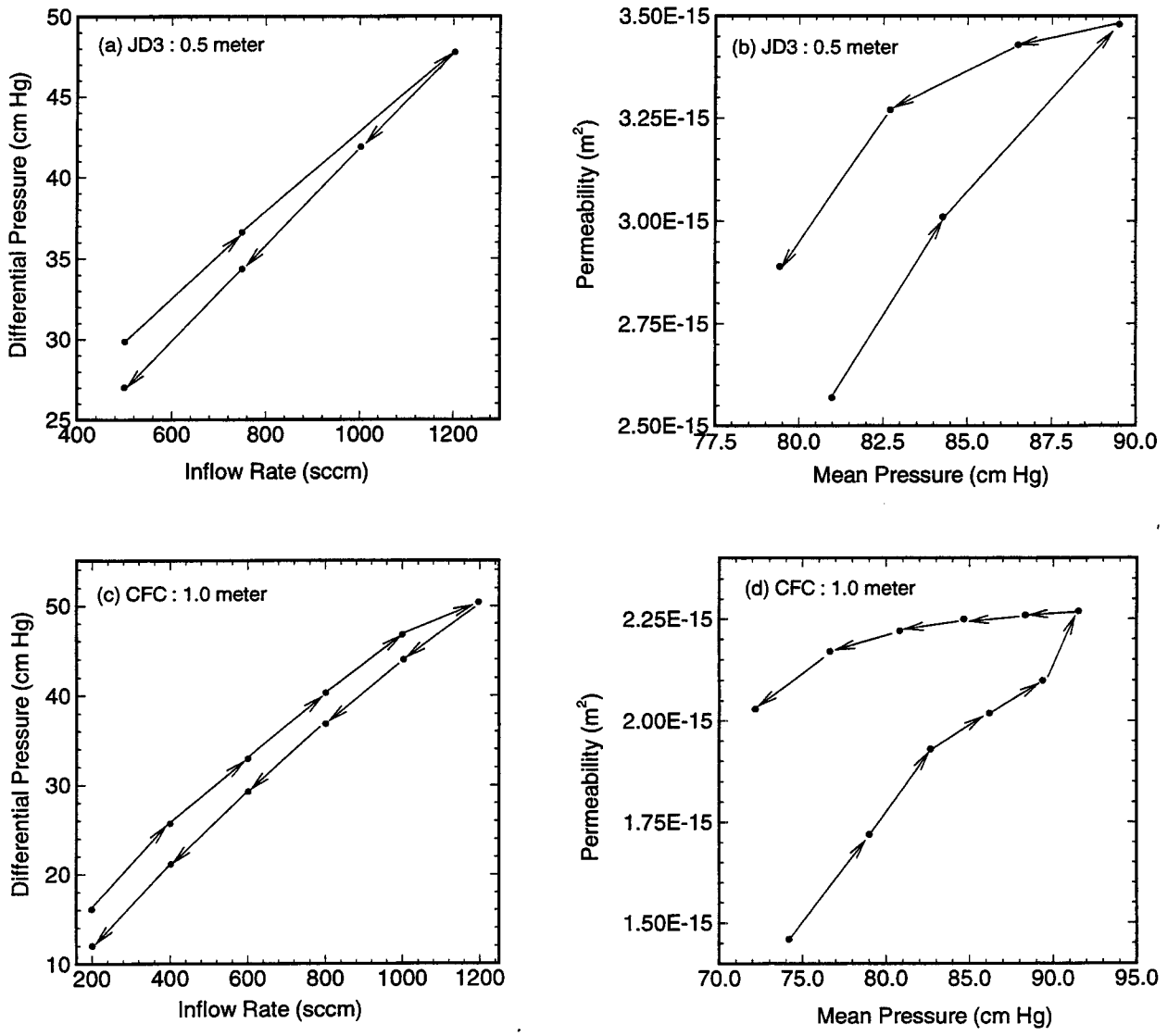

Figure 6.6: Hysteretic behavior of apparent permeability as a function of injection rate.

pressure to maintain a given flow rate, and resulting in a larger apparent permeability. Similar behavior is depicted by retention curves where drainage and imbibition data are available [Rhodes, 1993, see also Fig. 2.3].

The second type of test was designed to span as large a pressure and permeability range as allowed by the field equipment, aiming to determine the critical air entry pressure at which water movement (drainage) starts to occur. Pressure responses for two of these tests are depicted in Figure 6.7. As shown in this figure, the tests consisted of twelve flow rates in 1-m injection intervals along boreholes Z2 and W2A. The pressure stabilizes "rapidly" (within 100 to 200 minutes) at low flow rates, but takes significantly longer to stabilize at higher flow rates. Whereas, at small injection rates the pressure increases monotonically toward a stable value, at larger flow rates the pressure first increases to a maximum and then decreases monotonically to a steady value. Based on calculated changes of permeability, it appears that drainage occurs at all pressure levels but resistance to drainage varies in a nonlinear fashion, frustrating our attempts to establish a unique air entry value for a given borehole interval. Numerical simulations [Guzman, 1994] closely reproduce the observed two-phase behavior supporting our contention that the observed permeability changes are the result of capillary displacement of water by air.

Minimum and maximum permeability values in Table 6.1 correspond to those obtained during multiple injection rates and repeated testing. In general, apparent air permeability increases with increasing pressure (injection rate), but, there are some "high-permeability" intervals for which it decreases with increasing pressure (injection rate). We attribute this decrease in permeability to inertial flow effects resulting from high pore flow velocities [Guzman, 1994]. Due to the pressure dependence of measured permeability, sample statistics are reported for mid-range permeability values (average of minimum and maximum k) for each interval. Table 6.2 includes the corresponding sample statistics for all available data.

TABLE 6.2
Summary of steady state permeabilities.

Borehole ID	Scale of Measurement (m)	Number of Samples	k (m^2)			$ln\ k$		
			Mean (10^{-15})	Median (10^{-15})	Variance (10^{-30})	Mean	Median	Variance
Y2	0.5	54	3.01	0.85	110.2	-34.76	-34.71	2.25
	1.0	28	5.00	1.38	147.9	-34.47	-34.22	3.07
	3.0	9	4.33	1.07	60.4	-34.03	-34.47	2.00
X2	1.0	30	4.95	1.08	266.9	-34.83	-34.52	2.93
Z2	1.0	28	8.38	0.86	313.5	-34.51	-35.16	4.96
W2A	1.0	31	1.73	0.74	5.0	-34.84	-35.05	1.37
V2	1.0	21	2.12	0.11	55.8	-36.28	-36.74	3.78
Y3	1.0	23	6.06	1.68	109.7	-34.47	-34.36	5.50
All	1.0	161	4.72	0.87	154.5	-34.85	-34.90	3.71

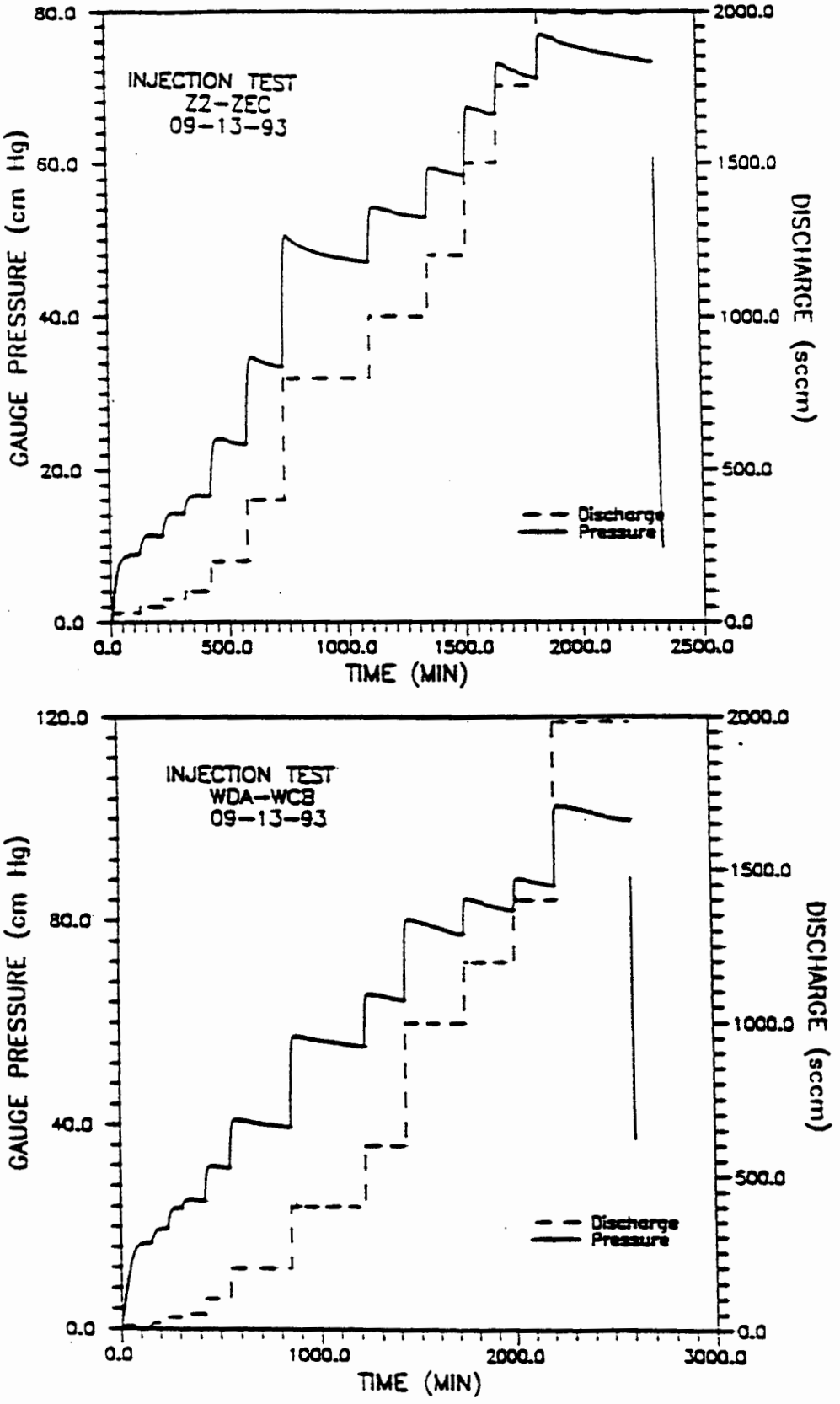

Figure 6.7: Pressure response during a multi-step injection test.

6.4 Scale Dependence

A basic assumption behind the concept of flow and transport through porous media is that the partial differential equations used to describe these processes apply on some macroscopic scale. The precise magnitude of this scale is rarely, if ever, specified or mentioned. Though the dependence of permeability on the scale of measurement is often recognized, evidence for such scale dependence is usually circumstantial. Studies by Cushman [1984] and Desbarats and Bachu [1994] underline the need for additional research on the effect of measurement support on the spatial statistics of environmental data.

Our systematic measurement of k at ALTS on three different scales (measurement supports) provides a unique opportunity to observe the variation of permeability with such scale. Table 6.2 shows that the arithmetic mean of k increases from 3.01×10^{-15} m^2 at the 0.5-m scale to 5.0×10^{-15} m^2 at the 1.0-m scale, and then drops somewhat at the 3.0-m scale for borehole Y2. As the flow is predominantly radial in all three cases, one would expect the arithmetic averages to be independent of measurement support. We attribute the increase in mean k from 0.5- to 1.0-m scales partly to sampling error and partly to the nested semivariogram structure observed in borehole Y2; a theoretical explanation of this phenomenon can be found in a recent paper by Neuman [1994]. This author indicates that when the log permeability behaves as a multi-scale random process (see Section 6.6) the effective permeability varies as a power of the measurement scale. We believe that the subsequent drop in mean k from 1.0 m to 3.0 m scales is an artifact of the small sample at the 3.0 m scale; theoretically we expect mean k to either stabilize or to continue increasing with the length of the support. The sample size decreases from 54 at 0.5 m to 28 at 1.0 m to 9 at 3.0 m test intervals.

Theoretically, the variance of k should decrease as the support length increases. Instead, it increases from 0.5 to 1.0 m scales, then decreases. A similar increase in variance is reported by Desbarats and Bachu [1994] when comparing core-scale permeability data to those obtained from drill-stem test measurements. However, we again suspect that part of this is due to the small size of our data sets, especially at the 1.0 and 3.0 m scales in borehole Y2.

Existing stochastic theories of flow and transport in heterogeneous media rely heavily on a knowledge of the mean and variance of log permeabilities. It is clear from our data that both the mean and the variance of ln k may vary with the scale of measurement in a way which may or may not be theoretically predictable by these theories. This emphasizes the need to perform site characterization on a wide range of well-defined scales of measurements, both in terms of support (size of rock sample tested) and in terms of correlation distanced between supports to reveal semivariogram structures such as the nested forms discussed in the next section.

To study further the relationship between our measurements at different scales, and to verify further that flow in our tests is predominantly radial, we computed spatial weighted averages of the 0.5- and 1.0-meter permeability data over test intervals of 1.0 and 3.0 m. We then compared these local spatial averages, arithmetic and geometric, with k values actually measured at the 1.0 and 3.0-m scales. The actual distance between the straddle-packers corresponding to the "1.0-meter scale" was 0.98 m. Weighting was performed according to:

$$k_a = \sum_{i=1}^{n} \frac{l_i}{L} k_i \quad \text{and} \quad k_g = \prod_{i=1}^{n} (k_i)^{l_i/L} \quad \text{where} \quad L = \sum_{i=1}^{n} l_i \tag{6.3}$$

l_i being the portion of the particular interval completely contained within a larger interval L, k_a and k_g being the arithmetic and geometric averages, respectively. Three upscaled estimates were obtained in this way; 3-meter values based on 0.5- and 1.0-meter data, and 1-meter values based on 0.5-meter data. We found that arithmetic averages provide better estimates than geometric averages, the latter generally underestimating the measured values. Both averages underpredict the measurements at high permeabilities, but the arithmetic averages do so to a lesser extent than do the geometric means. The

fact that the arithmetic averages produce better estimates supports our earlier contention that flow during the straddle-packer injection tests at ALTS is predominantly radial.

6.5 Spatial Variability and Statistical Analysis

The spatial variability of apparent air permeability measured at three different scales is shown in Figures 6.8 to 6.10. The data are presented in the form of rectangles which delineate depth intervals and ranges of computed permeabilities. Also shown are the minimum (dashed curve) and maximum (solid curve) pressures applied during each test. In general, there is no indication of a systematic trend as a function of depth. However, a pseudo-periodic behavior becomes more prominent as the scale of measurement is reduced. Even for data at the 0.5-m scale, there does not seem to be a direct correlation between fracture occurrence and permeability in borehole Y2 though high permeabilities are expected to be associated with some degree of fracturing. We conclude that a visual identification of open fractures is a poor predictor of permeability, which must therefore be measured directly by means of pneumatic (or hydraulic) tests.

Boreholes X2, Z2, W2A, and V2 have been completely tested at a scale of 1 meter while testing in borehole Y3 is underway. Permeabilities as function of pressure and position along these boreholes are shown in Figures 6.11 through 6.15, respectively. Again a poor correlation is found between fracture traces and the permeability estimates in boreholes X2, Z2 and Y3. Permeability estimates along borehole W2A, vary with pressure over wider ranges than do those in the other boreholes. These larger changes may be the result of either the effect of the plastic cover on the natural distribution of moisture along the rock profile (around boreholes X2, Y2, Z2, V2 and Y3) or the spatial variability of the fluid retention properties of the rock. We believe that the effect of the plastic cover, rather than spatial variation in rock properties, is responsible for the observed changes. The effect of seasonal variability on moisture distribution, and in turn on apparent "in-situ"permeability, needs to be studied further.

The statistics of log-transformed permeability estimates (ln k) in different boreholes and the corresponding histograms are summarized in Figures 6.16 to 6.18. These statistics correspond to the mid-range log-transformed permeability, $(\ln k_{max} + \ln k_{min})/2$. The statistics of the complete (composite) data set including permeabilities from four directions (Figure 6.16a) show that the resulting histogram is relatively symmetric (skewness = 0.153), with the mean close to the median, and a flat distribution (kurtosis = -0.142) [Hann, 1977]. Histograms for the particular directions and boreholes are not as well defined as the composite histogram, due to the smaller size of these samples.

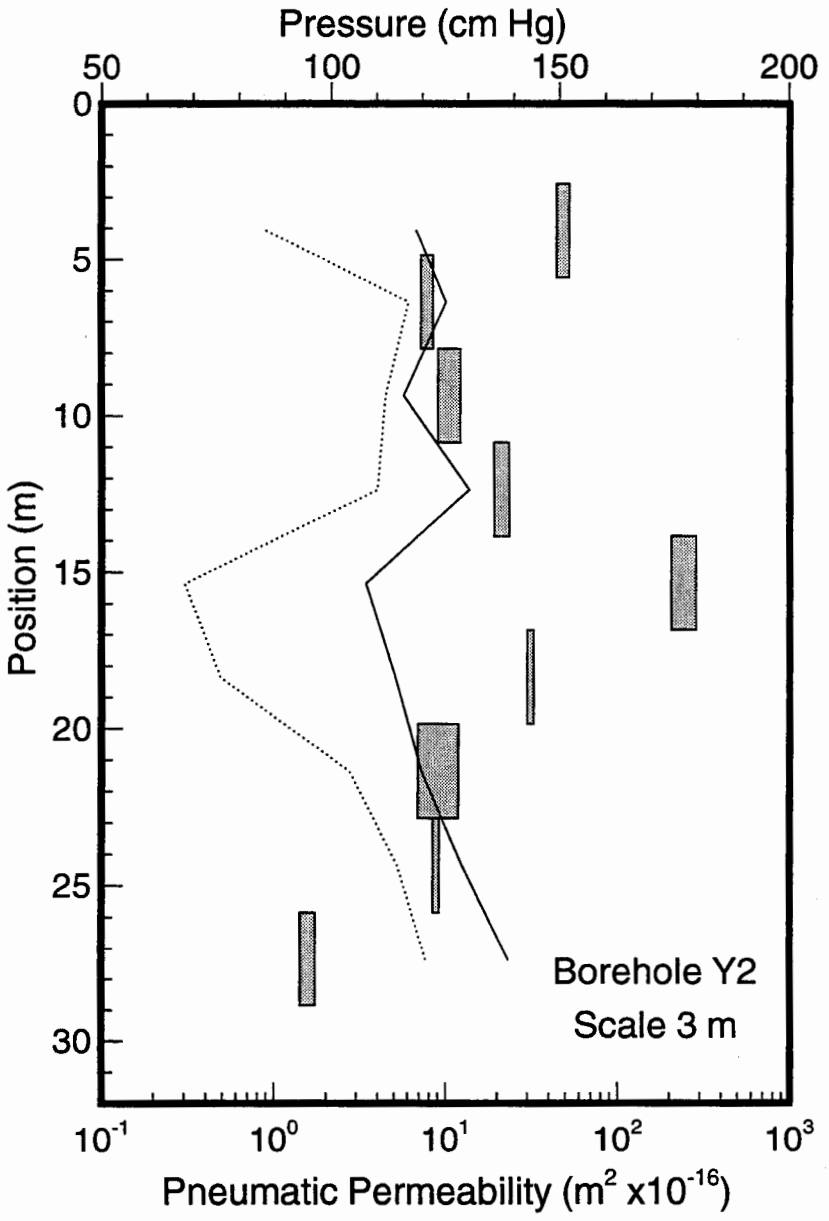

Figure 6.8: Spatial distribution of apparent permeability along Borehole Y2 at a scale of 3.0 m.

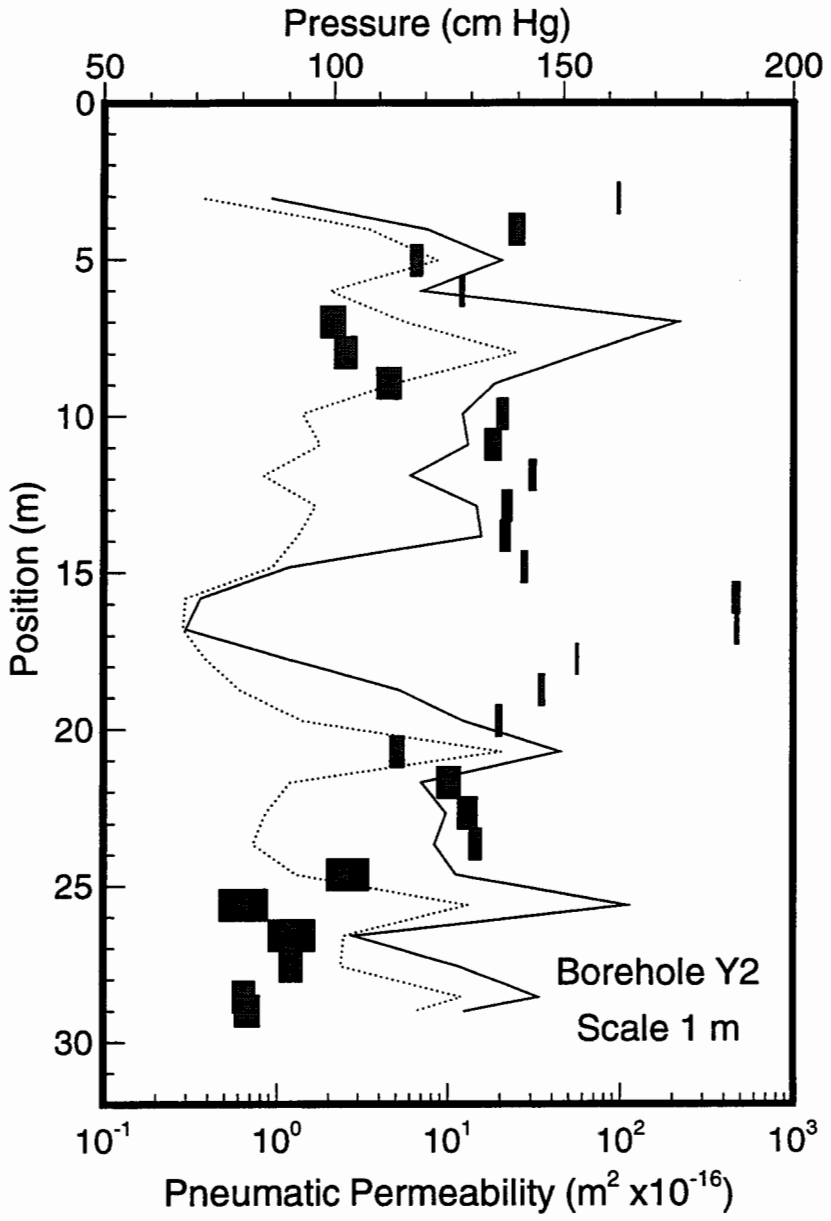

Figure 6.9: Spatial distribution of apparent permeability along Borehole Y2 at a scale of 1.0 m.

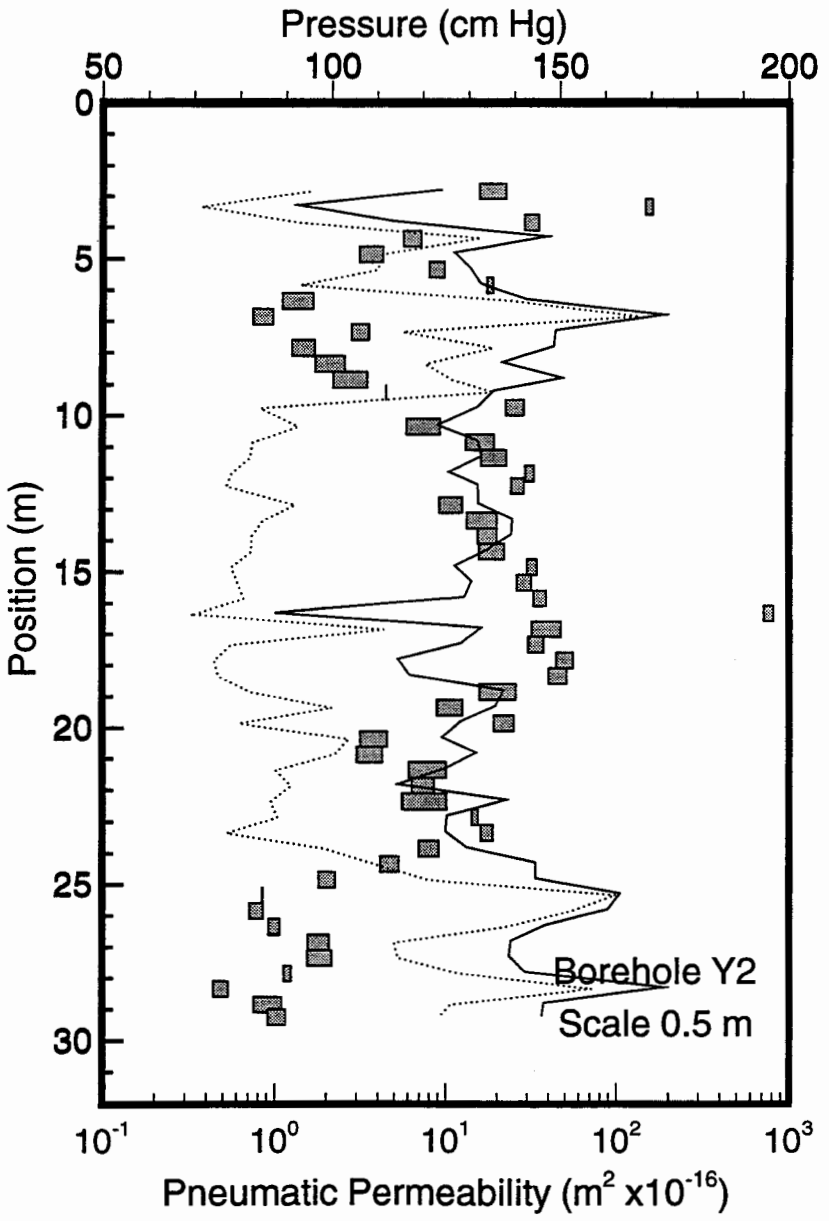

Figure 6.10: Spatial distribution of apparent permeability along Borehole Y2 at a scale of 0.5 m.

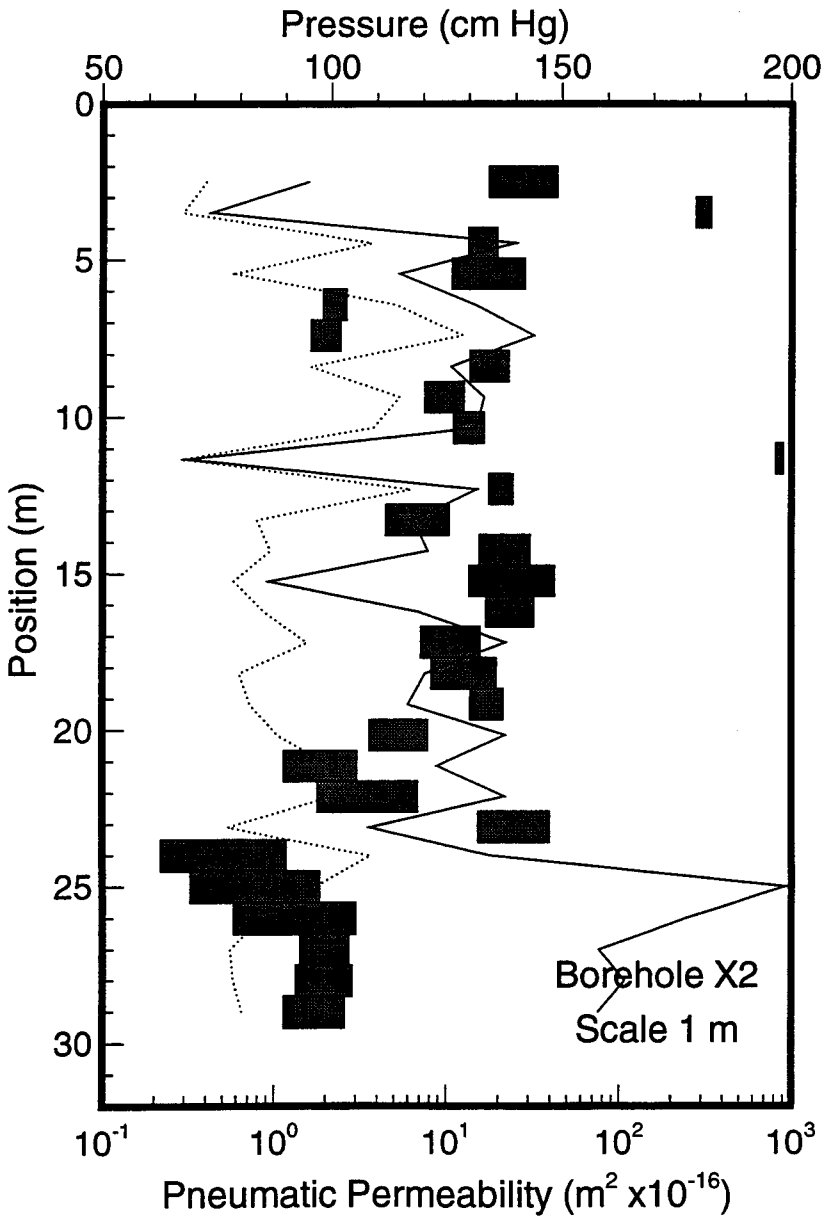

Figure 6.11: Spatial distribution of apparent permeability along Borehole X2 at a scale of 1.0 m.

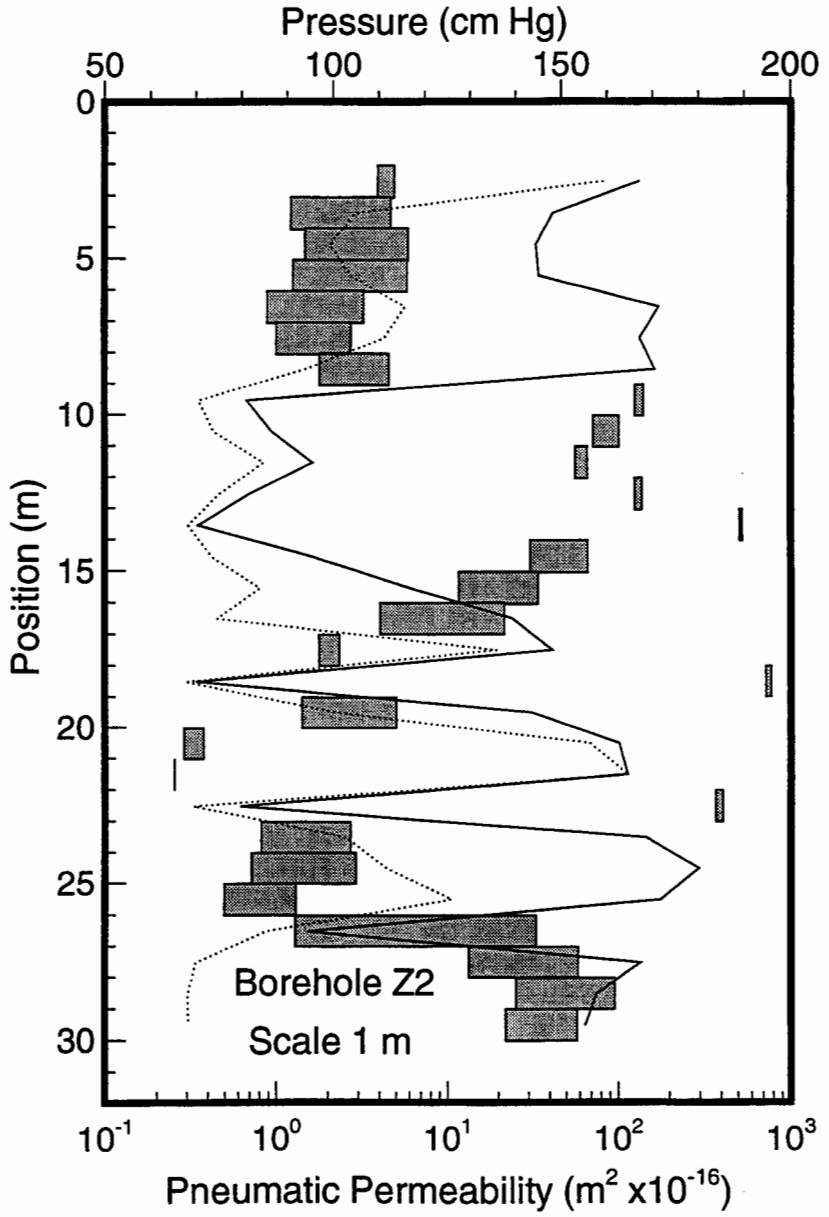

Figure 6.12: Spatial distribution of apparent permeability along Borehole Z2 at a scale of 1.0 m.

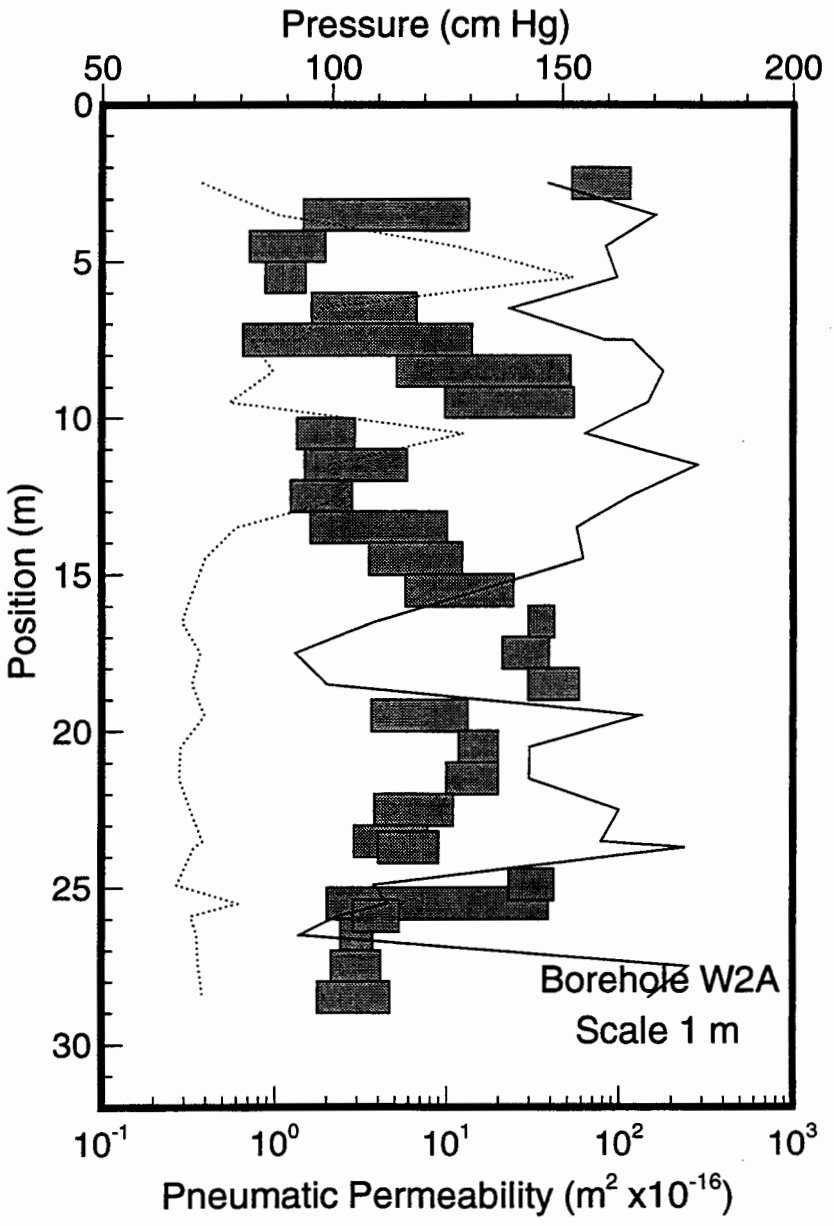

Figure 6.13: Spatial distribution of apparent permeability along Borehole W2A at a scale of 1.0 m.

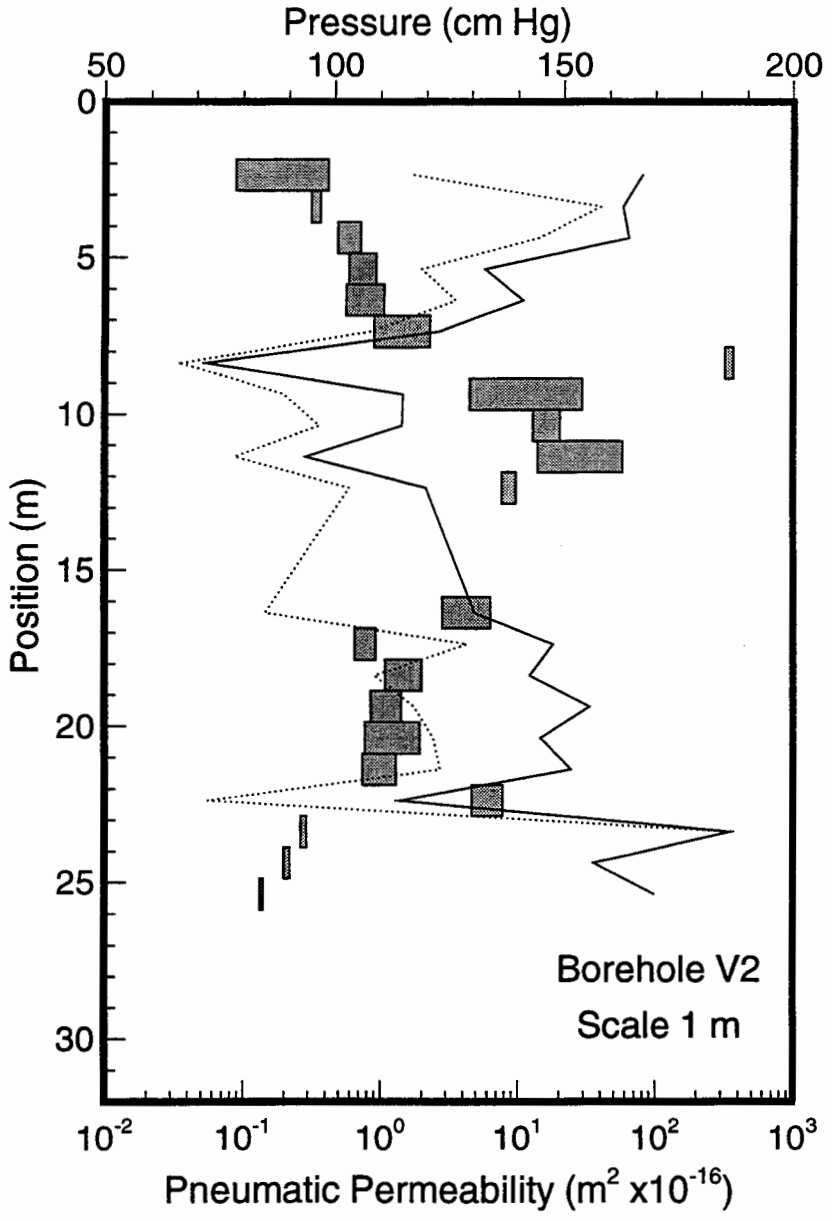

Figure 6.14: Spatial distribution of apparent permeability along Borehole V2 at a scale of 1.0 m.

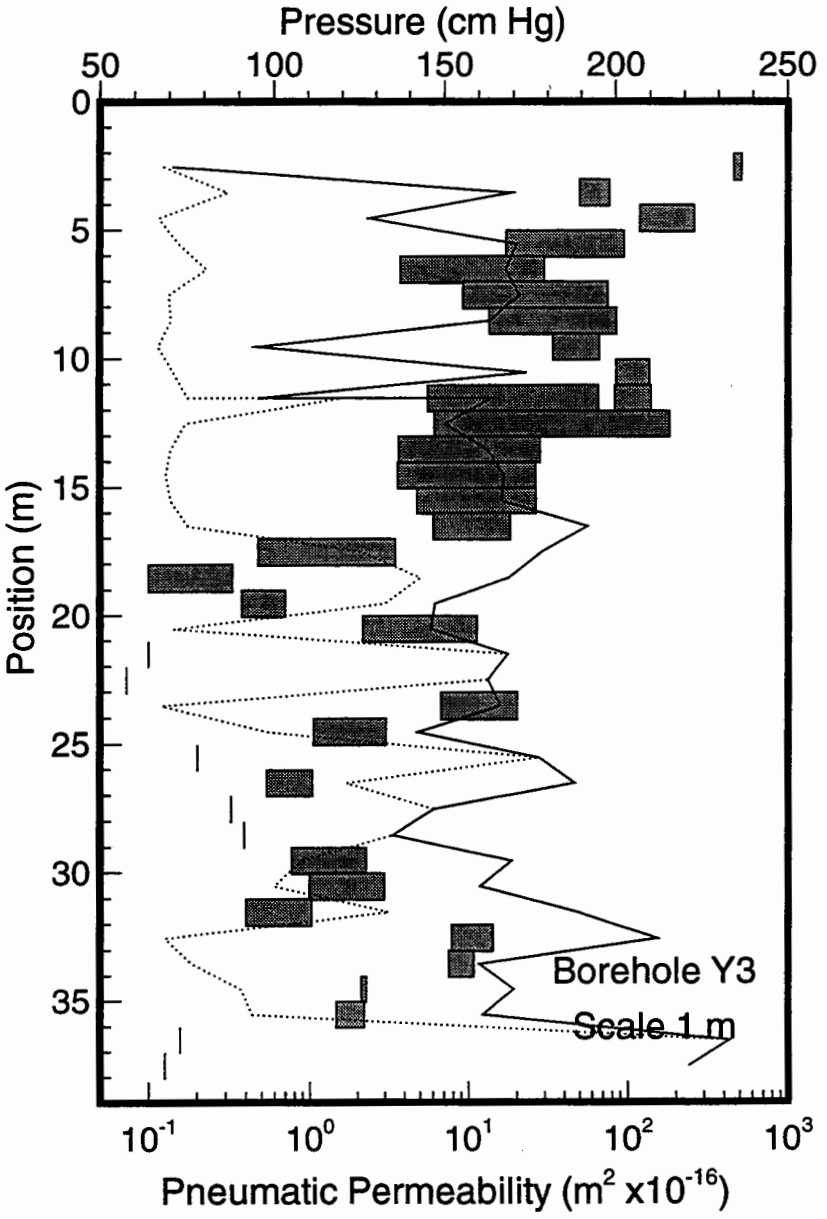

Figure 6.15: Spatial distribution of apparent permeability along Borehole Y3 at a scale of 1.0 m.

All Boreholes

Mean	-34.8518
Standard Error	0.1518
Median	-34.9030
Mode	-35.7850
Standard Deviation	1.9261
Variance	3.7098
Kurtosis	-0.1416
Skewness	0.1533
Range	9.3570
Minimum	-39.4380
Maximum	-30.0810
Sum	-5611.1402
Count	161.0000
Confidence Level(0.950000)	0.2975

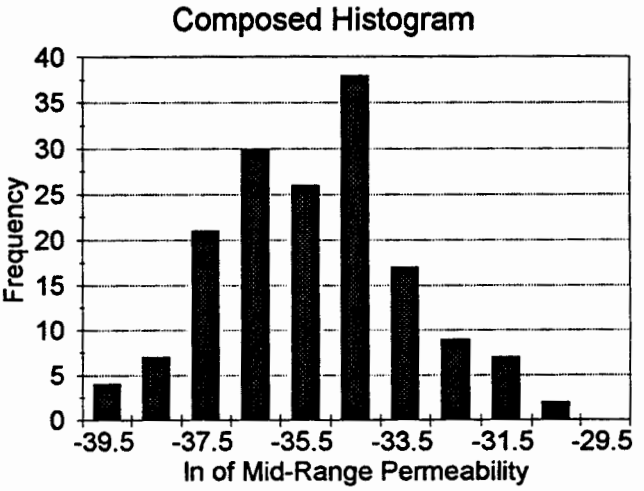

Boreholes Y2, X2 & Y3

Mean	-34.6021
Standard Error	0.2123
Median	-34.3536
Mode	NA
Standard Deviation	1.9103
Variance	3.6491
Kurtosis	0.1687
Skewness	-0.1084
Range	9.3570
Minimum	-39.4380
Maximum	-30.0810
Sum	-2802.7726
Count	81.0000
Confidence Level(0.950000)	0.4160

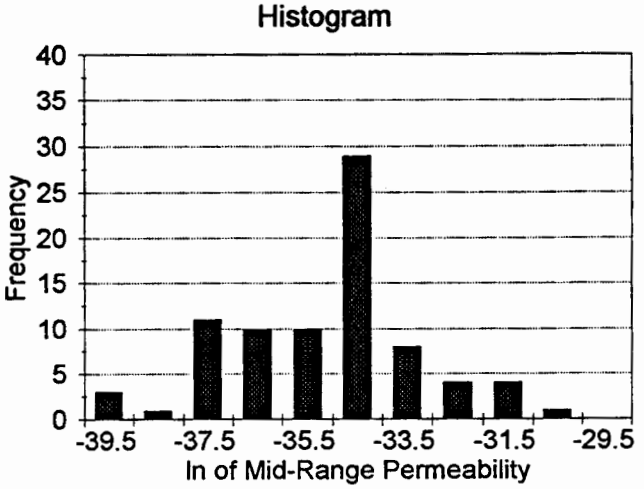

Figure 6.16: Summary statistics:
(a) Composite apparent permeability at 1-m scale, (b) Azimuth west, dip 45°

Borehole Z2

Mean	-34.5124
Standard Error	0.4209
Median	-35.1605
Mode	NA
Standard Deviation	2.2274
Variance	4.9615
Kurtosis	-0.8747
Skewness	0.3442
Range	7.9920
Minimum	-38.2130
Maximum	-30.2210
Sum	-966.3470
Count	28.0000
Confidence Level(0.950000)	0.8250

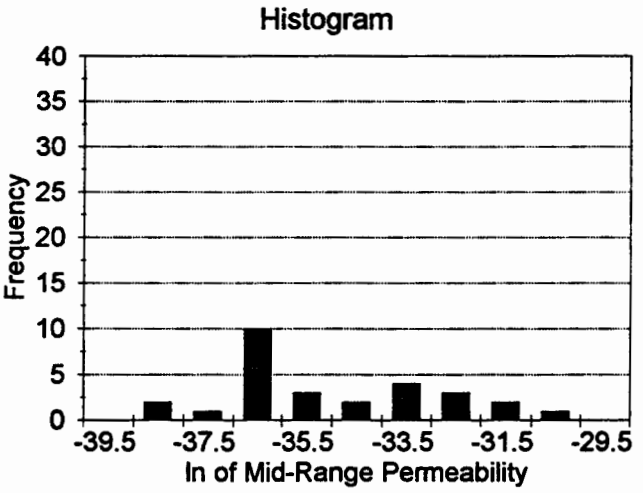

Borehole W2A

Mean	-34.8433
Standard Error	0.2099
Median	-35.0500
Mode	NA
Standard Deviation	1.1689
Variance	1.3662
Kurtosis	-0.5162
Skewness	0.5193
Range	4.3640
Minimum	-36.7040
Maximum	-32.3400
Sum	-1080.1420
Count	31.0000
Confidence Level(0.950000)	0.4115

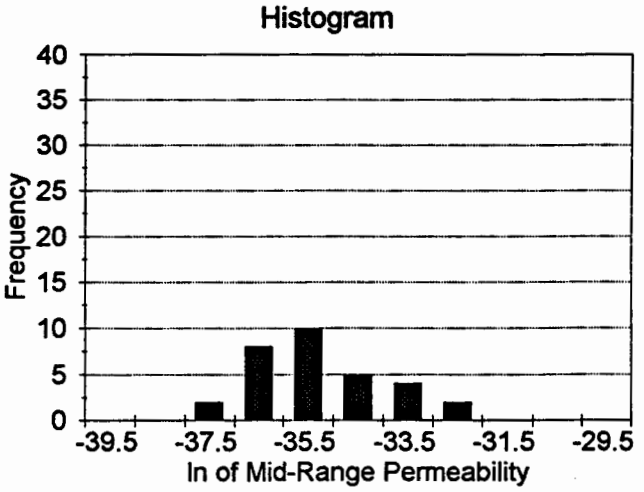

Figure 6.17: Summary statistics: (a) Azimuth east, dip 45°, (b) Azimuth south, dip 45°

Borehole V2

Mean	-36.2799
Standard Error	0.4242
Median	-36.7428
Mode	NA
Standard Deviation	1.9440
Variance	3.7793
Kurtosis	1.2083
Skewness	1.0528
Range	7.8613
Minimum	-38.8619
Maximum	-31.0006
Sum	-761.8786
Count	21.0000
Confidence Level(0.950000)	0.8315

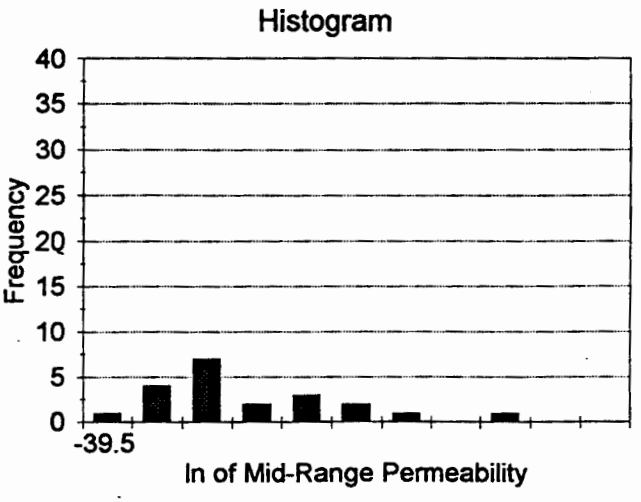

Figure 6.18: Summary statistics: Vertical direction.

6.6 Geostatistical Analysis

To date, more than one hundred and sixty (160) one-meter intervals have been tested along six holes oriented along four different directions at ALTS. These data provide a unique opportunity to study the three-dimensional spatial structure of air permeability. Here we present a brief summary of the geostatistical analyses [Guzman, 1994] together with sample semivariograms of ln k from borehole Y2 at three measurement scales. The geostatistical analysis is performed on the log transformed mid-range permeability data.

A three-dimensional omni-directional semivariogram for the available 1-m scale data is presented in 6.19. Semivariogram values corresponding to lags with less than 40 pairs were deemed unreliable and are not.included in this figure (shading of particular semivariograms values is a function of the number of pairs). This semivariogram shows an echelon structure indicative of a nested hierarchy of processes acting at different scales. The first correlation structure has a sill of 1.2 and a range of about 3.0 m. The second structure shows a sill of 3.8 and a range of about 12.0 m. The sill and range for the third structure remain undefined due to the relatively small size of the sampling domain (40 m x 25 m x 35 m). Possible explanations for these correlation structures are;

1. The lower plateau (or sill) is associated with rock matrix and small discontinuous fractures whereas the higher sill is representative of more conductive better connected fractures prevalent at intermediate scale.
2. Different deposition sequences during the formation of the tuff may result in heterogeneities within the rock mass.
3. A combination of effects from fracture and matrix heterogeneity on the overall physical characteristics of the rock mass.

Multiscale continua behavior has been reported in the soil literature by Burrough [1983], in the petroleum literature by Hewett [1986], and in the hydrologic literature by Grindrod and Impey [1992] and Desbarats and Bachu [1994]. They like others, have associated it with fractal behavior, a concept used by Neuman [1990, 1993, 1994] to explain the scale dependence of dispersivities and hydraulic conductivities. An upcoming paragraph deals with the application of this theory to the available air permeability data from ALTS.

Semivariograms corresponding to 0.5, 1.0, and 3.0 m test intervals in borehole Y2 are shown in Figure 6.20. As there are only nine data points at the 3.0 m scale, this sample semivariogram is relatively ill defined. The semivariograms corresponding to 0.5 m and 1.0 m test intervals reveal well defined structures (Figure 6.20b and c). Both show two distinct plateaus, suggesting (again) the presence of a multiscale (nested) correlation structure. The structure with the lower sill exhibits a correlation scale (range) of about 6.0 m, the other about 11.0 m.

Semivariograms of ln k at 1.0 m scale in the directions W, E, and S at a 45° and 90° dip are shown in Figures 6.21. These semivariograms seem to involve elements of a nested structure and pseudo-periodicity. The nugget component for all our semivariograms is surprisingly small. We tentatively attribute the differences among these directional semivariograms largely to sampling errors (the 1.0 m samples are relatively small).

The observed nested structure in Figures 6.20 and 6.21a is similar to that discussed by Neuman [1990, 1993, 1994] in connection with his scaling theory. According to this theory, the variance (sill) and correlation scale (range) of log permeabilities tend to increase consistently with separation distance. They are associated with a power-law semivariogram:

$$\gamma(s) = c\, s^{2w} \qquad (6.4)$$

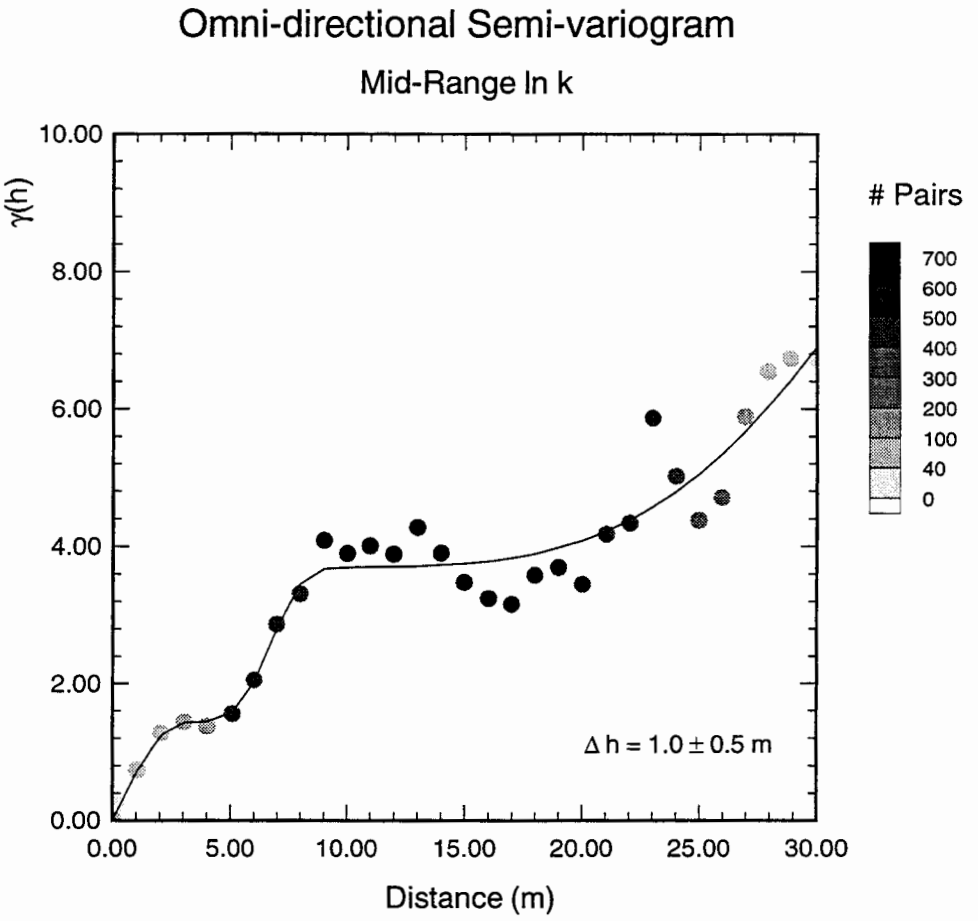

Figure 6.19: Three-dimensional omni-directional semivariogram of *ln k* 1-m scale.

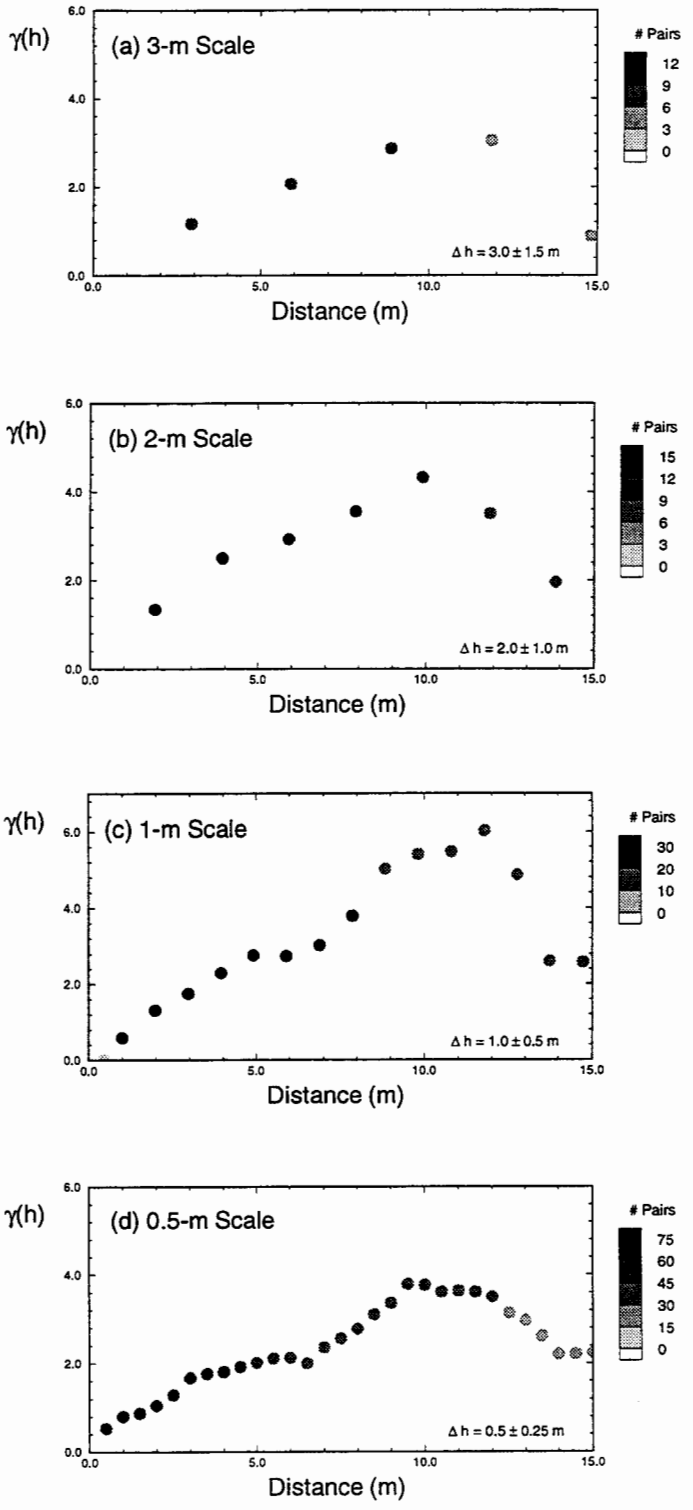

Figure 6.20: Semivariograms of *ln k* along Y2: (a) 3-m scale, (b) 2-m scale, (c) 1-m scale, and (d) 0.5-m scale.

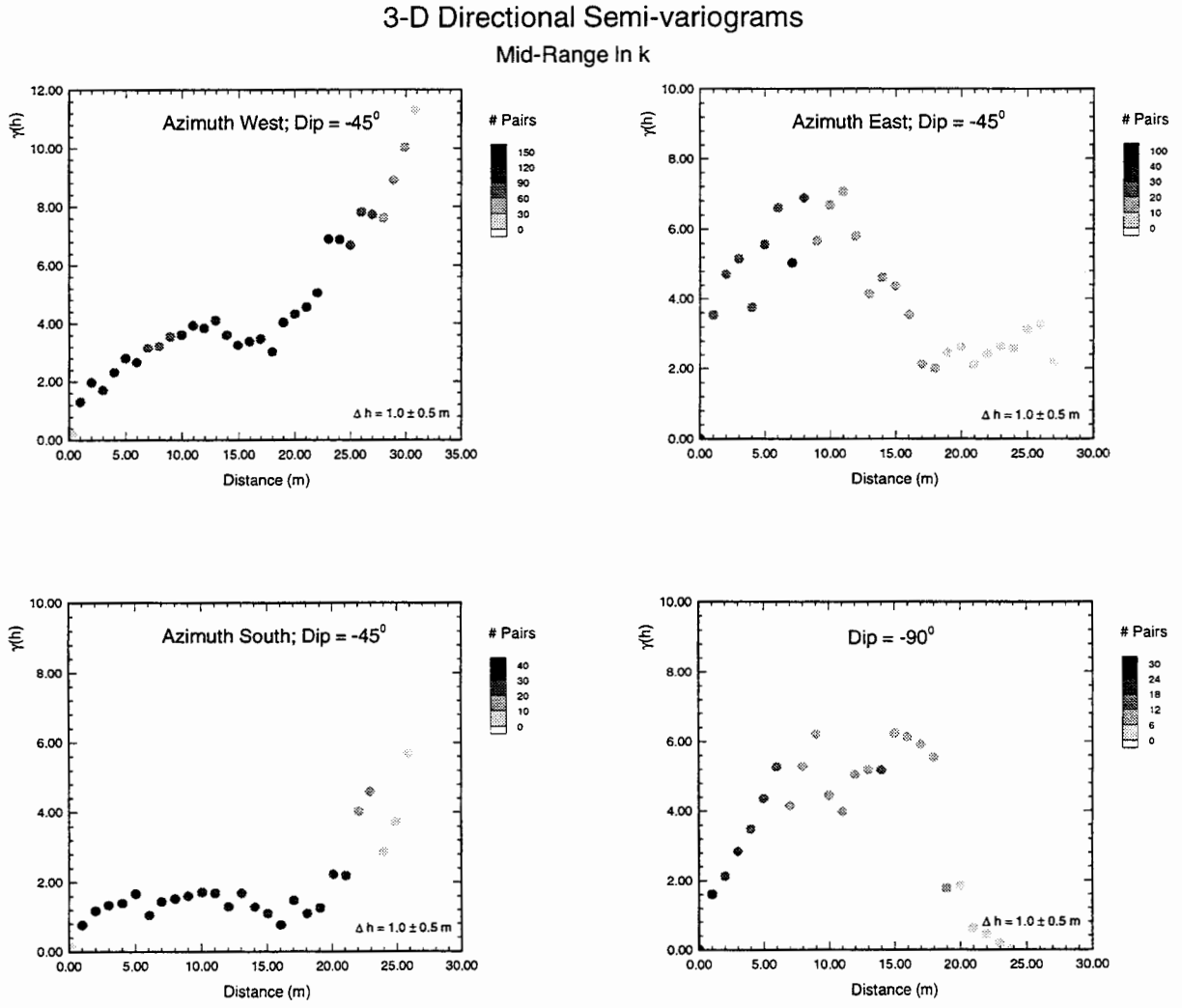

Figure 6.21: Directional semivariograms of *ln k*: (a) Azimuth west, dip 45°, (b) Azimuth east, dip 45°, (c) Azimuth south, dip 45°, (d) Vertical direction.

where

- s separation distance
- c constant
- w Hurst coefficient.

Large values of w (e.g., $w > 0.5$) correspond to smoothly varying log permeability fields whose spatial increments are positively correlated (persistent), $w = 0.5$, to fields with uncorrelated increments (pure Brownian process), $0 < w < 0.5$ to noisy fields with negatively correlated (anti-persistent) increments. Equation 6.4 implies that the log permeability field is self-affine with a fractal dimension $D = E + 1 - w$, where E is the topological dimension. As such, the log permeability field lacks either a finite correlation scale or a finite variance. Neuman [1990, 1993] predicted on the basis of apparent dispersivities from tracer tests, and verified on the basis of permeabilities and transmissivities from hydraulic tests [Neuman, 1994], that the Hurst coefficient w tends toward 0.25 as sample size increases. Whereas the data quoted by Neuman span scales from 0.1 m to 45 km, Desbarats and Bachu [1994] have recently reported $w = 0.22$ for log transmissivities in a sequence of sands and shales for scales up to 100 km.

Figure 6.22 shows a log-log semivariogram of the available three-dimensional data from ALTS at 1 m scale. Also shown, is a power law model fitted to the data by least squares. The latter is a straight line with half slope $w = 0.29$. This is remarkably close to the generalized value of $w = 0.25$ predicted by Neuman. We pool all available air permeability data from ALTS (Figure 6.23) including 54 on the 0.5 m scale, 161 on the 1.0 m scale, and 86 on the 3.0 m scale, we obtain a Hurst coefficient of $w = 0.28$. These semivariograms excludes points with fewer than 40 pairs. The 3-m data set was obtained from Rasmussen et al. [1990].

Whereas the power law does not reproduce details of the nested structures in Figure 6.19, it nevertheless captures the multiscale trend of the data. As pointed out by Neuman [1990, 1993, 1994] deviations around this model are due in part to the fact that log permeability is often not self-similar at the local scale but rather exhibits a nested, echelon structure. Each measurement in such a structure represents some discrete, statistically homogeneous geologic unit or feature. Only when the effect of enough such units and/or features is superimposed does the generalized power reveals itself.

Our semivariograms for apparent air permeability at ALTS are similar to those typically obtained in many heterogeneous porous media. This suggests to us that the air permeability data from ALTS behave, for all practical purposes, as if they represented a multiscale continuum. A continuum representation has been found adequate for log permeabilities from various other fractured rock sites including granites at Oracle, Arizona, Stripa and Finnsjon in Sweden and Fanay-Augeres in France [Neuman, 1987, 1990; Kostner, 1993; Ando, 1994]. This supports an earlier conclusion by Neuman [1987, 1990] that one can often treat the permeability of fractured rocks as a random (stochastic) field defined over a (possibly multiscale) continuum.

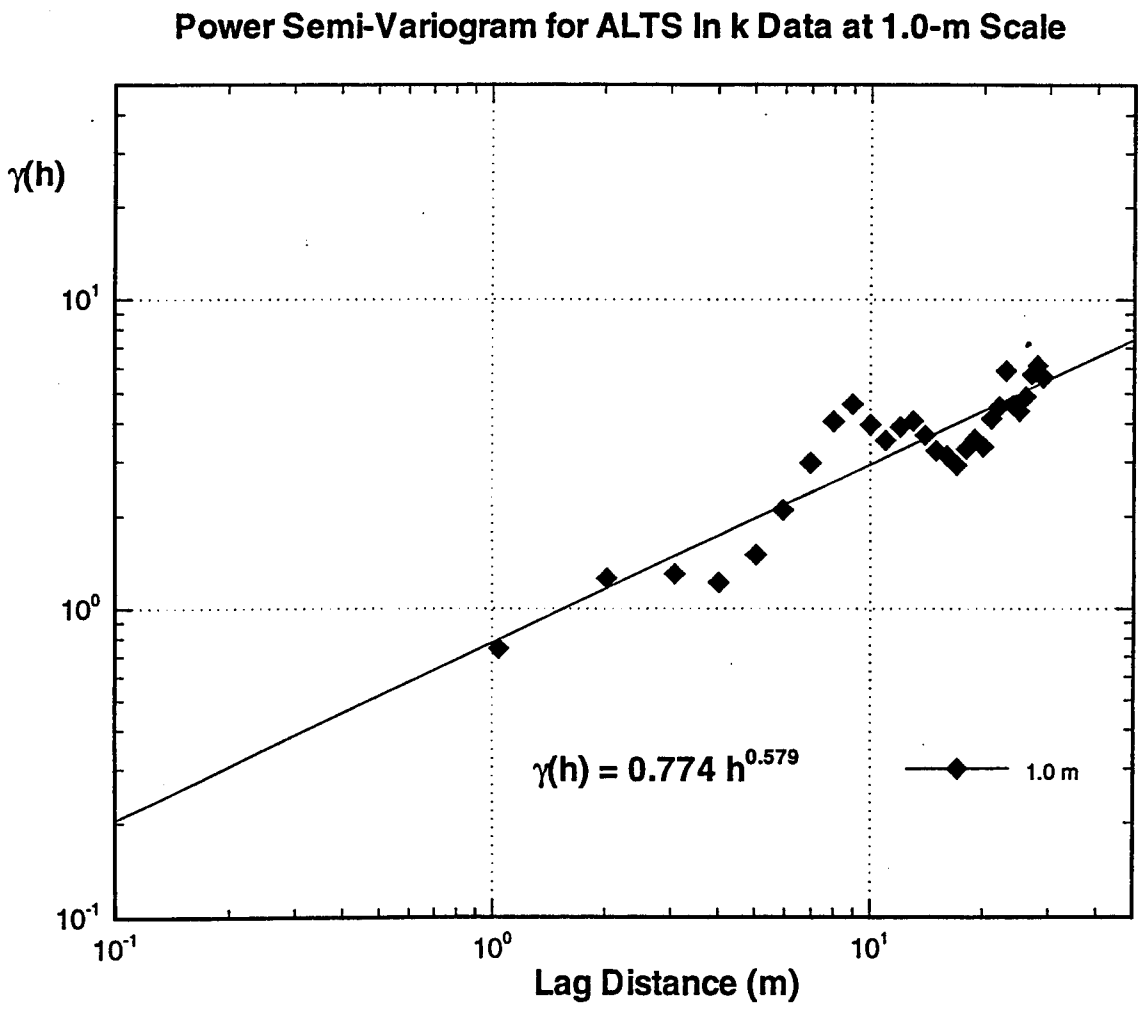

Figure 6.22: Log-Log semivariogram of *ln k* at the 1-m scale.

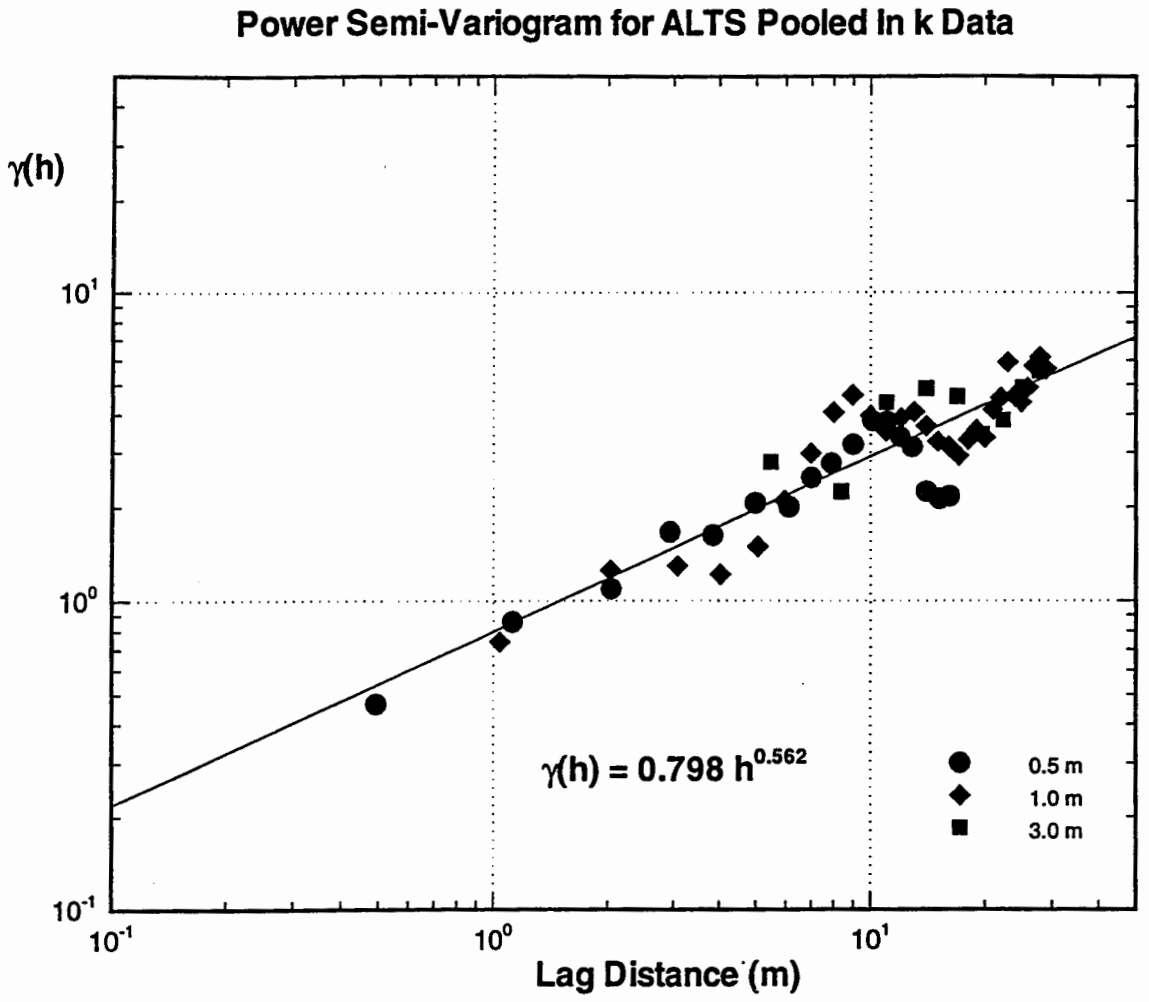

Figure 6.23: Log-Log semivariogram of *ln k* of the pooled data from the 0.5-, 1.0- and 3.0-m scales.

6.7 Discussion

Based on an extensive data set consisting of steady state apparent air permeability values, we have reached the following conclusions. The apparent air permeability from straddle-packer tests is a strong function of the applied pressure. Changes in air permeability with pressure are due to two-phase flow and, in some cases to inertial flow. Computer simulations confirmed the two-phase flow explanation. Upscaling of the apparent permeability is accomplished best via weighted arithmetic averaging.

Geostatistical and statistical analyses indicate that the apparent permeability data from ALTS behave as a stochastic multiscale continuum with an echelon and power-law (fractal) structure. The latter is associated with a Hurst coefficient $w = 0.28$ to 0.29 which is remarkably close to the generalized value $w = 0.25$ predicted by Neuman [1990, 1994]. Additional permeability tests spanning larger rock volumes at ALTS would help to determine whether the seemingly fractal behavior extends beyond the scales already tested.

Our results strongly suggest that site characterizations must be based on hydrogeologic data collected on a spectrum of scales relevant to performance assessment. They further point out the need to consider two-phase flow and inertia effects in the interpretation of air injection tests. The transient part of these tests may hold the key to site evaluation of functional relationships between rock permeability, fluid pressure and saturation. We believe the inverse methods hold a promise in this regard, and propose to use them in the context of our ALTS data.

REFERENCES

Anderson, W.G., 1987, "Wettability Literature Survey-Part 5: The Effect of Wettability on Relative Permeability", *J. Petroleum Technology*, 1453-1468.

Ashworth, E. and T. Ashworth, 1990, A rapid method for measuring thermal conductivity of rock core and its preliminary use for finding the thermal resistance of cracks, in Rock Mechanics: Contributions and Challenges, Hustrum and Johnson (eds), Balkema, Rotterdam.

Barker, J.A., 1988, "A Generalized Radial Flow Model for Hydraulic Tests in Fracture Rock", *Water Resour. Res.*, 24(10):1796-1804.

Bassett, R.L., S.P. Neuman, T.C. Rasmussen, A. Guzman-G., G.R. Davidson, and C.F. Lohrstorfer, 1994, Validation Studies for Assessing Flow and Transport Through Unsaturated Fractured Rock, NUREG/CR-6203, U.S. Nuclear Regulatory Comm., Washington, D.C.

Burrough, P.A., 1983, "Multiscale Sources of Spatial Variation in Soil. I. The Application of Fractal Concepts to Nested Levels of Soil Variation", *J. of Soil Science*, 34:577-597.

Campbell, G.S. and G.W. Gee, 1986. "Water Potential: Miscellaneous Methods", p. 619-633. In A. Klute (ed.) Methods of Soil Analysis, Part I. 2nd ed. Agron. Monogr. 9. ASA and SSSA, Madison, WI.

Carslaw, H.S. and J.C. Jaeger, 1959, Conduction of Heat in Solids, Oxford Press, p. 100.

Dverstorp, B., J. Andersson, and W. Nordqvist, 1992, "Discrete Fracture Network Interpretation of Field Tracer Migration in Sparsely Fractured Rock", *Water Resour. Res.*, 28(9):2327-2343.

Cushman, J.H., 1986, "On Measurement, Scale and Scaling", *Water Resour. Res.*, 22(2):129-134.

Desbarats, A.J. and Bachu, S., 1994, "Geostatistical Analysis of Aquifer Heterogeneity from the Core Scale to the Basin Scale: A Case Study", *Water Resour. Res.*, 30(3):673-684.

Estes, R.K. and P.F. Fulton, 1956, "Gas slippage and permeability measurements", *Trans. Am. Inst. Min. Metall. Pet. Eng.*, 207:338-342.

Finsterle, S. and K. Pruess, Estimating Two-Phase Hydraulic Properties by Inverse Modeling, paper presented at the Fifth International High Level Radioactive Waste Management Conference, Las Vegas, NV. May 22-26, 1994.

Gerke, H.H. and M.T. Van Genuchten, 1993, "A Dual-Porosity Model for Simulating the Preferential Movement of Water and Solutes in Structured Media", *Water Resour. Res.*, 29(2):305-319.

Grindrod, P. and M.D. Impey, 1992, "Fractal Field Simulations of Tracer Migration within the WIPP Culebra Dolomite", Rep. IM2856-1, Version 2, 62 pp., Intera Information Technologies, Denver, Colorado, March.

Guzman-G., A., 1994, Air Permeability Tests and their Interpretation in Partially Saturated Fracture Tuffs, Unpublished Ph.D. Dissertation unpublished manuscript, Department of Hydrology and Water Resources, University of Arizona, Tucson.

Hann, C.T., 1977, Statistical Methods in Hydrology, Iowa State University Press.

Hassler, G.L., et al., 1974, *Trans. AIME*, 118(116):1936 in Scheidegger, A.E.

Hewett, T.A., 1986, "Fractal Distributions of Reservoir Heterogeneity and Their Influence on Fluid Transport", Paper 15386 presented at the 61st Annual Technical Conference, Soc. Pet. Eng., New Orleans, LA, Oct. 5-8.

Hsieh. P.A., S.P. Neuman and E.S. Simpson, 1983, Pressure testing of fractured rocks: a methodology employing three-dimensional cross-hole tests. U. S. Nuclear Regulatory Commission, NUREG/CR-3213.

Hvorslev, M.J., 1951, Time lag and soil permeability in groundwater observations, Bulletin 36, U. S. Army Engineer Water Ways Experiment Station, Vicksburg, Miss.

Klinkenberg, L.J., 1941, The Permeability of Porous Media to Liquids and Gases, Am. Pet. Inst., Drilling and Production Practice.

Klute, A., 1964, "Water Diffusivity", in Methods of Soil Analysis, Part 1, Am. Soc. Agron., Soil Sci. Soc. Am., 262:272.

Klute, A., 1986, "Water Retention: Laboratory Methods", p. 635-662. In A. Klute (ed.) Methods of Soil Analysis, Part I. 2nd ed. Agron. Monogr. 9. ASA and SSSA, Madison, WI.

Klute, A., and C. Dirksen, 1986, Hydraulic conductivity and diffusivity: Laboratory methods. p. 687-734. *In* A. Klute (ed.) Methods of Soil Analysis, Part I. 2nd ed. Agron. Monogr. 9. ASA and SSSA, Madison, WI.

Konstner, A., 1993, Geostatistical and Numerical Analysis of Flow in a Crystalline Rocks Mass. Unpublished M.S. Thesis, Department of Hydrology and Water Resources, University of Arizona.

Krishnamoorthy, T.M., R.N. Nair, and T.P. Sarma, 1992, "Migration of Radionuclides from a Granite Repository", *Water Resour. Res.*, 28(7):1927-1934.

Martinez, M.J., R.C. Dykhuizen, and R.R. Eaton, 1992, "The Apparent Conductivity for Steady Unsaturated Flow in Periodically Fractured Porous Media", *Water Resour. Res.*, 28(11):2879-2887.

Mandelbrot, B.B. and Wallis, J.R., 1969a, "Computer Experiments with Fractional Gaussian Noises, Part I. Averages and Variances", *Water Resour. Res.* 5:228-241.

Mandelbrot, B.B. and Wallis, J.R., 1969b, "Some Long-Run Properties of Geophysical Records", *Water Resour. Res.*, 5:321-340.

Massmann, J. and D.F. Farrier, 1992, "Atmospheric Pressures on Gas Transport in the Vadose Zone", *Water Resour. Res.*, 28(3):777-791.

Montazer, P., 1982, Permeability of Unsaturated, Fractured Metamorphic Rocks Near an Underground Opening, Ph.D. Dissertation, Colorado School of Mines.

Neuman, S.P., 1987, "Stochastic Continuum Representation of Fractured Rock Permeability as an Alternative to the REV and Fracture Network Concepts", in Proceedings, Memoirs of the 28th US Symposium on Rock Mechanics, Tucson, Az.

Neuman, S.P., 1990, "Universal Scaling of Hydraulic Conductivities and Dispersivities in Geologic Media", *Water Resour. Res.*, 26(8):1749-1758.

Neuman, S.P., 1993, Comment on "A Critical Review of Data on Field-Scale Dispersion in Aquifers" by L.W. Gelhar, C. Welty, and K.R. Rehdat, *Water Resour. Res.*, 29(6):1863-1865.

Neuman, S.P., 1994, "Generalized Scaling of Permeabilities: Validation and Effect of Support Scale".

Nitao, J.J. and T.A. Buscheck, 1991, "Infiltration of a Liquid Front in an Unsaturated, Fractured Porous Medium", *Water Resour. Res.*, 27(8):2099-2122.

Nordqvist, A.W., Y.W. Tsang, C.F. Tsang, B. Dverstorp, and J. Andersson, 1992, "A Variable Aperture Fracture Network Model for Flow and Transport in Fractured Rock", *Water Resour. Res.*, 28(6):1703-1713.

Norris, A.E., 1990, "Nuclear Waste Isolation in the Unsaturated Zone, Focus '89", *Proc. of Topical Meeting, Am. Nucl. Soc.*, La Grange Park, IL, September 17-21, 1989.

Oldenburg, C.M. and K. Pruess, 1993, "On Numerical Modeling of Capillary Barriers", *Water Resour. Res.*, 29(4):1045-1056.

Philip, J.R. and D.A. Farrell, 1964, "General Solution of the Infiltration-Advance Problem in Irrigation Hydraulics", *J. of Geophys. Res.*, 69(4):621-631.

Rasmussen, T.C. and D.D. Evans, 1989, "Fluid Flow and Solute Transport Modeling Through Three-Dimensional Networks of Variably Saturated Discrete Fractures", U.S. Nuclear Regulatory Comm., Washington, D.C., NUREG/CR-5239.

Rasmussen, T.C. and D.D. Evans, 1992, "Nonisothermal Hydrologic Transport Experimental Plan", NUREG/CR-5880, U.S. Nuclear Regulatory Commission, Washington, D.C.

Rasmussen, T.C., D.D. Evans, P.J. Sheets, and J.H. Blanford, 1990, Unsaturated Fractured Rock Characterization Methods and Data Sets at the Apache Leap Tuff Site, prepared for U.S. Nuclear Regulatory Commission, Dept. of Hydrology and Water Resources, Univ. of Arizona, Tucson, NUREG/CR-5596.

Rhodes, C.R., 1993, Moisture Characteristic Curves for Apache Leap Tuff: Temperature Effects and Hysteresis, Superior Arizona, Unpublished M.S. Thesis, Department of Hydrology and Water Resources, University of Arizona.

Scheidegger, A.E., 1974, The Physics of Flow Trough Porous Media, 3dr. Edition, University of Toronto Press.

Silliman, S.E., 1989, "Interpretation of the Difference Between Aperture Estimates Derived from Hydraulic and Tracer Tests in a Single Fracture", *Water Resour. Res.*, 25(10):2275-2283.

Thoma, S.G., D.P. Gallegos, and D.M. Smith, 1992, "Impact of Fracture Coatings on Fracture/Matrix Flow Interactions in Unsaturated, Porous Media", *Water Resour. Res.*, 28(5):1357-1367.

Thorstenson, D.C. and D.W. Pollock, 1989, Gas Transport in Unsaturated Porous Media: The Adequacy of Fick's Law, Review of Geophysics, 27(1):61-78.

Tsang, Y.W., 1992, "Usage of 'Equivalent Apertures' for Rock Fractures as Derived from Hydraulic and Tracer Tests", *Water Resour. Res.*, 28(5):1451-1455.

Vickers, B.C., 1990, "Aperture Configuration of a Natural Fracture in Welded Tuff", Unpublished M.S. Thesis, Department of Hydrology and Water Resources, The University of Arizona, Tucson, 132 pp.

Weeks, E.P., 1987, "Effect of Topography on Gas Flow in Unsaturated Fractured Rock: Concepts and Observations", in Evans, D.D. and T.J. Nicholson, *Flow and Transport Through Unsaturated Fractured Rock*, AGU Geophysical Monograph 42, Washington, D.C.

Wentworth, C.K., 1944, *Am. J. of Sci.*, 242:478.

NRC FORM 335 (2-89) NRCM 1102, 3201, 3202

U.S. NUCLEAR REGULATORY COMMISSION

BIBLIOGRAPHIC DATA SHEET

(See instructions on the reverse)

1. REPORT NUMBER (Assigned by NRC. Add Vol., Supp., Rev., and Addendum Numbers, if any.)
NUREG/CR-6096

2. TITLE AND SUBTITLE
Apache Leap Tuff INTRAVAL Experiments

Results and Lessons Learned

3. DATE REPORT PUBLISHED
MONTH: March
YEAR: 1996

4. FIN OR GRANT NUMBER
L1282

5. AUTHOR(S)
T. C. Rasmussen*, S. C. Rhodes, A. Guzman, S. P. Neuman

6. TYPE OF REPORT
Technical

7. PERIOD COVERED *(Inclusive Dates)*
11/89 - 05/95

8. PERFORMING ORGANIZATION – NAME AND ADDRESS *(If NRC, provide Division, Office or Region, U.S. Nuclear Regulatory Commission, and mailing address; if contractor, provide name and mailing address.)*
Department of Hydrology and Water Resources
University of Arizona
Tucson, AZ 85721

*University of Georgia
Athens, GA 30602

9. SPONSORING ORGANIZATION – NAME AND ADDRESS *(If NRC, type "Same as above"; if contractor, provide NRC Division, Office or Region, U.S. Nuclear Regulatory Commission, and mailing address.)*
Division of Regulatory Applications
Office of Nuclear Regulatory Research
U.S. Nuclear Regulatory Commission
Washington, DC 20555-0001

10. SUPPLEMENTARY NOTES
T. Nicholson, NRC Project Manager

11. ABSTRACT *(200 words or less)*
Data from laboratory and field experiments in unsaturated fractured rock are summarized and interpreted for the purpose of evaluating conceptual and numerical models of fluid, heat and solute transport. The experiments were conducted at four scales, in small cores (2.5-cm long by 6-cm across), a large core (12-cm long by 10-cm across), a small block containing a single fracture (20 x 21 x 93 cm), and at field scales in boreholes (30-m long by 10-cm across) at three scales (½-, 1- and 3-meters). The smallest scale in the laboratory provided isothermal hydraulic and thermal properties of unfractured rock. Nonisothermal heat, fluid and solute transport experiments were conducted using the large core. Isothermal gas and liquid flow experiments were conducted in the fractured block. Field-scale experiments using air were used to obtain *in situ* permeability estimates as a function of the measurement scale. Interpretation of experimental results provides guidance for resolving uncertainties related to radionuclide migration from high level waste repositories in unsaturated fractured rock.

12. KEY WORDS/DESCRIPTORS *(List words or phrases that will assist researchers in locating the report.)*
air permeability testing
fracture flow
imbibition experiments
model validation
non-isothermal
relative permeability
moisture retention curves
site characterization data
unsaturated flow & transport
model testing

13. AVAILABILITY STATEMENT
Unlimited

14. SECURITY CLASSIFICATION
(This Page)
Unclassified
(This Report)
Unclassified

15. NUMBER OF PAGES

16. PRICE

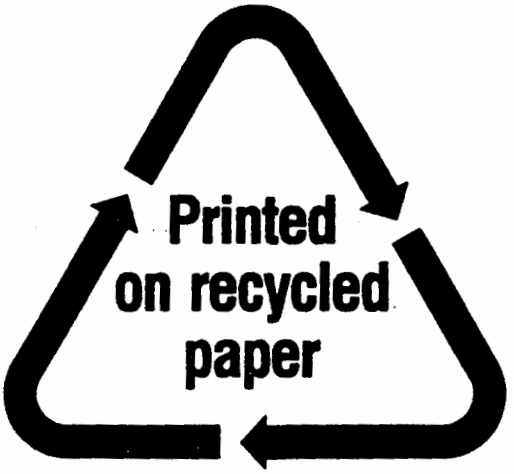

Federal Recycling Program